Ph. D. thesis

A Study on Application of Nacelle LiDAR to Wind Turbine Power Performance Verification

Dongheon Shin

Multidisciplinary Graduate School Program for Wind Energy

Graduate School

Jeju National University

August 2019

A Study on Application of Nacelle LiDAR to Wind Turbine Power Performance Verification

指導敎授 高 炅 男

申 東 憲

이 論文을 工學 博士學位 論文으로 提出함

2019 年 6 月

申東憲의 工學 博士學位 論文을 認准함

審査委員長 _김범석_ ㊞

委　　　員 _최종철_ ㊞

委　　　員 _정지현_ ㊞

委　　　員 _강용혁_ ㊞

委　　　員 _근경남_ ㊞

濟州大學校 大學院

2019 年 6 月

A Study on Application of Nacelle LiDAR to Wind Turbine Power Performance Verification

Dongheon Shin

(Supervised by professor Kyungnam Ko)

A dissertation submitted in partial fulfillment of the requirement for the degree of Doctor of Philosophy

2019. 6.

This dissertation has been examined and approved.

Thesis director, Bumsuk Kim, Prof. of Faculty of Wind Energy Engineering

Jongchul Huh, Prof. of Mechanical Engineering

Jihyun Jeong, Prof. of Mechanical Engineering

Yongduck Kang, Prof. of Naval Architecture and Ocean Engineering, Dong-Eui University

Kyungnam Ko, Prof. of Faculty of Wind Energy Engineering

June 2019

Multidisciplinary Graduate School Program for Wind Energy
Graduate School
Jeju National University

Contents

List of Figures

List of Tables

Nomenclature

Symbol	Description	Unit
A	Swept area by the rotor	$[m^2]$
A_i	Area of the i-th segment	$[m^2]$
AEP	Annual energy production	
AEP_{Cup}	AEP calculated from PC_{Cup}	
$AEP_{NTF,Cup}$	AEP calculated from $PC_{NTF,Cup}$	
$AEP_{NTF,NL}$	AEP calculated from $PC_{NTF,NL}$	
B_{10min}	Air pressure averaged over 10-minute	[hPa]
$c_{B,i}$	Sensitivity factor of pressure	[W/Pa]
C_P	Power coefficient	
$C_{P,NL}$	Power coefficient obtained with nacelle LiDAR measurements	
$C_{P,REWS}$	Power coefficient obtained with REWS	
$C_{P,Cup}$	Power coefficient obtained with cup anemometer wind speed	
$C_{P,NTF,Cup}$	Power coefficient using NTF_{Cup}	
$C_{P,NTF,NL}$	Power coefficient using NTF_{NL}	
$c_{T,i}$	Sensitivity factor of air temperature	[W/K]
$c_{V,AEP,i}$	Sensitivity factor for uncertainty in wind speed for AEP	
$c_{V,PC,i}$	Sensitivity factor for uncertainty in wind speed for power curve	
CAN	Controller area network	
CF	Capacity factor	
CNR	Carrier-to-noise ratio	[dB]
CT	Current transformer	
D	Rotor diameter	[m]

D_e	Equivalent rotor diameter	[m]
D_n	Rotor diameter of nearby wind turbine	[m]
DAQ	Data aquisition system	
DTU	Technical University of Denmark	
FCR	Flow complexity recognition	
$F(V_i)$	Rayleigh cumulative probability distribution function	
f_i	Relative occurrence of wind speed	
$f_{r,RSD}$	Wind shear correction factor	
FFT	Fast Fourier transforms	
$g(z)$	Integrated function	
H	Hub height	[m]
IEC	International Electrotechnical Commission	
KTL	Korea Testing Laboratory	
L	Distance between a test wind turbine and a met mast	[m]
L_e	Distance from neighboring wind turbine to test wind turbine	[m]
l_h	Height of obstacle	[m]
L_n	Distance from obstacle to test wind turbine	[m]
$L_{pretilt}$	Distance between OH of nacelle LiDAR and rotor plan	[m]
l_w	Width of obstacle	[m]
LiDAR	Light detection and ranging	
LOS	Line of sight	
Met mast	Meteorological mast	
N_h	Number of hours in a year	
n_h	Number of measurement heights	
N_i	Number of 10-minute data sets in bin i	
NTF	Nacelle transfer function	

NTF$_{Cup}$	NTF derived from cup anemometer wind speed	
NTF$_{NL}$	NTF derived from nacelle LiDAR measurements	
OH	Optical head	
P$_c$	Received modulated carrier signal power	[W]
P$_i$	Normalized and averaged power output in bin i	[W]
P$_m$	Measured power output	[W]
P$_n$	Received noise power	[W]
P$_r$	Rated power output	[W]
P$_W$	Gas constant of vapor pressure	[Pa]
PC$_{Cup}$	Power curve obtained with cup anemometer wind speed	
PC$_{IEC}$	Power curves drawn according to IEC standards	
PC$_{NL}$	Power curve obtained with nacelle LiDAR measurements	
PC$_{NTF,Cup}$	Power curve using NTF$_{Cup}$	
PC$_{NTF,NL}$	Power curve using NTF$_{NL}$	
PC$_{REWS}$	Power curve obtained with REWS	
PT	Power transducer	
PU	Processing unit	
R	Radius of the rotor swept area	[m]
R^2	Coefficient of determination	
R$_0$	Gas constant of dry air 287.05 J/kgK	
R$_W$	Gas constant of water vapor	
REWS	Rotor equivalent wind speed	
RIX	Ruggedness index	
RPM	Revolutions per minute	
RWS	Radial wind speed	
S$_{p,i}$	Category A uncertainty in electrical power	[W]

SCADA	Supervisory control and data acquisition	
T_{10min}	Absolute air temperature averaged over 10-minute	[K]
$u_{AD,i}$	Category B uncertainty in air density	
u_{AEP}	Uncertainty of AEP	[W]
$u_{AEP,Cup}$	Uncertainty of AEP_{Cup}	[W]
$u_{AEP,NTF,Cup}$	Uncertainty of $AEP_{NTF,Cup}$	[W]
$u_{AEP,NTF,NL}$	Uncertainty of $AEP_{NTF,NL}$	[W]
$u_{B,i}$	Uncertainty in pressure	[Pa]
$u_{FS,Cup}$	Uncertainty in free stream wind speed from a met mast	[m/s]
$u_{FS,NL}$	Uncertainty in free stream wind speed from nacelle LiDAR	[m/s]
$u_{FS,NL1}$	Statistical uncertainty of the nacelle LiDAR measurements	[m/s]
$u_{FS,NL2}$	Uncertainty caused by flow distortion due to terrain	[m/s]
$u_{FS,NL3}$	Uncertainty related to the measurement height	[m/s]
$u_{FS,NL4}$	Uncertainty of the tilt inclinometers	[m/s]
$u_{M,i}$	Category B uncertainty in the method	[m/s]
$u_{p,i}$	Category B uncertainty in power output	[W]
u_{PC}	Uncertainty in power curve	
$u_{PC,Cup}$	Uncertainty in PC_{Cup}	
$u_{PC,NTF,Cup}$	Uncertainty in $PC_{NTF,Cup}$	
$u_{PC,NTF,NL}$	Uncertainty in $PC_{NTF,NL}$	
$u_{T,i}$	Category B uncertainty in air temperature	[K]
$u_{V,i}$	Category B uncertainty in wind speed	[m/s]
V_{10min}	Measured wind speed averaged over 10-minute	[m/s]
V_{Cup}	Wind speed measured from cup anemometer	[m/s]
$v_{eq,final}$	Final REWS	[m/s]
V_{free}	Free-stream wind speed	[m/s]

$v_{h,MM}$	Cup anemometer wind speed at hub height	[m/s]
V_{hub}	Wind speed extrapolated to the hub height	[m/s]
V_i	Normalized and averaged wind speed in bin i	[m/s]
V_n	Normalized wind speed for air density	[m/s]
$V_{nacelle}$	Wind speed measured from nacelle anemometer	[m/s]
V_{NL}	Wind speed measured from nacelle LiDAR	[m/s]
V_r	Rated wind speed of wind turbine	[m/s]
V_{REWS}	REWS	[m/s]
z_i	Height of the i-th segment separation line	[m]
$z_{NL,i}$	Average nacelle LiDAR measurement height in bin i	[m]
$Z_{pretilt}$	Distance between OH of nacelle LiDAR and rotor axis	[m]
α	Opening angle	[deg]
$\beta_{pretilt}$	Tilt value measured by nacelle LiDAR	[deg]
ΔH	Maximum error of beam detection pointing	[m]
Δz_1	Vertical length	[m]
$\Delta\beta_T^2$	Standard uncertainty of tilt measurement of theodolite	[deg]
ρ_0	Reference air density of 1.225 kg/m^3	[kg/m^3]
ρ_{10min}	10-minute averaged air density at a site	[kg/m^3]
ϕ	Relative humidity [range 0 to 1]	

Abstract

After constructing and commissioning a wind farm, the power performance of wind turbines should be tested; and further, the measured power curve should be verified by comparing it with the guaranteed power curve provided by a manufacturer in accordance with International Electrotechnical Commission (IEC) 61400-12 standards. Hence, the meteorological mast (met mast) must be installed at a minimum of 100 m above the ground level because that large wind turbines with a hub height beyond 100 m have been developed. However, the installation is costly and time consuming.

To solve this problem, a lot of studies for application of light detection and ranging (LiDAR) systems to wind turbine power performance testing have been carried out in the pioneering countries. The ground LiDAR has been already applied to derive the rotor equivalent wind speed (REWS) suggested in IEC 61400-12-1 2nd edition. Meanwhile, for the application of nacelle LiDAR to wind turbine power performance testing, a project team IEC 61400-50-3 was organized, and they have been working towards publishing the official international standard IEC 61400-50-3 by the end of 2020.

To clarify the difference in the wind turbine power curves obtained by a cup anemometer, REWS, and nacelle LiDAR measurements, the wind turbine power performance measurement was experimentally performed at the Haengwon wind farm on Jeju Island, South Korea. A 2-beam nacelle LiDAR mounted on the nacelle of a 1.5 MW test wind turbine was used with a met mast and a ground LiDAR positioned at a distance 2.5 times the rotor diameter from the turbine.

To establish the standard for nacelle LiDAR data filtering, the characteristics of nacelle LiDAR measurements were firstly analyzed by dividing them into three parts: weather conditions (temperature, humidity, pressure, amount of precipitation), mechanical movement (rotation of wind turbine blades, tilt variation of nacelle LiDAR), and nacelle LiDAR data availability. After data filtering, the reliability of the nacelle LiDAR measurements was assessed by comparing it with the cup anemometer wind speed on a met mast. Therefore, various weather conditions and mechanical movements did not disturb reliable data measurement. Nacelle LiDAR measurements with an availability of 80 % or more could be used for checking nacelle LiDAR wind data reliability. The reliability of nacelle LiDAR was extremely high with a regression coefficient of 98 % and coefficient of determination of 97 %.

The REWS was derived from cup anemometer and ground LiDAR measurements in accordance with the IEC 61400-12-1 2nd edition. The scatter plots were drawn using the wind data measured by each instrument and compared in terms of the standard deviation. The power curve by nacelle LiDAR measurements (PC_{NL}) was then compared with those by the cup anemometer measurements (PC_{Cup}) and REWS (PC_{REWS}) according to IEC 61400-12-1 1st and 2nd editions. To quantitatively identify the difference in the power curves, the relative error of PC_{NL} was calculated by assuming that the power curves with the IEC standards are references. Consequently, the relative error for the power output in the bin interval of 0.5 m/s before the rated wind speed was high, whereas that after the rated was close to 0 %. The relative errors with PC_{Cup} and PC_{REWS} were 3.01 % and 3.51 % on average, respectively.

Additionally, a study on the application of the nacelle transfer function by nacelle LiDAR (NTF_{NL}) was conducted for the power performance measurement of multiple wind turbines at the Dongbok wind farm on Jeju Island, South Korea. A 4-beam nacelle LiDAR was mounted on the nacelle of a 2 MW wind turbine to measure wind conditions in front of the turbine rotor, and an 80 m high met mast was installed near another wind turbine to measure the free-stream wind speed.

The NTF was determined by a table method, and then the power curve drawn using the NTF_{NL} ($PC_{NTF,NL}$) was compared with those drawn in compliance with IEC 61400-12-1 and 61400-12-2 (PC_{Cup} and $PC_{NTF,Cup}$). The combined standard uncertainties of the power curves were calculated to clarify the magnitude of the components of the uncertainties. The uncertainties of annual energy production (AEP) were also estimated by assuming that wind speed is a Rayleigh wind speed distribution. The results revealed that $PC_{NTF,NL}$ was in good agreement with the power curves drawn in accordance with the IEC standards. The difference between combined standard uncertainties of $PC_{NTF,NL}$ and $PC_{NTF,Cup}$ was within the range 3.5 % to 8.3 %.

초 록

기존의 국제표준 IEC(International Electrotechnical Commission) 61400-12 시리즈에 따라 풍력터빈 출력성능평가를 수행하기 위해서는 반드시 기상탑(Meteorological mast)이 설치되어야 한다. 오늘 날, 현대의 풍력터빈이 대형화되고 풍력산업이 해상풍력에 초점이 맞춰짐에 따라 허브높이 100 m 이상의 기상탑 설치가 요구되고, 이에 따라 기상탑 설치 시에 경제적, 시간적, 공간적 문제 등의 어려움이 발생한다. 이에 대한 해결책으로 풍력터빈 출력성능평가에 라이다(Light detection and ranging, LiDAR) 시스템 도입을 위한 연구가 세계 풍력 선도국을 중심으로 활발하게 진행되고 있다. 지상기반 라이다(Ground LiDAR)는 IEC 61400-12-1 제2판의 로터등가풍속(Rotor equivalent wind speed, REWS) 도출을 위하여 이미 적용되고 있다. 한편, 풍력터빈 출력성능평가에 나셀 라이다(Nacelle LiDAR)를 적용하기 위하여 IEC PT 61400-50-3이 조직되어 세계의 나셀 라이다 전문가들이 2020년 말 국제표준 발행을 목표로 활발한 연구를 수행하고 있다. 하지만, 나셀 라이다 데이터의 신뢰성 검증 및 풍력터빈 출력성능평가에 적용, 검증한 연구사례는 많지 않으며, 다양한 조건에서의 더 많은 현장 시험 및 검증이 요구되고 있다. 이 논문은 풍력터빈 출력성능평가에 나셀 라이다 시스템의 적용 가능성을 확인하기 위한 나셀 라이다 기반의 풍력터빈 출력성능평가 현장시험 평가결과를 나타낸다.

제주도 행원 풍력발전단지의 1.5 MW 풍력터빈을 대상으로 2빔 나셀 라이다 측정 데이터를 이용한 풍력터빈 출력곡선이 그려졌고, 풍력터빈으로부터 로터직경 2.5배 거리에 위치한 기상탑의 컵 풍속계와 지상기반 라이다의 측정 데이터로부터 IEC 61400-12-1 제1판 및 제2판에 따라 그려진 출력곡선들과 비교하였다. 풍력터빈 출력곡선 작성에 앞서 나셀 라이다 데이터의 데이터 오차처리 기준을 수립하기 위하여 다양한 조건에서의 나셀 라이다 측정 데이터 특성이 분석되었

다. 나셀 라이다 측정 데이터 특성은 기상상태(온도, 습도, 기압, 강수량), 기계거동(로터 블레이드 회전, 나셀 라이다 틸트 변화), 데이터 가용률에 따른 반송파 대 잡음비(Carrier-to-noise ratio, CNR) 신호 및 측정 정확도로 분류하여 분석되었다. 측정 데이터 특성 분석 결과를 토대로 나셀 라이다 데이터를 오차처리 하였고, 컵 풍속계 풍속과의 선형회귀분석을 통하여 데이터 신뢰성을 검증하였다. 그 결과, 나셀 라이다 데이터 측정 시에 다양한 기상조건 변화에도 CNR 값은 정상 범위임을 확인하였고, 로터 블레이드 회전은 나셀 라이다 데이터의 정상적인 측정에 방해요소로 작용하지 않음을 확인하였다. 또한, 데이터 가용률 80 % 이상의 측정 데이터가 유효함을 알 수 있었다. 컵 풍속계 풍속 데이터와의 선형회귀분석 결과는 회귀계수와 결정계수가 거의 1에 근접함에 따라 나셀 라이다 측정 데이터의 신뢰성은 매우 높음을 알 수 있었다. 나셀 라이다 및 컵 풍속계 풍속, 지상기반 라이다를 이용한 로터등가풍속에 대한 출력 산포도가 비교되었고, 빈 방법을 이용하여 출력곡선들이 그려졌다. 출력곡선들 간의 차이를 정량적으로 식별하기 위하여 IEC 표준에 따른 출력곡선들을 참값으로 가정하여 0.5 m/s 빈 간격의 나셀 라이다 출력곡선의 상대오차를 계산하였다. 그 결과, 정격풍속 이전 구간의 상대오차는 다소 높았지만, 정격풍속 이후 구간의 상대오차는 거의 0 %에 가까웠다. 전 구간의 평균 상대오차는 컵 풍속 출력곡선의 경우 3.01 %, 로터등가풍속 출력곡선의 경우 3.51 % 이였다.

추가적으로 다수 풍력터빈의 출력성능평가를 위하여 나셀 라이다 기반 나셀변환함수(Nacelle transfer function, NTF)의 적용 가능성이 연구되었다. 이 연구는 제주도 동복 풍력발전단지의 2 MW 풍력터빈 2기(동복 풍력터빈 1호기, 15호기)를 대상으로 수행되었다. 동복 풍력터빈 1호기 나셀 위에 설치된 4빔 나셀 라이다와 나셀 풍속계로부터 측정된 풍속 데이터를 이용하여 나셀 라이다 기반 NTF가 도출되었으며, 도출된 나셀 라이다 기반 NTF를 동복 풍력터빈 1호기와 15호기에 각각 적용하여 출력곡선들을 작성하였다. 작성된 나셀 라이다 기반 NTF 출력곡선들은 동복 풍력터빈 15호기로부터 로터직경 2.5배 거리에 위치한 기상탑

의 컵 풍속계 데이터로부터 IEC 61400-12-1 및 IEC 61400-12-2에 따라 그려진 컵 풍속계 출력곡선 및 컵 풍속 기반 NTF 출력곡선과 선형회귀분석을 통하여 비교되었다. 또한, 각 출력곡선에 대한 합성표준불확도가 추정되었고, 합성표준불확도를 이루는 각 요소 별 불확도가 평가되었다. 이 때, 나셀 라이다 풍속에 대한 불확도를 추정하기 위한 불확도 요소와 불확도 추정 방법이 제안되었다. 그 결과, 나셀 라이다 기반 NTF 출력곡선은 IEC 국제표준에 따라 그려진 출력곡선들과의 회귀계수 및 결정계수가 거의 1에 가까우며 높은 상관성을 보였다. 나셀 라이다 기반 NTF 출력곡선과 IEC 61400-12-2에 근거하여 그려진 컵 풍속계 기반 NTF 출력곡선의 합성표준불확도 차이는 3.5 ~ 8.3 % 범위 내였다.

I. Introduction

1. Background

Wind energy is one of the most well-known forms of renewable energy. At the end of 2017, the worldwide total cumulative installed electricity generation capacity from wind power amounted to 513 GW, an increase of 10 % compared with the previous year [1]. Among the total wind energy capacity, offshore wind energy capacity exceeded 3 GW in 2010 and had increased to approximately 16 GW in 2017 [2]. By 2020, offshore wind energy is projected to grow to a total installed capacity of 25 GW [3].

To increase the efficiency of wind energy, several studies have been conducted in areas such as wind resource assessment, wind farm design, and wake effect analysis [4-25]. For these studies, it is crucial to measure the accurate wind data and essential to install a meteorological mast (met mast) of hub height.

To test the power performance of wind turbines, wind conditions should be measured for more than six months at the hub height of a test wind turbine. Wind turbine power performance testing is required to obtain a certification of wind turbine prototype, including load measurement and blade testing, and it shows how much energy is generated as a function of the kinetic energy available in the surrounding wind. Moreover, wind turbine power performance testing should be conducted following constructing and commissioning of a wind farm because the financial viability of a project is determined by the wind turbine power curve. Consequently, the power performance of wind turbines should be verified by comparing the measured power curve with the power curve guaranteed by a manufacturer.

The power performance of wind turbines should be tested in accordance with International Electrotechnical Commission (IEC) 61400-12 standards.

"IEC 61400-12-1 1st edition (2005)" is a first international standard to test the power performance of wind turbines. The standard requires installation of a met mast of hub height within a distance that is 2 to 4 times the rotor diameter from a test wind turbine [26]. Even today, numerous studies on power performance testing have been performed using the met mast wind data according to this standard.

"IEC 61400-12-2 (2013)" describes the methodology that can be used to evaluate the power performance of multiple wind turbines using the nacelle transfer function (NTF), which is the correlation between wind speeds measured using an anemometer on a met mast and a nacelle anemometer on a wind turbine [27].

"IEC 61400-12-1 2nd edition (2017)" describes the procedure and requirements for wind turbine power performance test using the rotor equivalent wind speed (REWS), which considers the wind shear covering the wind turbine rotor swept area, to evaluate the annual energy production (AEP) more accurately [28].

The IEC standards to test the power performance of wind turbines require installation of the met mast. However, met mast installation is costly and time consuming. Recently, installing a met mast has become difficult because large wind turbines with a hub height beyond 100 m have been manufactured, thus implying that met masts must be installed beyond 100 m above the ground level. In addition, it is known to be extremely difficult to install an offshore met mast in the ocean for measuring offshore wind conditions.

Furthermore, the power performance of wind turbines has been generally tested for a representative wind turbine owing to the difficulty of installing met masts for all turbines, despite the fact that power performance testing has to be conducted for all wind turbines on a wind farm.

As a solution to this problem, light detection and ranging (LiDAR) systems have received attention from the wind energy industry because they can be easily installed and relocated with a wide measurement range, thus implying that it is possible to measure the wind condition for multiple wind turbines at comparatively lower cost and in a shorter time period, particularly for offshore wind farms that require a difficult approach.

Based on the large amount of studies on reliability verification of ground LiDAR wind data and analysis results for large scale wind turbine power performance measurement [29-54], the ground LiDAR has been already applied to derive REWS in IEC 61400-12-1 2nd edition.

According to the demand of nacelle LiDARs for wind turbine power performance measurement, a project team responsible for IEC 61400-50-3 has been organized and is making an effort to publish the official international standard "IEC 61400-50-3" by the end of 2020 [55]. However, the related research is still insufficient. It is necessary to verify the reliability of nacelle LiDAR measurements under various conditions, and to identify the applicability of nacelle LiDAR to measure the power performance of wind turbines by comparing the power curve by nacelle LiDAR measurements with those of IEC standards through further experimental studies.

Additionally, an alternative plan for power performance measurement of multiple wind turbines is needed because power performance testing for a wind turbine takes more than six months, although the use of a nacelle LiDAR to test the power performance of wind turbines can replace wind condition measurement by the met mast from an economic aspect.

2. Research trend

Many studies have been conducted on wind turbine power performance in accordance with IEC 61400-12-1 1st edition [56-65]. For instance, Curvers et al. [58] derived the sector-wise power curves of an entire wind farm comprising 36 wind turbines from supervisory control and data acquisition (SCADA) data. The wind farm efficiency was 91.5 %. Barber et al. [60] evaluated the power performance of the Enercon E-40 600 kW wind turbine at an Alpine test site in Switzerland. They found that the air temperature considerably influenced the AEP of the turbine, and determined that a power curve correction technique was thus needed for accurate prediction of the performance. Altan et al. [64] pointed out that the performance of the Savonius wind rotor can be enhanced by arranging a curtain in front of the rotor.

The procedure for power performance testing in the IEC 61400-12-1 applies specifically to wind turbines with a tall met mast. For that reason, investigations have been conducted on the possibility of using nacelle wind speed to test the power performance of wind turbines in order to avoid having to install a tall met mast, which would be very expensive and time-consuming. Suzuki et al. [66] showed the corrected power curve of a J70 2 MW wind turbine, based on wind data from a ground LiDAR, a met mast, and a nacelle anemometer. Hernandez et al. [67] proposed a method to validate wind farm power performance by analyzing SCADA data from wind turbines based on the Friedman's test (which is a non-parametric statistical inference technique) and by verifying that the proposed method was acceptable for evaluating the power performance of a specific wind farm. Power performance testing was conducted by Oh et al. [68] using the nacelle wind speed data for multiple wind turbines operating on complex terrain. They found that the power outputs of each wind turbine varied considerably,

which led to the conclusion that power performance verification should be done for each wind turbine when the wind farm is located on complex terrain. Power performance was evaluated for multiple wind turbines by investigating the relationship between nacelle anemometer and met mast wind speeds to estimate the NTF. Ormel et al. [69] presented an advanced nacelle anemometry technique for performance monitoring: first, they calculated the NTF; then they used computational fluid dynamics (CFD) to analyze the wind flow at the rotor. They then discussed the correlation between the NTF and free-stream wind. Finally, the international standard IEC 61400-12-2 was published, making it possible to conduct power performance tests for multiple wind turbines by using the NTF to transfer the nacelle anemometer to met mast free-stream wind data. According to this standard, IEC 61400-12-2, Kim et al. [70] conducted power performance measurement for two 3 MW wind turbines in compliance with the standard. Shin et al. [71-73] proposed a methodology for identifying wind turbine degradation using the NTF and evaluated the annual capacity factor (CF) reduction of two commercial wind farms.

For the last few years, many verification campaigns have been conducted to approve the LiDAR system as the standard measuring device to test the power performance of wind turbines in the IEC standards. For example, Smith et al. [30] conducted a comparative study using wind data measured by a continuous wave (CW) ZephIR LiDAR and a cup anemometer up to a height of 100 m. It showed that a linear regression lines varied from 0.96 to 0.99 for flat and homogeneous terrain. A comparison of wind data for three months measured from the QinetiQ ZephIR LiDAR and a 100 m-height tall met mast was conducted in the North Sea off the German coast in 2007 [32]. In this campaign, the correlation coefficient was close to one, although the slopes between LiDAR and met mast wind speeds decreased with height. Shu et al. [49] reported that the correlation coefficient between CW LiDAR and

met mast wind speeds were more than 0.99 with a regression slope of 1.00 – 1.03. Kim et al. [39, 40] compared the Windcube v2 ground LiDAR measurements with Remtech sound detection and ranging (SoDAR) wind data, and they analyzed the uncertainty in vertical wind distribution. Kim et al. [52] reported the reliability of ground LiDAR measurements according to terrain complexity by comparing ground LiDAR measurements measured at three points. Overall, ground LiDAR measurements have been similar to reference wind data. According to the investigation results on reliability verification of ground LiDAR measurements, the ground LiDAR has been applied to measure wind data at more than hub height for deriving REWS in IEC 61400-12-1 2nd edition.

Meanwhile, several investigations on the use of a nacelle LiDAR for wind turbine power performance measurement have been conducted. For instance, Courtney [74] proposed the procedure for line of sight (LOS) calibration with tilt and roll calibration of a 2-beam nacelle LiDAR. Borraccino et al. [75] reported a generic methodology for radial wind speed (RWS) calibration of 2-beam nacelle LiDAR. They discussed the calibration procedure concepts with uncertainty analysis, and demonstrated the reliability of the nacelle LiDAR measurements. Davoust et al. [76] researched the measurement availability of nacelle LiDAR for LiDAR system characteristics, mounting configurations, atmospheric conditions and wind reconstruction algorithms. Variable parameters affecting measurement availability were modelled and predicted, and the nacelle LiDAR availability for wind turbine control was defined and demonstrated. The measurement campaign using a nacelle LiDAR was conducted, and a procedure to test the power performance of wind turbines using a nacelle LiDAR was proposed by Wagner et al. [77-80]. They also proposed the components and mathematical equations for estimating power curve uncertainty [81].

Apart from wind turbine power performance measurement, the nacelle LiDAR has been investigated and applied to various other measurements. Fleming et al. [82] reported the efficiency improvement of wind turbines by correcting yaw misalignment using a nacelle LiDAR, resulting in an AEP increase of 2.4 %. Schlipf et al. [83] conducted a field test of LiDAR assisted collective pitch control using a scanning LiDAR mounted on a wind turbine nacelle of 600 kW wind turbines, and they reported that structural loads on the tower base assembly of the wind turbine decreased by 10 % compared to normal loads.

3. Objectives

In this thesis, a field test was experimentally conducted in order to identify the applicability of nacelle LiDAR to wind turbine power performance measurement, and the nacelle transfer function based on nacelle LiDAR measurement is suggested for power performance measurement of multiple wind turbines.

The objectives of this study are as follows :

1) To establish the standard for nacelle LiDAR data filtering through characteristics analysis of nacelle LiDAR measurements under various conditions, and to verify the reliability of nacelle LiDAR measurements by comparing them with reference wind data (Chapters III and IV)

2) To identify the applicability of a nacelle LiDAR to wind turbine power performance measurement without a tall met mast, by quantifying the difference between the power curve by a nacelle LiDAR and those according to IEC 61400-12-1 1st and 2nd editions (Chapter III)

3) To suggest the NTF by nacelle LiDAR (NTF_{NL}) for power performance measurement of multiple wind turbines and to verify the proposed method by comparing the power curve by NTF_{NL} with those according to IEC 61400-12-1 and IEC 61400-12-2 (Chapter IV)

The contents of each chapter are briefly described hereafter.

Chapter II: "Doppler wind LiDAR" provides the reader with the measurement principle and the type of Doppler wind LiDAR.

Chapter III: "Applicability of a nacelle LiDAR to wind turbine power performance measurement" focuses on the use of a nacelle LiDAR for power curve verification. The power curve obtained with the nacelle LiDAR measurements (PC_{NL}) is compared with those derived in compliance with IEC 61400-12-1 1st and 2nd editions, and the relative errors between the power curves is computed to quantitatively identify the difference between them.

Chapter IV: "Application of the NTF from the nacelle LiDAR measurements for power performance measurement of multiple wind turbines" concentrates on the applicability of NTF_{NL} for power performance measurement of multiple wind turbines. The procedure and requirements for NTF_{NL} derivation and application are introduced. The power curves drawn using NTF_{NL} ($PC_{NTF,NL}$) are compared with those drawn in compliance with IEC 61400-12-1 and IEC 61400-12-2. In addition, the uncertainties of the power curves and AEPs are estimated.

Chapter V: "Summary and conclusions" summarizes and discusses the main results of the work. Research ideas and recommendations for future work are also described.

II. Doppler wind LiDAR

1. Measurement principle of Doppler wind LiDAR [84]

The measurement principle of a Doppler wind LiDAR has four steps. First, the Doppler wind LiDAR senses backscattered light from aerosols or particles moving with the wind, as shown in Fig. II-1. The return light proceeds from scatterers included in a probe volume positioned along the laser beam propagation path. The contribution of each scatterer is weighted as a function of its distance to the point of focus for continuous wave or center of the range-gate pulsed Doppler wind LiDAR systems. Second, the Doppler wind LiDAR converts the time signal into a Doppler power spectrum using fast Fourier transforms, and the derived spectrum corresponds to a distribution or histogram of Doppler frequency shifts. Then, the Doppler wind LiDAR deduces LOS velocities from the Doppler spectra. Finally, wind field characteristics such as speed, direction, and shear are evaluated by combining multiple LOS velocity measurements.
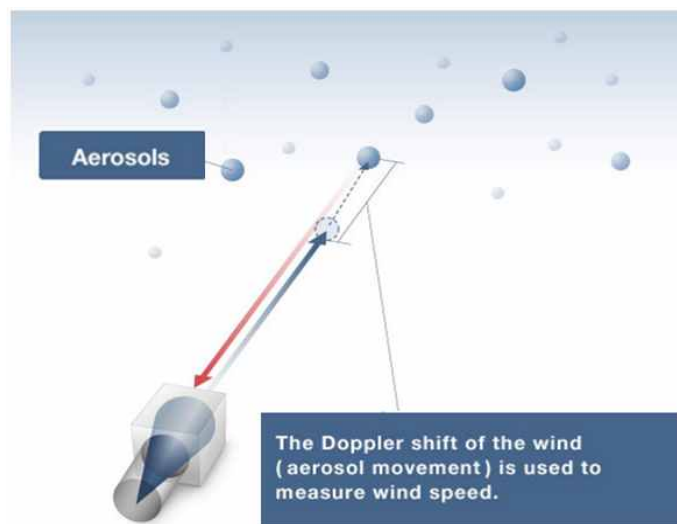
Fig. II-1 Schematic of Doppler wind LiDAR measurement principles

2. Type of Doppler wind LiDAR systems

The Doppler wind LiDAR can be classified into four types.

The nacelle LiDAR mounted on the nacelle of wind turbine measures wind conditions by emitting laser beams horizontally towards the wind turbine rotor. It is developed for wind turbine power performance testing.

Fig. II-2 Example of a nacelle LiDAR [85, 86]

A ground LiDAR measures wind conditions by emitting laser beams vertically from ground. It has been generally used for wind resource assessment and was recently applied to derive REWS in IEC 61400-12-1 2nd edition.

Fig. II-3 Example of a ground LiDAR [87, 88]

제주대학교 중앙도서관
JEJU NATIONAL UNIVERSITY LIBRARY

The ground LiDAR is also installed on a buoy or platform on the sea, and it is used for offshore wind resource assessment as floating or platform LiDARs.

Fig. II-4 Example of floating and platform LiDARs [89, 90]

A scanning LiDAR provides 360° scan of the atmosphere to provide enhanced measurements of wind resources; it makes numerous applications possible including wind mapping, site assessment, and wake measurements.
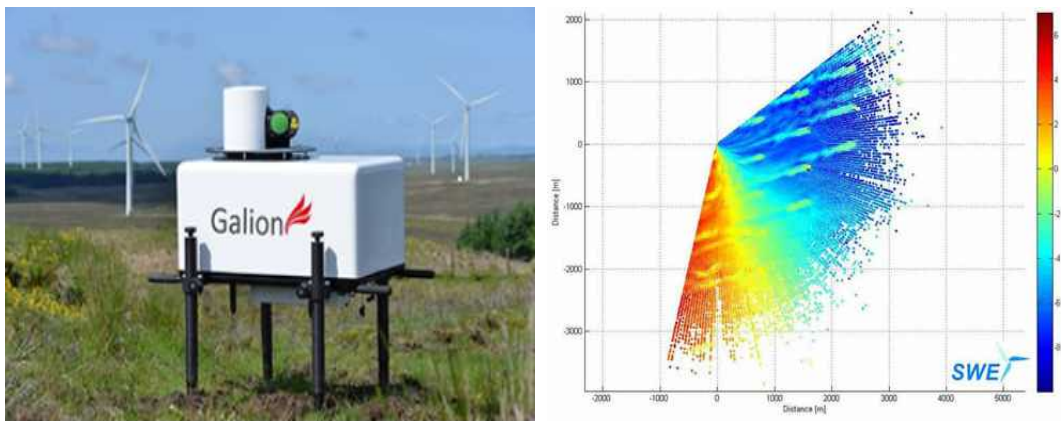
Fig. II-5 Example of a scanning LiDAR [91]

III. Applicability of a nacelle LiDAR to wind turbine power performance measurement [1]

This Chapter aims to identify the difference in wind turbine power curves obtained by nacelle LiDAR measurements (PC_{NL}), cup anemometer wind data (PC_{Cup}), and REWS (PC_{REWS}) in order to clarify the applicability of LiDAR systems to test the power performance of wind turbines without a tall met mast.

The investigation was experimentally conducted at the Haengwon wind farm on Jeju Island, South Korea. A nacelle LiDAR on a 1.5 MW test wind turbine was used with a met mast and a ground LiDAR positioned at a distance of 2.5 times the rotor diameter from the test wind turbine.

To establish the standard for LiDAR data filtering, the characteristics of nacelle LiDAR wind data were firstly analyzed in terms of three categories: weather conditions, mechanical movement, and data availability. After data filtering, a linear regression analysis between wind speeds was conducted.

The REWS was derived from a cup anemometer and ground LiDAR measurements in accordance with the IEC 61400-12-1 2nd edition. The derived REWS was compared with the cup anemometer wind speed.

From the selected wind data, the scatter plots of power output were drawn and compared in terms of the standard deviation. Finally, PC_{NL} was compared with PC_{Cup} and PC_{REWS} drawn according to IEC 61400-12-1 1st and 2nd editions. To quantitatively clarify the difference between power curves, the relative errors were estimated for the power outputs under the reference wind speeds from the cup anemometer and REWS.

---

1) This chapter was written by citing from the author's papers published in Journal of Mechanical Science and Technology (2018) and Journal of the Korean Energy Society (2017) [92, 93].

1. Test setup

1) Test site I

(1) Haengwon wind farm

The power performance measurement using a nacelle LiDAR was conducted at the Haengwon wind farm on Jeju Island, South Korea. The island is located off the southern part of the Korean peninsula, and the Haengwon wind farm is located on the northeastern part of Jeju Island, as shown in Fig. III-1. The Haengwon wind farm is situated on the coastal region, and the topographical conditions are relatively flat, with a roughness class of 0.1, and a ruggedness index (RIX) of 0.0. A nacelle LiDAR was mounted on the nacelle of a 1.5 MW test wind turbine, and a met mast and a ground LiDAR were installed at a distance 2.5 times the rotor diameter of the wind turbine.

The 10-minute averaged wind data measured by the instruments were collected for approximately 8.5 months, from 17 May 2016 to 2 March 2017.
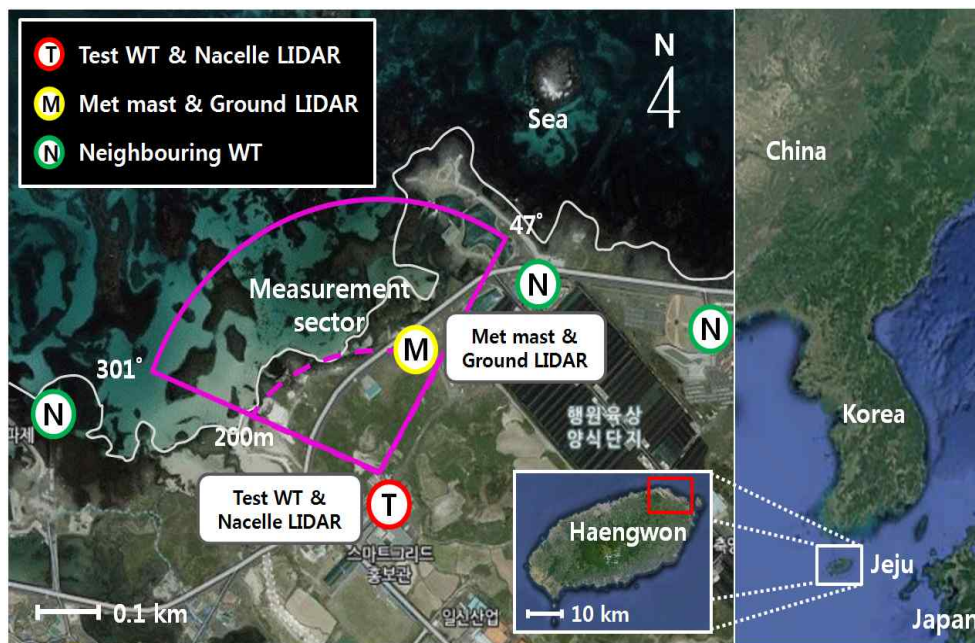
Fig. III-1 Location of Jeju Island including the layout of wind turbines and instruments at the Haengwon wind farm

Fig. III-2 shows the schematic for the wind turbine power performance measurement for this work. A nacelle LiDAR consists of two devices: an optical head (OH) and a processing unit (PU). The nacelle LiDAR measurements by laser beams horizontally emitted by the OH were saved in the PU. The wind data measured by laser beams vertically emitted from the ground LiDAR were recorded to the data storage device in the main body with meteorological data such as air temperature, humidity, and pressure. A variety of meteorological data measured by sensors on a met mast were acquired by the data logger. All data collected by each instrument were transferred to the main data acquisition system (DAQ) in the test wind turbine tower base by the controller area network (CAN) communication. The time series of the data were then synchronized in the main DAQ. Additionally, the active electric power was measured by a current transformer (CT) and a power transducer (PT) at the bottom of the test wind turbine, and it was collected in the main DAQ.
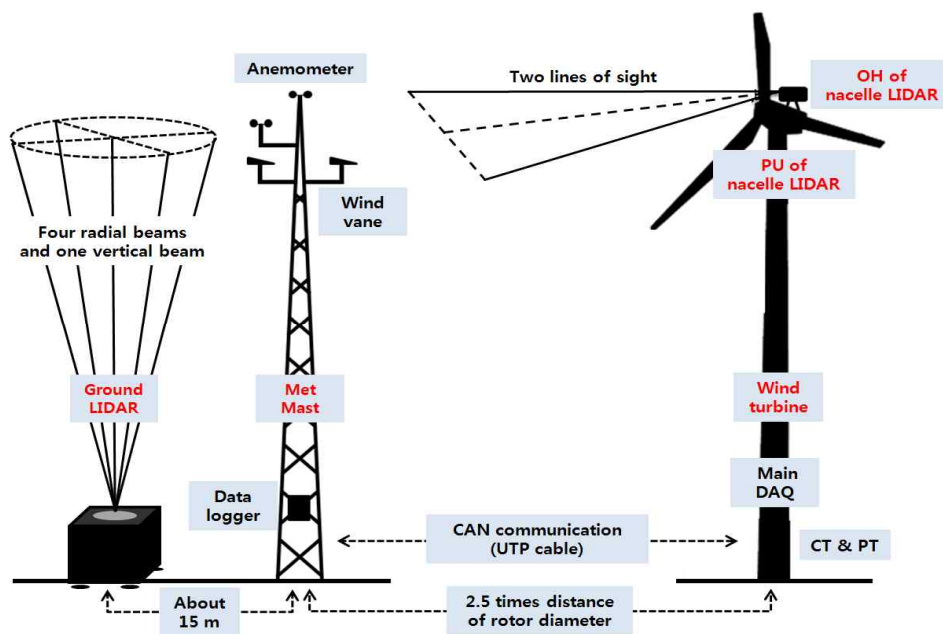
Fig. III-2 Schematic diagram of the wind turbine power performance test

(2) Measurement sector

To eliminate the wind data disturbed by the wake effects due to blade rotations of neighboring wind turbines and some obstacles, the measurement sector, α, was calculated using the following equations [26]:

$$D_e = \frac{2\,l_h\,l_w}{l_h + l_w} \qquad \text{(III-1)}$$

$$\alpha = 1.3\tan^{-1}(2.5D_e\,/\,L_e + 0.15) + 10 \qquad \text{(III-2)}$$

$$= 1.3\tan^{-1}(2.5\,D_n\,/\,L_n + 0.15) + 10$$

where D_e is the equivalent rotor diameter, l_h is height of the obstacle, and l_w is the width of obstacle. D_n is the rotor diameter of a nearby wind turbine and both L_e and L_n are distances from the neighboring wind turbine and obstacle, respectively. The calculated measurement sector was from 301° to 47°, as presented in Fig. III-1.

(3) Terrain evaluation

To test the power performance of wind turbines, the terrain evaluation should be conducted and meet the requirements proposed in Annex B of IEC 61400-12-1. If the requirements are not satisfied, site calibration should be conducted. Thus, the terrain conditions were evaluated, as shown in Fig. III-3. The terrain conditions within the distances of L, 2L, 4L, 8L and 16L were estimated in terms of the maximum slope and terrain variation from the plane. Here, L is the distance between a test wind turbine and a met mast. Table III-1 presents the results. The values obtained for the maximum slope and terrain variation under each condition are met, which means that no site calibration is required.
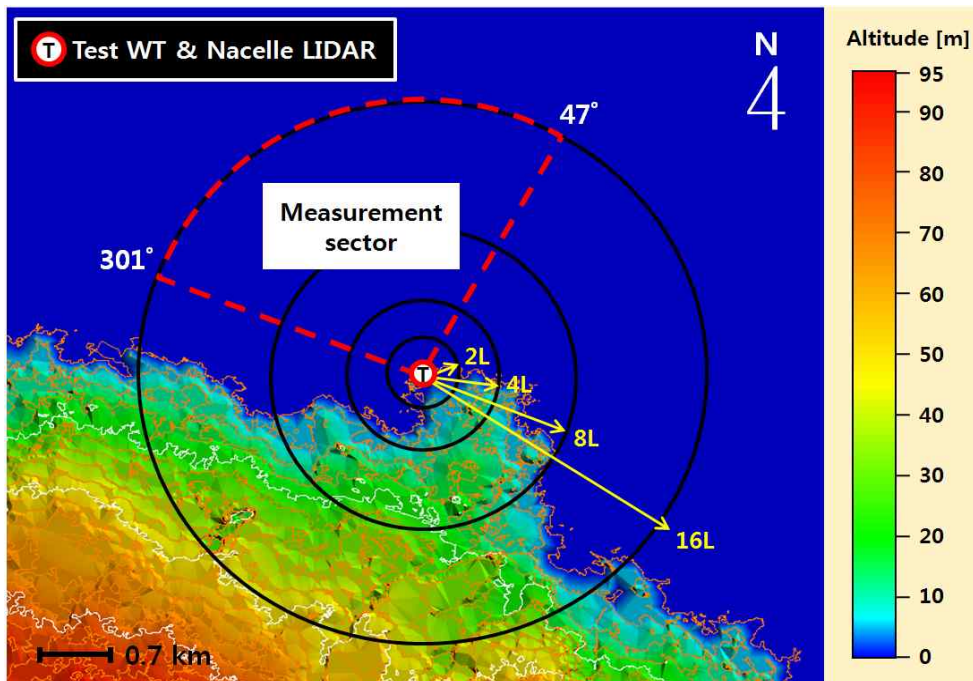
Fig. III-3 Measurement sector and region for terrain evaluation for the test wind turbine at the Haengwon wind farm

Table III-1 Terrain evaluation results for the Haengwon wind farm

Distance	Sector	Maximum slope [%]	Maximum terrain variation [m]	Note
<2L	360°	1.35 < 3	5.04 < 1/3(H-0.5D)	
≥2L and <4L	Measurement sector	0 < 5	0 < 2/3(H-0.5D)	Offshore area
≥2L and <4L	Outside measurement sector	0.83 < 10	Not applicable	
≥4L and <8L	Measurement sector	0 < 10	0 < (H-0.5D)	Offshore area
≥8L and <16L	Measurement sector	0 < 10	Not applicable	Offshore area

* H: 70 m, D: 70 m

2) Test wind turbine

A 1.5 MW wind turbine was selected for testing. Fig. III-4 shows the test wind turbine, and Table III-2 lists its specifications. The hub height and rotor diameter are both 70 m above ground level with a rated RPM of 17.02.

Fig. III-4 View of test wind turbine at the Haengwon wind farm

Table III-2 Specifications of the test wind turbine at the Haengwon wind farm

Items	Description
Model	HJWT 1500
Rated power	1500 kW
IEC class	IIA
Hub height	70 m
Rotor diameter	70 m
Swept area	4657 m^2
Rated RPM	17.02 rpm
Blade control	Pitch control
Cut-in / rated / cut-out wind speed	3.5 / 13 / 25 m/s

Fig. III-5 shows the CT and the PT installed at the bottom of the test wind turbine, and Table III-3 presents their specifications. The electric power measurement instruments of class 0.5 were used to satisfy the requirements provided in the IEC standard.

Fig. III-5 Current transformer and power transducer

Table III-3 Specifications of electric power measurement instruments in the test wind turbine at the Haengwon wind farm

Items	Current transformer	Power transducer
Model	BC 1009	P 530
Measurement range	3000 A	100-690 V / 1-6 A
Resolution	Ratio = 3000 : 5	4-20 mA output
Accuracy	Class 0.5	Class 0.5

3) Measurement instruments

(1) 2-beam nacelle LiDAR

The 2-beam nacelle LiDAR was used for this work, as shown in Fig. III-6, and its specifications are listed in Table III-4. The nacelle LiDAR is the Wind Iris 1st edition developed by Avent. It measures free-stream wind speed in front of the turbine rotor by emitting two laser beams as a stream of pulses with two LOS, separated by a horizontal angle of 30°. The nacelle LiDAR can measure wind speed at up to 10 points ranging between 80 m to 400 m horizontally from the nacelle [94]. In this work, the nacelle LiDAR wind data at eight points from 80 m to 360 m with 40 m interval were used for characteristics analysis of the nacelle LiDAR measurements, and the nacelle LiDAR measurements at 2.5 times the rotor diameter from wind turbine no. 1 were analyzed for wind turbine power performance testing.

This nacelle LiDAR was calibrated through a collaborative research project with the Korea Testing Laboratory (KTL) according to procedures suggested by Technical University of Denmark (DTU) [74, 75]. The calibration was conducted for LOS beams and RWS of the nacelle LiDAR, and the calibration result was verified by linear regression analysis with wind speed data measured from an 80 m tall met mast. As a result, the correlation had a slope of 1.01 and a coefficient of determination of 0.99.

Through dedicated software provided by the manufacturer, it is possible to remotely configure the measurement condition and to export the data. The wind data, such as wind speed, wind direction, and carrier-to-noise ratio (CNR) signals were monitored in real time for the measurement period, as shown in Figs. III-7 and III-8. The CNR will be dealt with in detail in the next section.

Fig. Ⅲ-6 2-beam nacelle LiDAR on a test wind turbine at the Haengwon wind farm

Table Ⅲ-4 Specifications of the 2-beam nacelle LiDAR

Items	Description
Model	Wind Iris 1st edition
Measurement range	80 to 400 m
Data sampling rate	1 to 2.5 Hz
No. of measurements	10
Laser source	Fibre pulsed laser 1.54 μm
Speed accuracy	0.1 m/s
Speed range	-10 to 40 m/s
Direction accuracy	± 0.5°
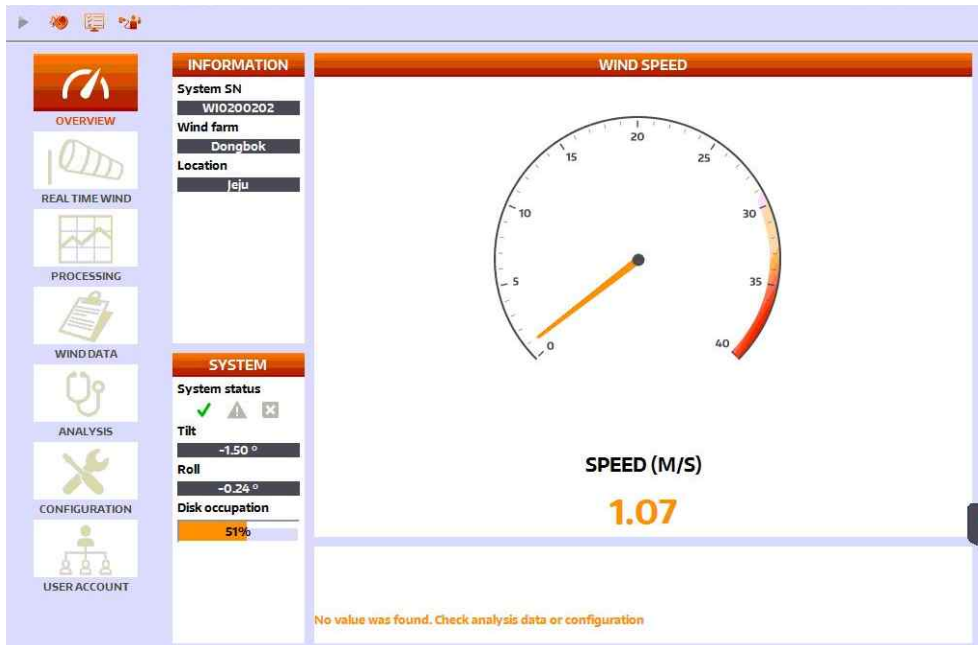
Fig. III-7 Real time monitoring of the nacelle LiDAR wind data
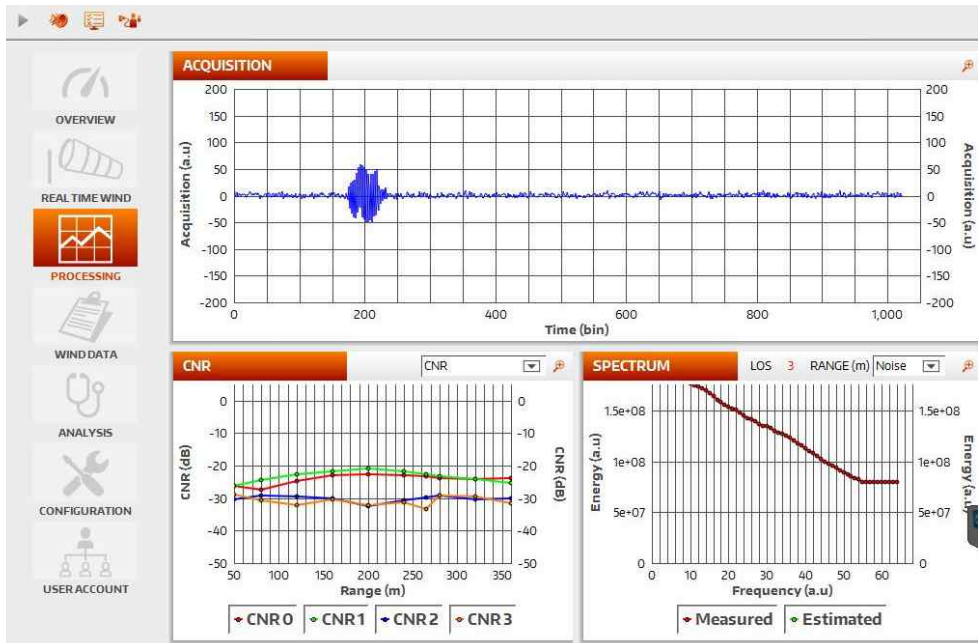
Fig. III-8 Real time monitoring of the status of nacelle LiDAR data processing

For an accurate measurement, the nacelle LiDAR should be well aligned with the wind turbine's rotor axis and leveled on the turbine roof; further, laser beams should not be blocked by the rotor blades or nacelle itself of the wind turbine, as shown in Fig. III-9. The OH is installed on the aligned tripod, and an inclinometer inside the OH is implemented to facilitate this leveling, providing tilt and roll values during operation of the system.
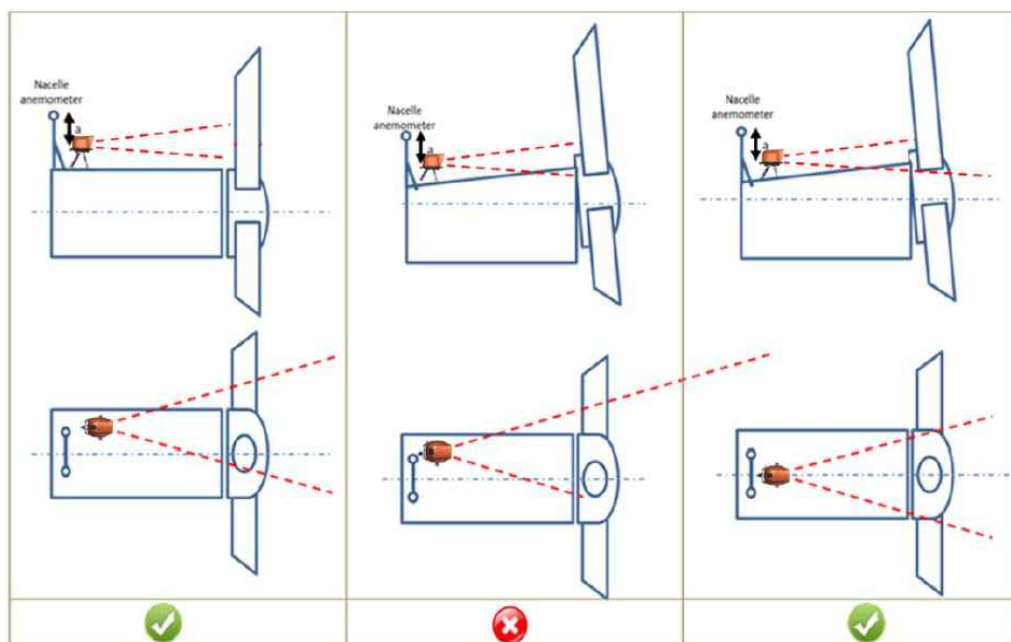
Fig. III-9 Proper positions of the nacelle LiDAR optical head [94]

Since the nacelle LiDAR is mounted on the nacelle of the turbine, and the measurement height of the nacelle LiDAR can be affected by the tower bends backwards owing to the strength applied by the wind on the rotor. Thus, the pre-tilt configuration has to be conducted. The tilt of the nacelle LiDAR has to be set to measure at below 2.5 % of the hub height at the measurement point considering the wind turbine bending, as presented Fig. III-10. The tilt angle, $\beta_{pretilt}$, can be calculated using Eq. III-3 [94]:

$$\beta_{pretilt} = -Arctan\left(\frac{Z_{pretilt} + 0.025\,H}{2.5D + L_{pretilt}}\right) \qquad (III-3)$$

where $Z_{pretilt}$ and $L_{pretilt}$ are the distance from the OH of the nacelle LiDAR to the rotor axis and the rotor plan, respectively. H and D are the hub height and the rotor diameter of the wind turbine, respectively. The pre-tilt value of the nacelle LiDAR configured for this work was -1.45°.
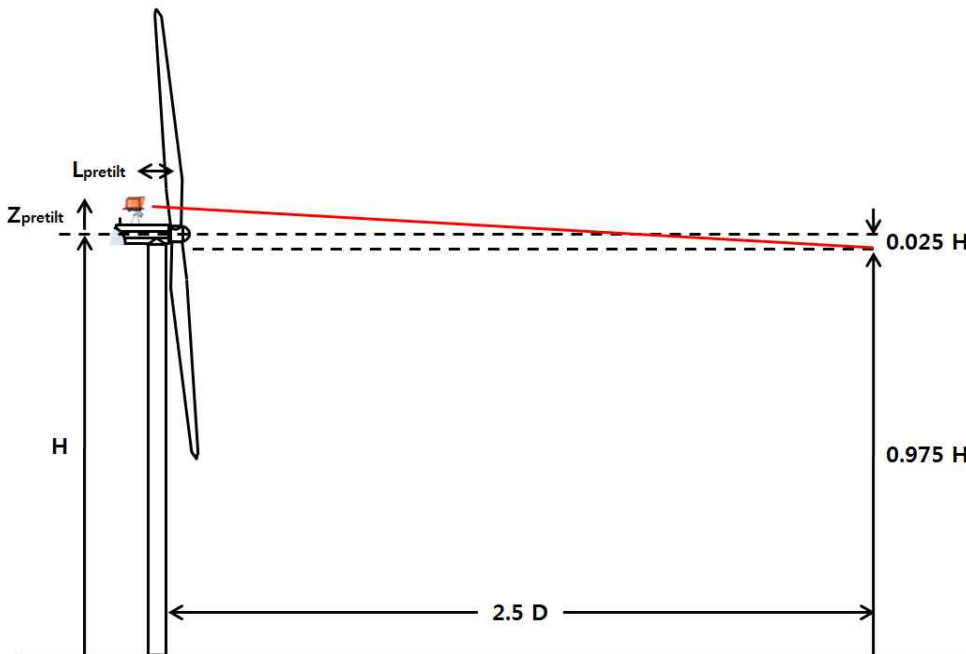
Fig. III-10 Configuration for pre-tilt adjustment

(2) Ground LiDAR

The ground LiDAR used in this work is Windcube v2 developed by Leosphere, as presented in Fig. Ⅲ-11. Table Ⅲ-5 lists its specifications. It measures the wind conditions by vertically emitting five laser beams, and it can measure at up to 12 points, at heights ranging from 40 m to 200 m above the ground level [95]. To derive REWS, the ground LiDAR measurements at seven heights from 40 m to 100 m with 10 m interval were used.

Fig. Ⅲ-11 Ground LiDAR installed at the Haengwon wind farm

Table Ⅲ-5 Specifications of the ground LiDAR installed at the Haengwon wind farm

Items	Description
Model	Windcube v2
Measurement range	40 to 200 m
Data sampling rate	1 Hz
No. of measurements	12
Laser source	Pulsed Doppler heterodyne
Wind speed measurement range	0 to 55 m/s

Through a dedicated communication network provided by the manufacturer, it is possible to remotely configure the measurement condition and to export the data. The wind data such as wind speed, direction, and CNR signals were monitored in real time for the measurement period, as illustrated in Figs. III-12 and III-13.
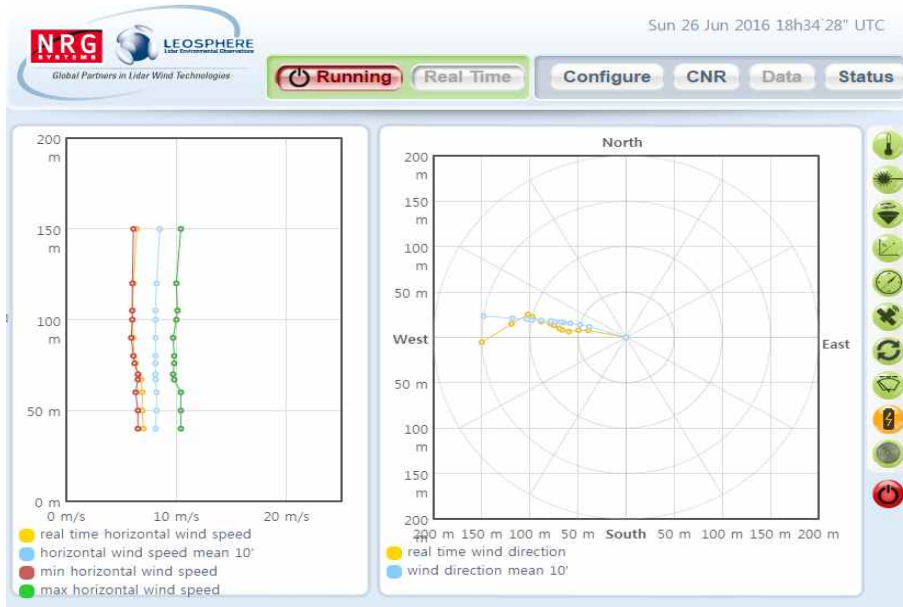
Fig. III-12 Real time monitoring of ground LiDAR wind data

Fig. III-13 Real time monitoring of CNR signals from the ground LiDAR

(3) Met mast

Fig. III-14 shows the met mast used for this work, and Table III-6 lists the specifications of the meteorological sensors and the data logger on the met mast. An 80 m high lattice type met mast was installed to test the power performance of a wind turbine. The wind speed data were collected by a Thies first class cup anemometer installed at the hub height. The met mast wind data were used as reference values for verifying the reliability of the nacelle LiDAR measurements and the PC_{NL}.

Moreover, the air temperature, pressure and humidity data near the hub height were used for normalization of the specific air density at the test site. The air density, ρ_{10min}, can be taken using Eq. III-4:

$$\rho_{10min} = \frac{1}{T_{10min}} \left(\frac{B_{10min}}{R_0} - \phi \, P_W \left(\frac{1}{R_0} - \frac{1}{R_W} \right) \right) \qquad \text{(III-4)}$$

where T_{10min} and B_{10min} are the measured absolute air temperature and air pressure averaged over 10-minute, respectively. R_0 is the gas constant of dry air 287.05 J/kgK. ϕ is the relative humidity (range 0 to 1). R_W and P_W are the gas constant of water vapor and the vapor pressure, respectively.

Fig. III-14 Met mast installed at the Haengwon wind farm

Table III-6 Specifications of the met mast installed at the Haengwon wind farm

Items	Models	Accuracy	Height
Anemometer	Thies S11100	1 %	70 m
Wind vane	Thies S52100	0.5°	67 m
Temperature	Galltec P6312P	0.2 K	65 m
Humidity	Galltec P6312	1 %	65 m
Pressure	Vaisala PTB 110	± 0.6 hPa	75 m
Data logger	Ammonit meteo-40L	-	1 m

2. Characteristics analysis of 2-beam nacelle LiDAR measurements

To establish the standard of nacelle LiDAR data filtering, the characteristics of nacelle LiDAR measurements were analyzed by dividing them into three parts, which are weather conditions, mechanical movement and nacelle LiDAR availability.

1) Definition of CNR

The CNR represents the carrier-to-noise ratio, it is defined as the ratio of the received modulated carrier signal power, P_c, to the received noise power, P_n, after the receiver filters.

$$CNR\ [dB] = 10\ \log_{10}\left(\frac{P_c}{P_n}\right) \qquad\qquad (\text{III-5})$$

The CNR is one of the main parameters that can be used to flag LiDAR measurements as valid. It depends on the concentration of aerosols in the atmosphere that backscatter laser light, and its level also depends on weather conditions. In other words, a high atmospheric backscatter coefficient leads to high CNR.

The CNR threshold is the limit below which the measured data are not considered as reliable. According to LiDAR user manuals [94, 95], LiDAR measurements with a CNR threshold less than –23 dB should to be excluded because the measurement sensitivity is weak as CNR decreases.

Fig. Ⅲ-15 presents the max, min, mean, and standard deviation of the CNR for the measurement period. The mean CNR varied from ‐10 dB to ‐18 dB; it had its highest value at 200 m and its value reduced as the distance increased.
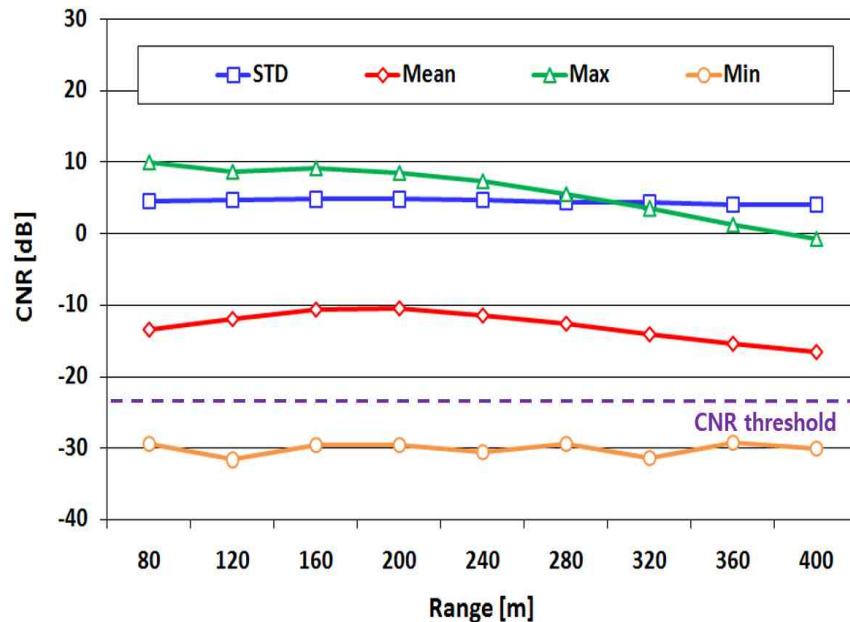
Fig. Ⅲ-15 Max, min, mean, and standard deviation of CNR signals of a 2‐beam nacelle LiDAR

2) Characteristics analysis of 2‐beam nacelle LiDAR measurements

(1) CNR variation with weather conditions

CNR variations were analyzed according to the following weather conditions: air temperature, humidity, and air pressure. The analysis conditions were as follows:

- temperature of 10 ℃ with a bin interval between 0 ℃ and 40 ℃;
- humidity of 20 % with a bin interval between 21 % and 100 %;
- pressure of 20 hPa with a bin interval between 940 hPa and 1020 hPa.

Figs. III-16 to III-18 present the results. In general, the CNRs have their highest value at distances between 160 m and 200 m, and their value reduces as distance increases beyond 200 m. Under the temperature condition, the CNR was the highest between 21 °C and 30 °C and it did not display a sequential trend. For the humidity condition, the CNR becomes gradually higher with an increase in humidity. For the pressure condition, unlike the temperature condition, it has no consecutive trend with pressure variation. However, the CNRs were in a normal range, i.e., their value was greater than ‐23 dB in all conditions, which means that various weather conditions did not affect the nacelle LiDAR measurement.
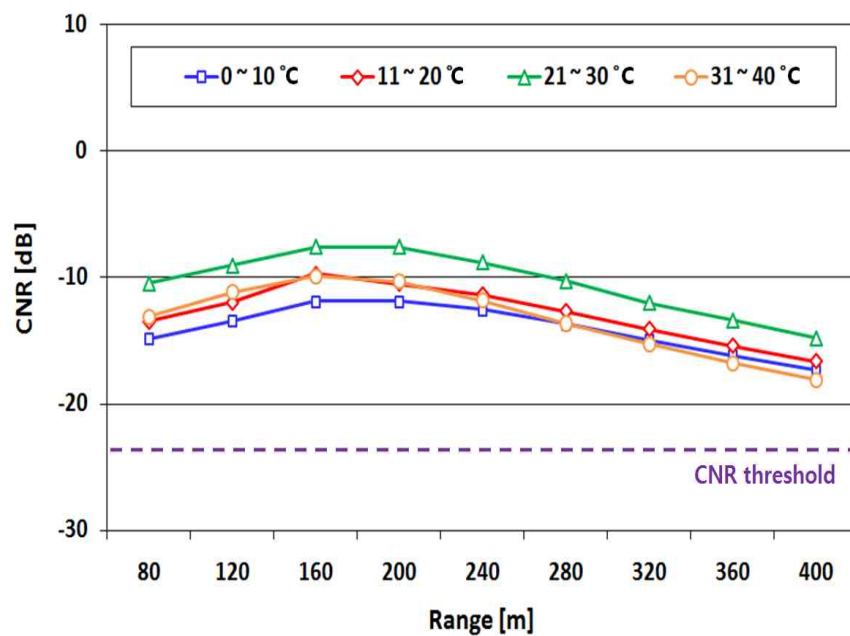
Fig. III-16 Variation in the CNR of 2-beam nacelle LiDAR with temperature
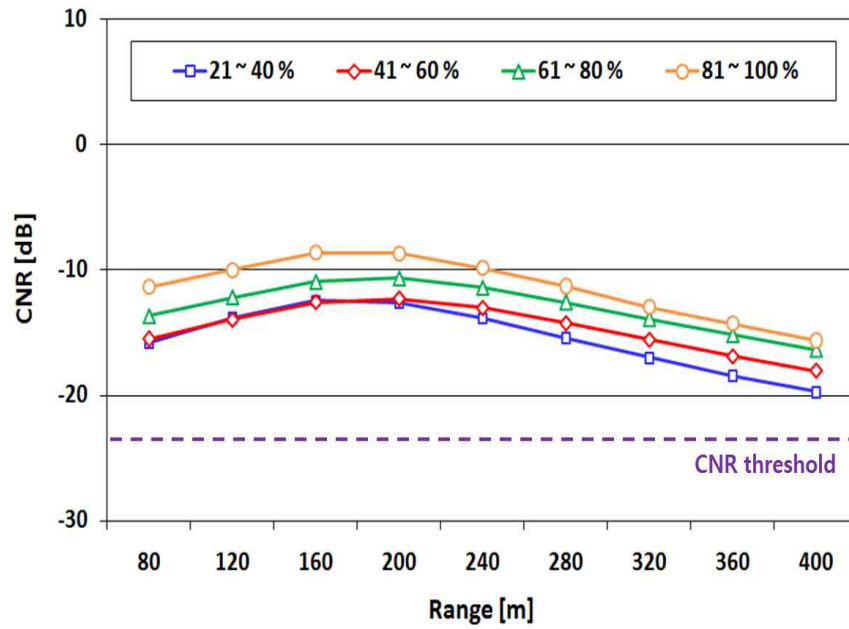
Fig. III-17 Variation in the CNR of 2-beam nacelle LiDAR with humidity
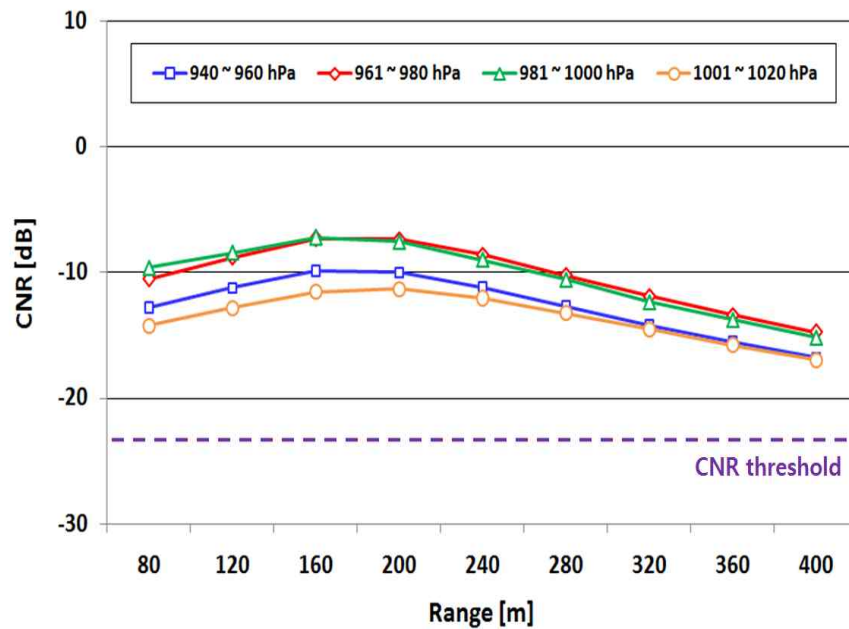
Fig. III-18 Variation in the CNR of 2-beam nacelle LiDAR with pressure

Additionally, the CNR variation with the amount of precipitation was analyzed. A user manual for the ground LiDAR recommends exclusion of data corresponding to a daily precipitation of more than 10 mm [95]. Thus, the CNR variation when the daily precipitation is more than 10 mm was investigated for a certain period during the observation period. Fig. III-19 presents the result. Despite the occurrence of a high precipitation of up to 55 mm, it was confirmed that the CNR signals were in the normal range, which means that the precipitation did not affect the nacelle LiDAR measurement.
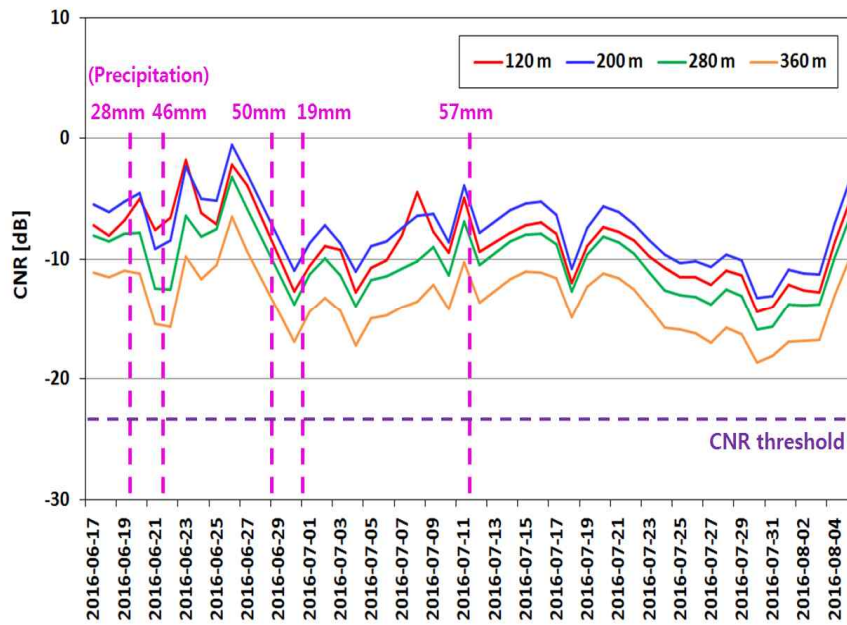
Fig. III-19 Variation in the CNR of 2-beam nacelle LiDAR with the amount of precipitation

(2) CNR variation with mechanical movement

The nacelle LiDAR is mounted behind the rotor blades of a wind turbine, thus implying that the nacelle LiDAR measurements could be affected by rotation of rotor blades. The rotor RPM data of the test wind turbine measured from SCADA system were used for analyzing the CNR variation with rotation of rotor blades.

Fig. III-20 shows the CNR variation with rotor RPM. The rated RPM of the test wind turbine is 17.02 rpm. Although the CNR decreased up to 20 dB at near the rated RPM, almost all the CNR signals were generally measured within a normal range higher than the CNR threshold of -23 dB. Therefore, it was confirmed that rotation of rotor blades did not affect normal measurement of a nacelle LiDAR.

Fig. III-21 presents the standard deviation of the CNR with rotor RPM. The standard deviation of the CNR was in inverse proportion to rotor RPM and it was close to one as the rotor RPM increased except for the rated rotor RPM. In other words, the CNR variation was small as the rotor RPM increased. High standard deviations of CNR were caused by the number of data, and those were close to one after data filtering.
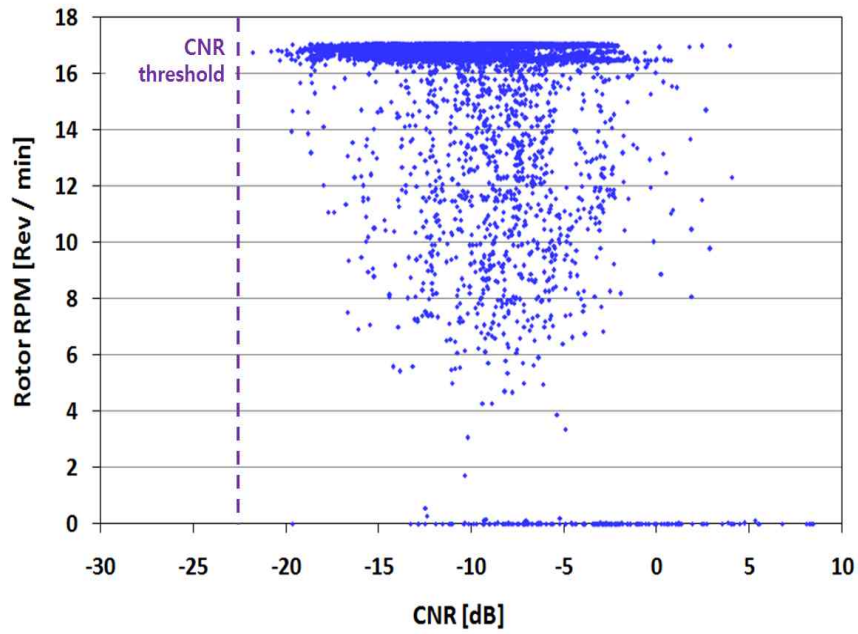
Fig. III-20 Variation in the CNR of 2-beam nacelle LiDAR with rotation of rotor blades
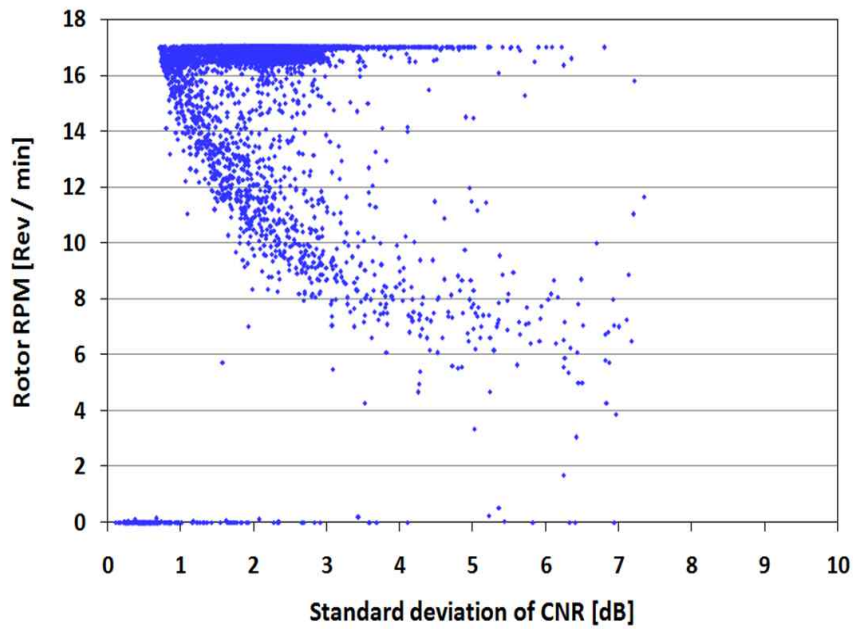
Fig. III-21 Standard deviation of the CNR of the 2-beam nacelle LiDAR with rotation of rotor blades

As described in Section 1.3.1 of Chapter III, the nacelle LiDAR measurement can be affected by the tower bends backwards owing to the strength applied by the wind on the rotor, thus implying that the nacelle LiDAR tilts due to the motion of the wind turbine nacelle due to wind variation. Fig. III-22 shows the nacelle LiDAR measurement error with tilt angle variation under conditions following the rated wind speed of the test wind turbine. Here, the nacelle LiDAR measurement error is defined as a difference in wind speeds measured by nacelle LiDAR and cup anemometer. Although the initial tilt value of ‐1.45° was varied within the range between ‐0.8° and ‐1.8°, the nacelle LiDAR measurement error was close to 0. Thus, it was confirmed that the tilt variation did not affect the measurement accuracy of nacelle LiDAR.
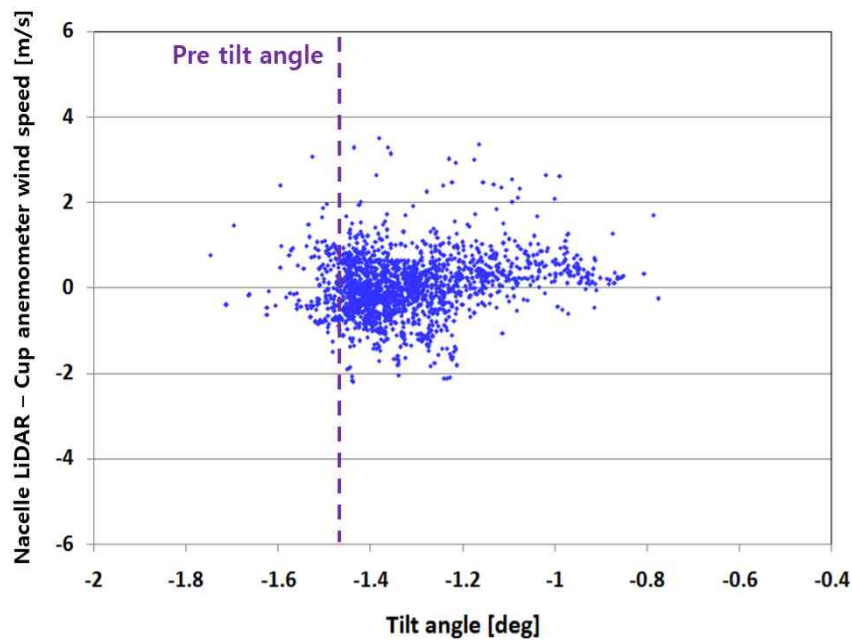
Fig. III-22 2-beam nacelle LiDAR measurement error with tilt angle variation

(3) Data accuracy with data availability

Fig. III-23 illustrates the nacelle LiDAR measurement error with data availability. Here, the nacelle LiDAR measurement error means the difference between the nacelle LiDAR and cup anemometer wind speeds. The measurement error was close to 0 when the data availability was higher. In this work, the nacelle LiDAR measurements with data availability of more than 80 % were considered as reliable wind data. It was confirmed that the data share when the availability was more than 80 % was 91.9 %.
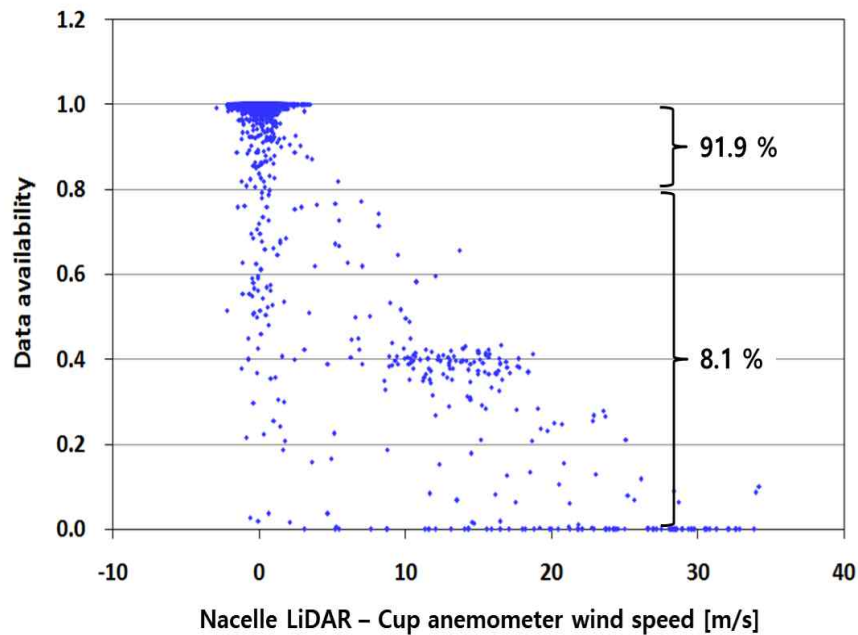
Fig. III-23 2-beam nacelle LiDAR measurement error with data availability

3. Data rejection and reliability verification

According to the analysis results of the characteristics of nacelle LiDAR measurements with weather conditions, mechanical movement and data availability, the nacelle LiDAR measurements were simultaneously rejected with other data, as follows:

- data without a measurement sector;
- data with nacelle and ground LiDAR availabilities of less than 80 %;
- data with a CNR of less than ‑23 dB;
- data when the nacelle and ground LiDARs were in abnormal operation;
- data when the test wind turbine was in abnormal operation.

To verify the reliability of selected LiDAR data after data filtering, linear regression analysis was conducted with cup anemometer wind speed. Fig. III‑24 shows the result of linear regression analysis between nacelle LiDAR and cup anemometer wind speeds. The correlation between them was a slope of 0.984 with a coefficient of determination of 0.970. Fig. III‑25 presents the result of linear regression analysis between ground LiDAR and cup anemometer wind speeds. The slope and coefficient of determination were 0.982 and 0.964, respectively. Thus, it was confirmed that the data were reliable and properly rejected.
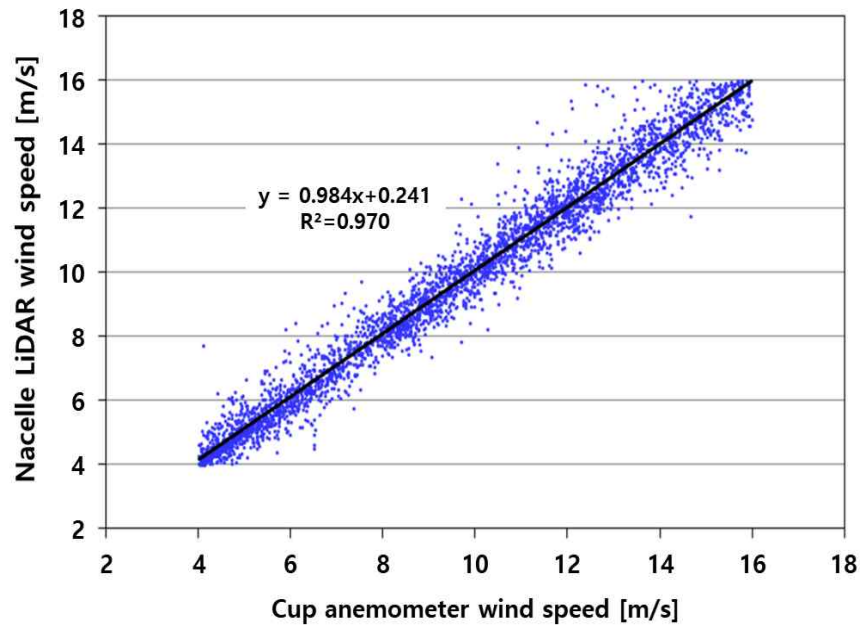
Fig. III-24 Linear regression analysis between wind speeds measured by 2-beam nacelle LiDAR and the cup anemometer at the Haengwon wind farm
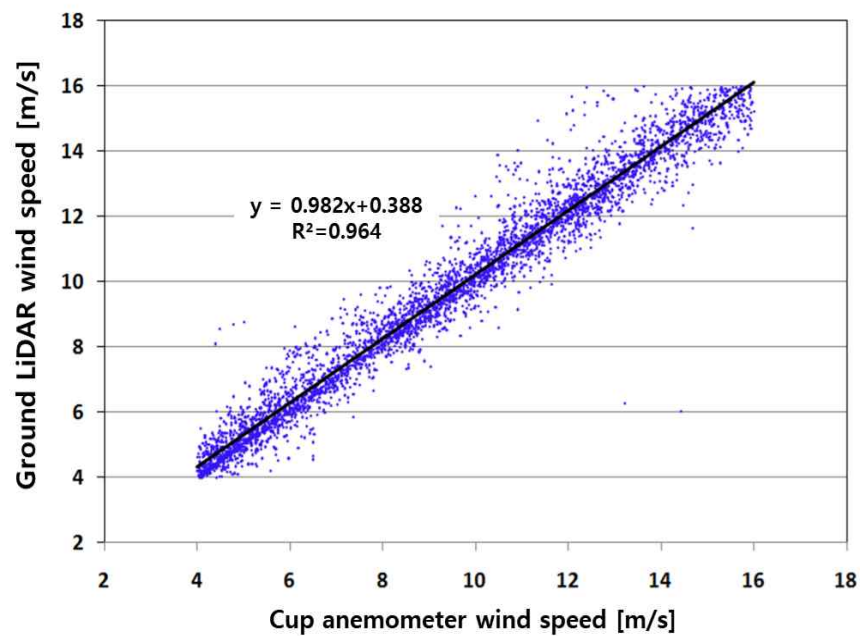
Fig. III-25 Linear regression analysis between wind speeds measured by a ground LiDAR and the cup anemometer at the Haengwon wind farm

Fig. III-26 shows the mean value with a bin interval of 1 m/s and scatter plot of the nacelle LiDAR measurement error. In all regions, the nacelle LiDAR measurement errors were close to 0, and the mean value varied from -0.20 m/s to 0.16 m/s with a median of 0.09 m/s. In addition, the standard deviations of the nacelle LiDAR measurement error were from 0.38 m/s to 0.73 m/s with a median of 0.61 m/s.
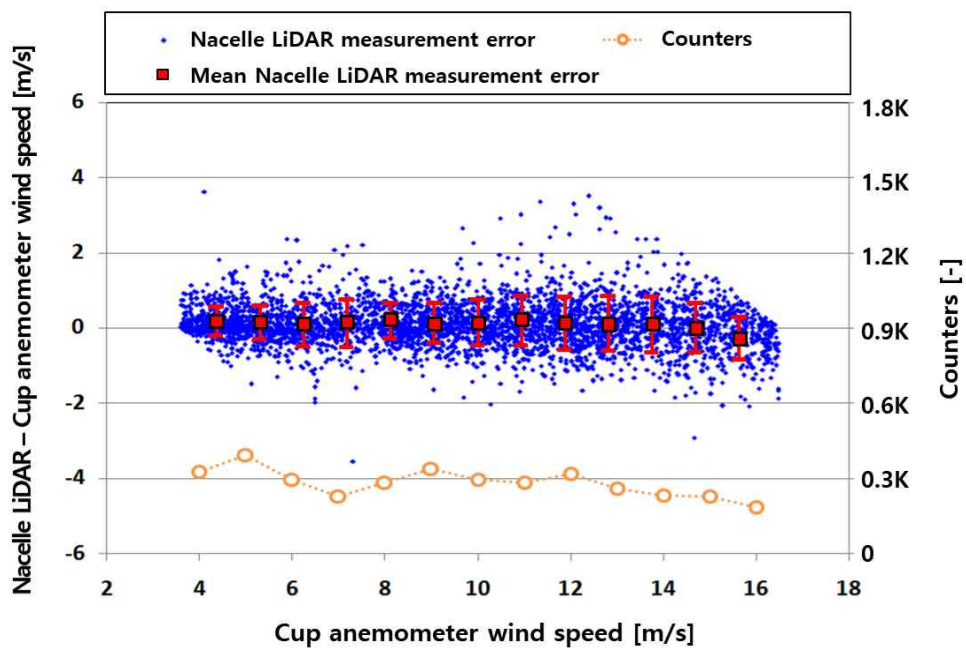
Fig. III-26 2-beam nacelle LiDAR measurement error and number of data points

4. REWS derivation using a ground LiDAR

1) Concept of REWS

Because the wind shear exponents have increased as large wind turbines with a hub height over 100 m have been manufactured, the hub height wind speed is no longer the representative wind speed to test the power performance of wind turbines. Thus, power performance testing using REWS was introduced in IEC 61400-12-1 2nd edition. REWS is defined as the wind speed corresponding to the kinetic energy flux through the swept rotor area when accounting for the variation in the wind speed with height. That is, it is corrected wind speed taking account into the wind shear for an entire swept area of a wind turbine rotor. To apply the wind shear correction, the wind speed measurement for a minimum of three heights was required as follows (It is recommended to measure at as many measurement heights as possible to minimize wind speed uncertainty) [28]:

- H ± 1.0 %;
- between H-R and H - 2/3R;
- between H+2/3R and H+R.
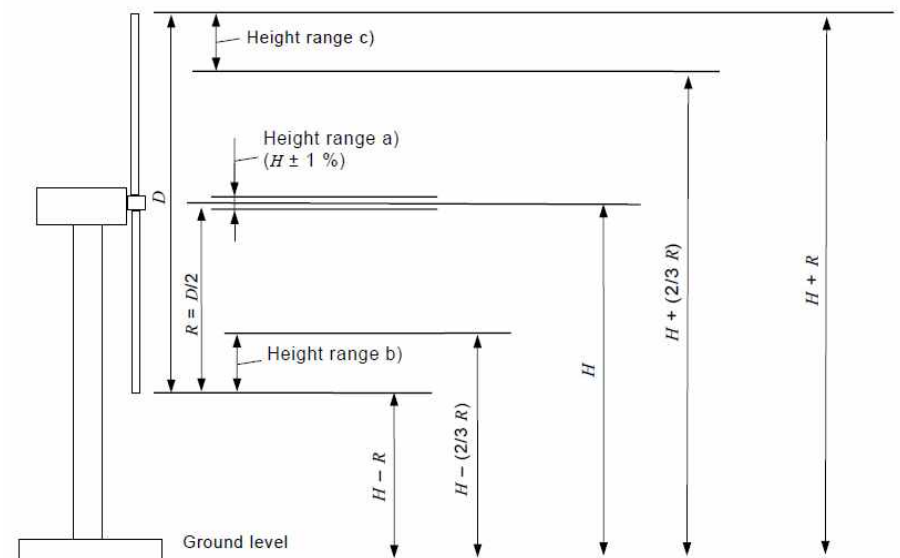
Fig. III-27 Wind shear measurement heights required for REWS derivation [28]

2) REWS derivation

For wind measurement over the hub height, the ground LiDAR has been generally used. In this work, the ground LiDAR wind speeds at seven measurement heights were used with a cup anemometer wind speed at the hub height for REWS derivation, as shown in Fig. III-28. The REWS, v_{eq}, was derived using following equations:

$$v_{eq} = \left(\sum_{i=1}^{n_h} v_i^3 \frac{A_i}{A} \right)^{1/3} \tag{III-6}$$

$$A_i = \int_{z_i}^{z_i+1} c(z)\, dz = g(z_{i+1}) - g(z_i) \tag{III-7}$$

$$c(z) = 2\sqrt{R^2 - (z-H)^2} \tag{III-8}$$

$$g(z) = (z-H)\sqrt{R^2 - (z-H)^2} + R^2 \tan^{-1}\left(\frac{z-H}{\sqrt{R^2 - (z-H)^2}} \right) \tag{III-9}$$

where n_h is the number of measurement heights, v_i is the wind speed measured at height i, A is the swept area by the rotor and A_i is the area of the i-th segment, z_i is the height of the i-th segment separation line, and g(z) is the integrated function.

A wind shear correction factor, $f_{r,RSD}$, is defined as the ratio of the REWS to the wind speed measured at the hub height. The final REWS, $v_{eq,final}$, is calculated by Eq. III-10:

$$v_{eq,final} = f_{r,RSD}\, v_{h,MM} \tag{III-10}$$

where $v_{h,MM}$ is the cup anemometer wind speed at hub height.

제주대학교 중앙도서관
JEJU NATIONAL UNIVERSITY LIBRARY
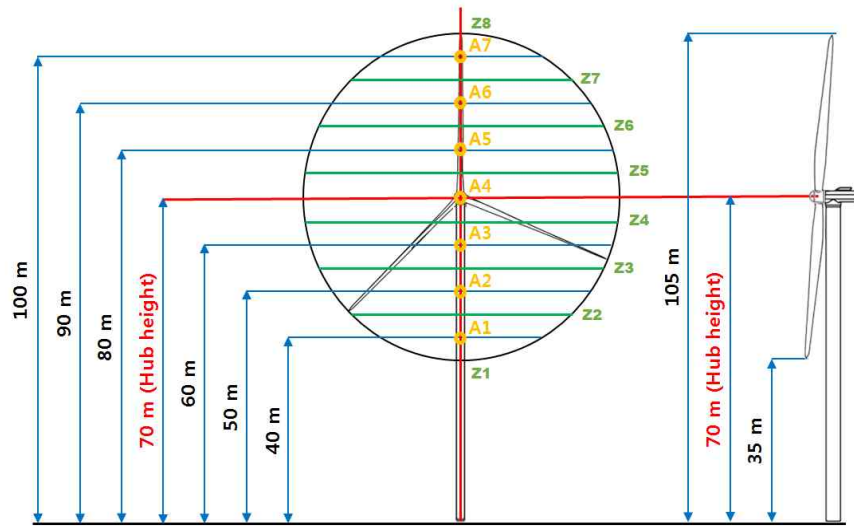
Fig. III-28 Schematic of REWS calculation

3) Reliability verification of REWS

Fig. III-29 presents the result of linear regression analysis between $v_{eq,final}$ and the cup anemometer wind speed. Although their correlation was very high, the slope and coefficient of determination were 0.995 and 0.999, respectively, there is clearly a difference between wind speeds before and after correcting for wind shear.
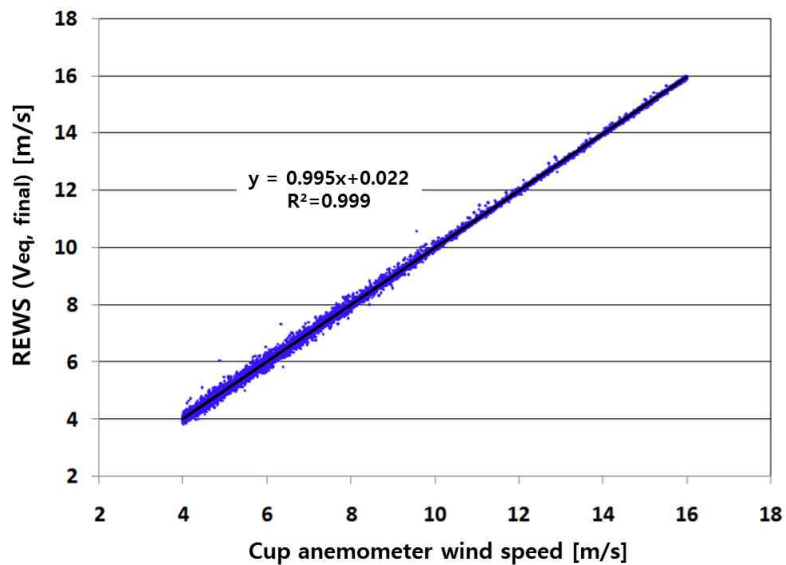
Fig. III-29 Linear regression analysis between final REWS and cup anemometer wind speed

5. Wind turbine power performance measurement using a nacelle LiDAR

1) Comparison of power outputs

Figs. III-30 to III-32 present the scatter plots of the power output by the cup anemometer, REWS and nacelle LiDAR measurements, respectively. In the figures, P_m and P_r mean the measured and the rated power outputs of the test wind turbine, respectively; V_{Cup} and V_{NL} denote the cup anemometer and nacelle LiDAR wind speeds, respectively; and V_{REWS} and V_r represents the REWS and the rated wind speed of the test wind turbine, respectively.

In Figs. III-30 and III-31, the power outputs by the cup anemometer and the REWS are similar. On the other hand, the power outputs by the nacelle LiDAR show a smaller scatter than the others, as illustrated in Fig. III-32. The reason for the different power output scatter plots may be the difference in the method of measuring the wind speed with each instrument: the cup anemometer wind speed is measured by the met mast fixed at a point irrespective of wind direction variation, while the nacelle LiDAR measurements is measured in front of the wind turbine rotor with nacelle yawing according to wind direction variation. Thus, correct power outputs corresponding to specific wind speeds could be obtained with the nacelle LiDAR. However, the wind measurement by the cup anemometer on a met mast fixed at a point may lead to a deviation in wind speed for the power output due to the fact that it cannot reflect the wind coming towards the wind turbine rotor. This result is similar to the research result by Wagner et al. [77].
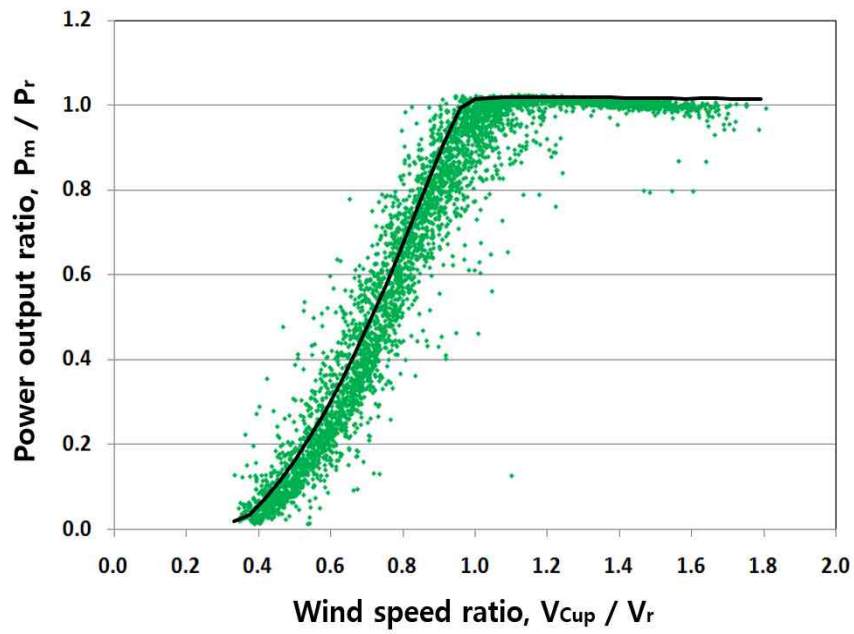
Fig. Ⅲ-30 Scatter plot of power output with cup anemometer wind speed and guaranteed power curve
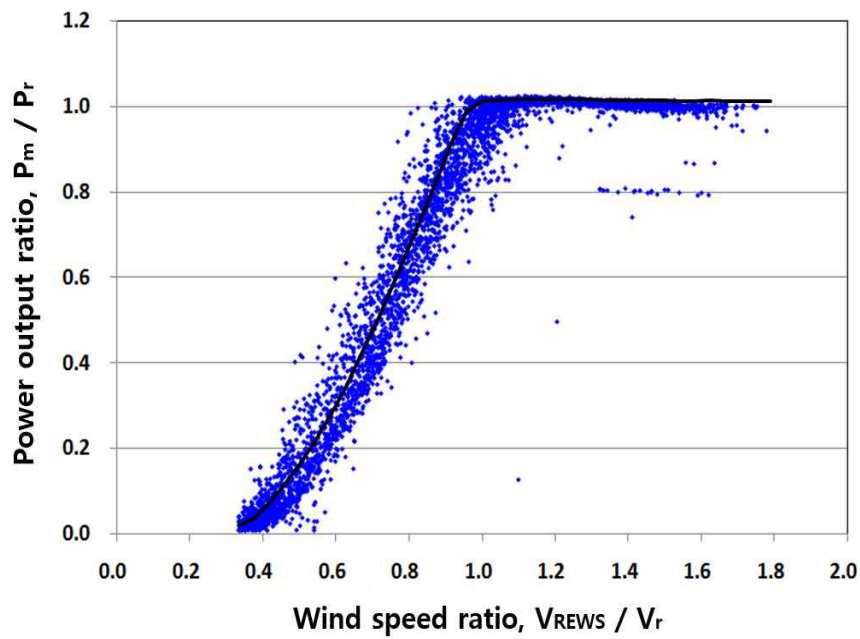
Fig. Ⅲ-31 Scatter plot of power output with REWS and guaranteed power curve
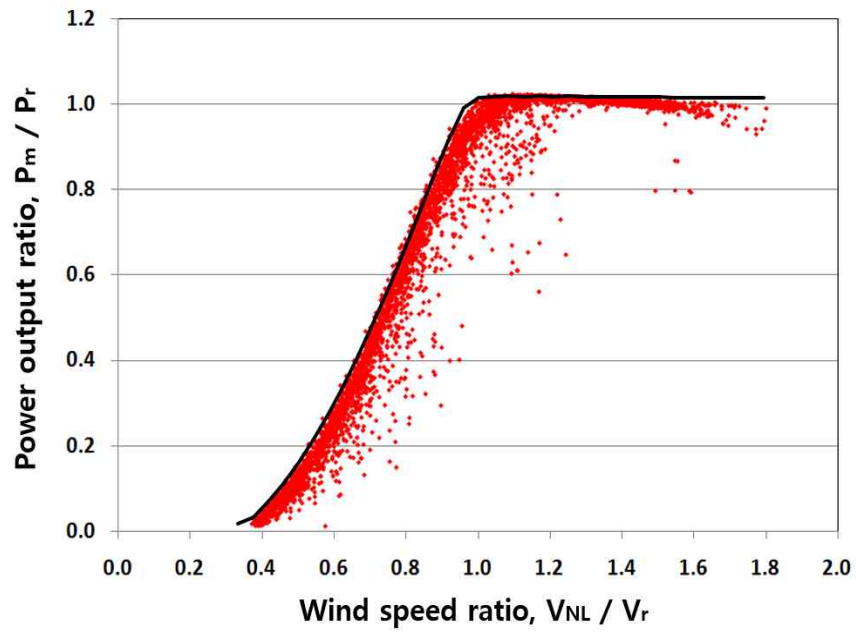
Fig. III-32 Scatter plot of power output with 2-beam nacelle LiDAR measurements and guaranteed power curve

To quantitatively clarify the difference in power outputs for each wind data set, the standard deviations of the power outputs were calculated by a bin interval of 0.5 m/s, as listed in Table III-7. The standard deviations of the power outputs by the cup anemometer wind speed and REWS were very similar; their mean standard deviations were 0.114 and 0.121, respectively. On the other hand, the standard deviation of the power output by the nacelle LiDAR measurements was lower than those of the others; its mean standard deviation was 0.039.

Table III-7 Standard deviations of power outputs by bin intervals

Interval [m/s]	Standard deviation [kW]			Interval [m/s]	Standard deviation [kW]		
	Cup	REWS	NL		Cup	REWS	NL
4.3 - 4.7	0.053	0.030	0.009	12.8 - 13.2	0.130	0.204	0.076
4.8 - 5.2	0.056	0.032	0.015	13.3 - 13.7	0.207	0.173	0.057
5.3 - 5.7	0.062	0.055	0.019	13.8 - 14.2	0.059	0.156	0.052
5.8 - 6.2	0.090	0.089	0.025	14.3 - 14.7	0.059	0.216	0.031
6.3 - 6.7	0.141	0.098	0.031	14.8 - 15.2	0.067	0.208	0.032
6.8 - 7.2	0.150	0.098	0.040	15.3 - 15.7	0.043	0.088	0.004
7.3 - 7.7	0.161	0.118	0.049	15.8 - 16.2	0.006	0.177	0.003
7.8 - 8.2	0.144	0.104	0.058	16.3 - 16.7	0.009	0.130	0.004
8.3 - 8.7	0.205	0.145	0.058	16.8 - 17.2	0.014	0.090	0.004
8.8 - 9.2	0.183	0.172	0.078	17.3 - 17.7	0.008	0.065	0.005
9.3 - 9.7	0.196	0.161	0.081	17.8 - 18.2	0.058	0.184	0.022
9.8 - 10.2	0.188	0.164	0.074	18.3 - 18.7	0.061	0.163	0.036
10.3 - 10.7	0.199	0.147	0.096	18.8 - 19.2	0.058	0.185	0.048
10.8 - 11.2	0.175	0.101	0.061	19.3 - 19.7	0.061	0.048	0.011
11.3 - 11.7	0.190	0.181	0.076	19.8 - 20.2	0.392	0.015	0.021
11.8 - 12.2	0.163	0.107	0.051	20.3 - 20.7	0.020	0.023	0.017
12.3 - 12.7	0.163	0.169	0.057	Mean	0.114	0.121	0.039

2) Comparison of power curves

Before drawing the power curves, the selected wind speeds were normalized to the reference air density at sea level to exclude the effect of wind variation on air density using Eq. III-11:

$$V_n = V_{10\min}\left(\frac{\rho_{10\min}}{\rho_0}\right)^{1/3} \qquad (\text{III-11})$$

where V_n is the normalized wind speed and $V_{10\min}$ is the measured 10-minute averaged wind speed. ρ_0 is the reference air density of 1.225 kg/m³.

The selected wind speed data normalized for the air density with the power output data were averaged by the bin method with an interval of 0.5 m/s using following equations:

$$V_i = \frac{1}{N_i}\sum_{j=1}^{N} V_{n,\,i,\,j} \qquad (\text{III-12})$$

$$P_i = \frac{1}{N_i}\sum_{j=1}^{N} P_{n,\,i,\,j} \qquad (\text{III-13})$$

where V_i and P_i are the normalized and averaged wind speed and power output in bin i, respectively. $V_{n,i,j}$ and $P_{n,i,j}$ are normalized wind speed and power output of data set j in bin i, respectively. N_i is the number of 10-minute data sets in bin i.

Additionally, the power coefficient, C_P, was calculated using Eq. III-14:

$$C_P = \frac{P_i}{\frac{1}{2}\rho_0\,A\,V_i^{\,3}} \qquad (\text{III-14})$$

Fig. Ⅲ-33 and Table Ⅲ-8 present the power curves and power coefficients of the cup anemometer, REWS, and nacelle LiDAR measurements. In the figure, V_m means the measured wind speeds, which are the cup anemometer, REWS and nacelle LiDAR measurements. Each power curve met the range requirements of the wind data from a cut-in wind speed to over 1.5 times the wind speed at 80 % of the rated power of wind turbine, and each bin had a minimum of three sampled data. The PC_{REWS} and the $C_{P,REWS}$ are almost the same as the PC_{Cup} and the $C_{P,Cup}$, respectively. Meanwhile, although PC_{NL} and $C_{P,NL}$ were similar to the others after the rated wind speed region, they were clearly lower than the others before the rated wind speed.
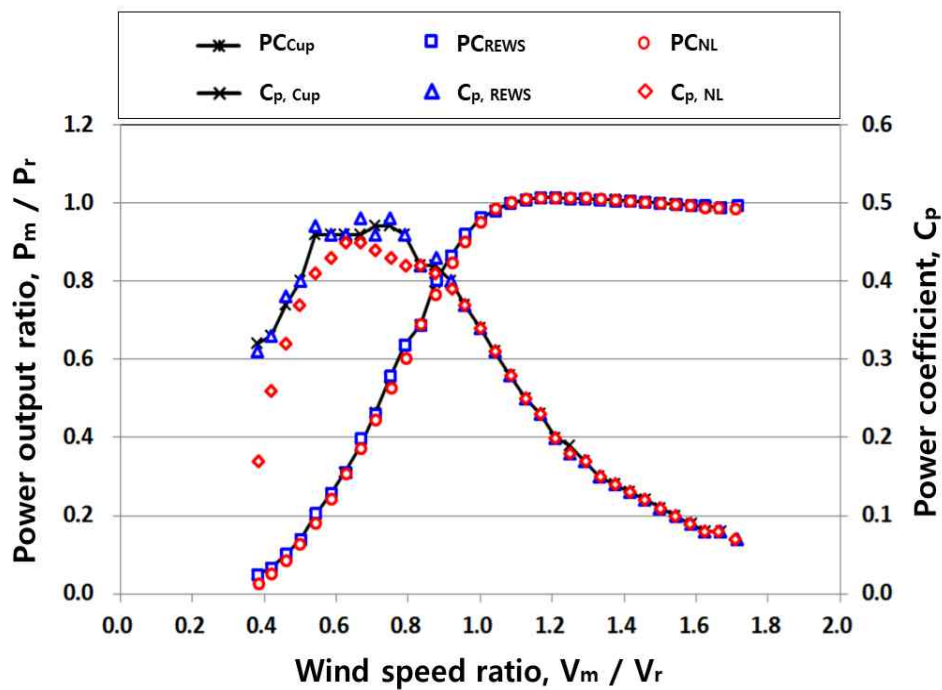
Fig. Ⅲ-33 Power curves and power coefficients for the test wind turbine at the Haengwon wind farm

Table III-8 Ratio between power curves and power coefficients for the test wind turbine at the Haengwon wind farm

Bin no.	Wind speed [m/s]	Ratio between NL and Cup			Ratio between NL and REWS		
		V_{NL} / V_{Cup}	P_{NL} / P_{Cup}	$C_{P,NL}$ / $C_{P,Cup}$	V_{NL} / V_{REWS}	P_{NL} / P_{REWS}	$C_{P,NL}$ / $C_{P,REWS}$
9	4.0	1.02	0.77	0.39	1.15	2.88	1.01
10	4.5	1.00	0.82	0.75	1.11	1.73	1.16
11	5.0	1.00	0.84	0.84	1.10	1.58	1.18
12	5.5	1.00	0.86	0.86	1.09	1.23	0.95
13	6.0	1.00	0.87	0.88	1.08	1.26	0.99
14	6.5	1.00	0.90	0.90	1.08	1.26	1.00
15	7.0	1.00	0.91	0.92	1.07	1.13	0.92
16	7.5	1.00	0.93	0.94	1.06	1.09	0.90
17	8.0	1.00	0.96	0.97	1.06	1.11	0.94
18	8.5	1.00	0.93	0.93	1.06	1.15	0.97
19	9.0	1.00	0.94	0.94	1.05	1.12	0.95
20	9.5	1.00	0.96	0.96	1.05	1.11	0.95
21	10.0	1.00	0.96	0.96	1.05	1.08	0.94
22	10.5	1.00	1.00	1.00	1.05	1.07	0.93
23	11.0	1.00	0.99	0.99	1.05	1.04	0.91
24	11.5	1.00	1.01	1.01	1.05	1.07	0.94
25	12.0	1.00	1.01	1.01	1.04	1.03	0.92
26	12.5	1.00	0.99	0.99	1.04	1.03	0.92
27	13.0	1.00	0.99	0.99	1.04	1.04	0.93
28	13.5	1.00	1.00	1.00	1.04	1.02	0.92
29	14.0	1.00	1.00	1.00	1.03	1.02	0.92
30	14.5	1.00	1.00	1.00	1.03	1.05	0.95
31	15.0	1.00	1.00	1.00	1.03	1.05	0.95
32	15.5	1.00	1.00	1.01	1.03	1.01	0.92
33	16.0	1.00	1.00	1.00	1.03	1.04	0.95
34	16.5	1.00	1.00	1.00	1.03	1.02	0.94
35	17.0	1.00	1.00	1.00	1.03	1.01	0.93
36	17.5	1.00	1.00	0.99	1.03	1.00	0.92
37	18.0	1.00	1.00	1.00	1.03	1.04	0.96
38	18.5	1.00	0.99	0.99	1.03	1.02	0.94
39	19.0	1.00	1.01	1.01	1.03	1.06	0.98
40	19.5	1.00	1.00	0.99	1.03	1.01	0.93
41	20.0	1.00	1.01	1.01	1.03	0.99	0.92
42	20.5	1.00	0.95	0.94	1.03	0.97	0.88
43	21.0	1.00	1.00	1.00	1.03	0.97	0.89

To quantitatively identify the differences in the power curves, the relative error of PC_{NL} was calculated with a bin interval of 0.5 m/s assuming that the power curves according to IEC standards are a reference using the Eq. III-15:

$$Relative\ error\ [\%] = \frac{PC_{IEC} - PC_{NL}}{PC_{IEC}} \times 100 \qquad (III\text{-}15)$$

where PC_{IEC} is the power output of PC_{Cup} with IEC 61400-12-1 1st edition or PC_{REWS} with IEC 61400-12-1 2nd edition.

The results are shown in Fig. III-34. Overall, both the relative errors decreased as the wind speed before the rated wind speed increased and were close to 0 % after the rated wind speed. Before the rated wind speed, the relative errors with PC_{Cup} varied from 0.69 % to 20.11 % with a mean value of 6.11 %, and the relative errors with PC_{REWS} were within the range from 0.54 % to 20.09 % with a mean value of 7.10 %. Although this result looked quite large, it is not actually large because the error between cup anemometer measurements and LiDAR wind speed can have by 4 to 6 % [96]. The total mean relative errors of PC_{Cup} and PC_{REWS} were 3.01 % and 3.51 %, respectively.
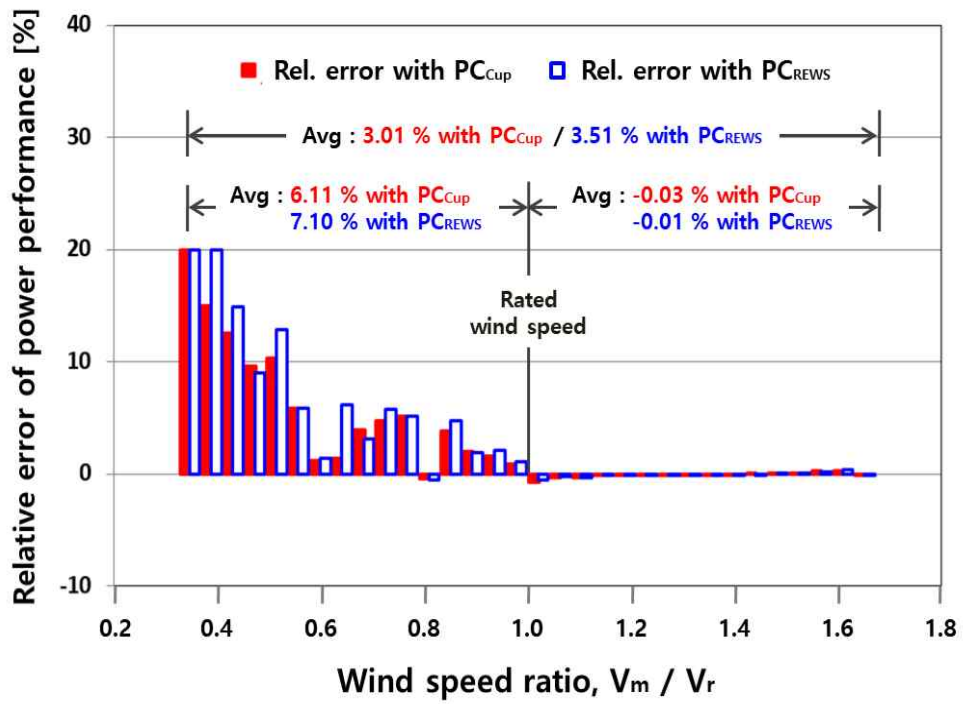
Fig. III-34 Relative errors of PC_{NL} with PC_{Cup} and PC_{REWS}

3) Comparison of AEPs

According to IEC 61400-12-2, a Rayleigh wind speed distribution with annual mean wind speeds of 4 m/s to 11 m/s presented in Fig. III-35 is assumed to estimate the AEPs from PC_{NL} (AEP_{NL}), PC_{Cup} (AEP_{Cup}) and PC_{REWS} (AEP_{REWS}). The AEPs can be calculated using Eq. III-16:

$$AEP = N_h \sum_{i=1}^{N} [F(V_i) - F(V_{i-1})] \left(\frac{P_{i-1} + P_i}{2} \right) \tag{III-16}$$

where N_h is the number of hours in a year and N is the number of bins. $F(V_i)$ and $F(V_{i-1})$ are the Rayleigh cumulative probability distribution functions for wind speeds V_i and V_{i-1} in bins i and i-1, respectively. P_i and P_{i-1} represent the average power output in bins i and i-1, respectively.
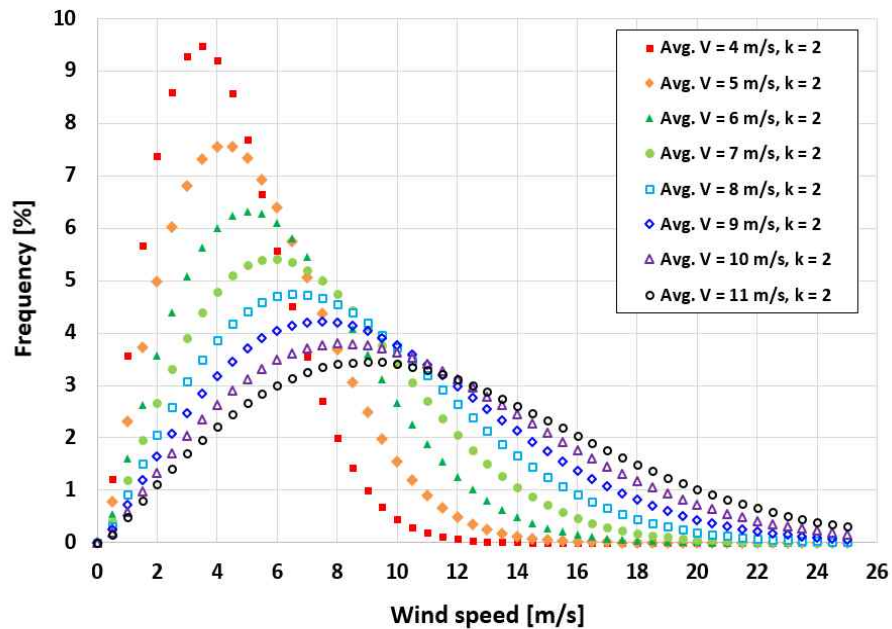
Fig. III-35 Rayleigh wind distribution corresponding mean wind speed of 4 to 11 m/s

Table III-9 lists the ratio of the AEPs estimated from each power curve. In the table, AEP-extrapolated means the AEP calculated by extrapolating power from the last bin to the cut-out wind speed of 25 m/s. It was found that the ratio of AEPs increased as the wind speed increased, and the ratio of AEPs shows a high relationship of more than 91 % except for the case with an annual mean wind speed of 4 m/s. In particular, the ratio of AEPs was more than 96 % at an annual mean wind speed of 7 m/s at the test site.

Table III-9 Ratio of AEPs derived from measured power curves of the test wind turbine at the Haengwon wind farm

Annual mean wind speed [m/s]	AEP-measured		AEP-extrapolated	
	AEP_{NL} / AEP_{Cup}	AEP_{NL} / AEP_{REWS}	AEP_{NL} / AEP_{Cup}	AEP_{NL} / AEP_{REWS}
4	0.87	0.86	0.86	0.85
5	0.95	0.92	0.92	0.91
6	0.96	0.94	0.95	0.94
7	0.97	0.96	0.96	0.96
8	0.99	0.97	0.97	0.97
9	1.01	0.97	0.98	0.97
10	1.02	0.98	0.98	0.98
11	1.04	0.98	0.98	0.98

6. Discussion and conclusions

To clarify the difference in the wind turbine power curves drawn using the cup anemometer wind data, REWS, and nacelle LiDAR measurements, a measurement campaign using ground and nacelle LiDARs with a met mast was conducted. The REWS and the nacelle LiDAR wind speed were compared with the cup anemometer wind speeds through linear regression analysis, using the cup anemometer wind speeds as a reference. The power output scatter plots by each measurement were compared with one another. Subsequently, the power curves were drawn from each measurement and the relative error was analyzed to quantitatively identify their difference. The results can be summarized as follows:

1) The correlation among the cup anemometer, ground LiDAR, and nacelle LiDAR wind speeds was high; the linear regression analysis showed slopes of 0.982 and 0.984 with corresponding coefficients of determination of 0.964 and 0.970 for the ground LiDAR and the nacelle LiDAR, respectively.

2) Although the correlation between the cup anemometer wind speed and REWS was high with a slope of 0.995 and a coefficient of determination of 0.999, the two types of wind speeds were slightly different from each other.

3) The power output by the nacelle LiDAR measurements exhibited a smaller scatter than those of the cup anemometer wind speed and REWS owing to the difference in the measuring method.

4) The power curve and the power coefficient of the nacelle LiDAR before the rated wind speed were clearly lower than those of the cup anemometer wind speed and REWS, while those following the rated wind speed were close to one another.

5) Overall, the relative error for the power curves before the rated wind speed was high, while that after the rated was close to 0%. The total mean relative errors with PC_{Cup} and PC_{REWS} were 3.01 % and 3.51 %, respectively.

6) AEP_{NL} was very similar to AEP_{Cup} and AEP_{REWS} by means of the IEC 61400-12-1 1st and 2nd editions. At an annual mean wind speed of 7 m/s at the test site, the ratio of AEPs was more than 96 %.

IV. Application of the NTF from the nacelle LiDAR measurements for power performance measurement of multiple wind turbines [2]

In Chapter III, the applicability of the nacelle LiDAR was confirmed by a power performance measurement for a test wind turbine. Although economic problems can be solved by the use of the nacelle LiDAR for power performance testing for a wind turbine, a considerable amount of time will be needed for multiple wind turbines on a wind farm because testing power performance for a wind turbine takes more than six months.

The nacelle wind speed measured by nacelle anemometer on the nacelle of a wind turbine has not been used for wind turbine power performance tests, because it is disturbed by wake effects due to the rotation of rotor blades. According to IEC 61400-12-2, the free-stream wind speed upwind can be predicted by correcting the nacelle wind speed using the NTF, which is the correlation between wind speeds measured using a cup anemometer on a met mast and a nacelle anemometer on a wind turbine. Using the NTF derived from a representative wind turbine, the power performance of other wind turbines can be evaluated if some requirements are satisfied.

If it is possible to apply the NTF derived from nacelle LiDAR measurements without a met mast to power performance testing, power curves of other wind turbines can be drawn, which will be done at a comparatively low cost and in a short duration. In particular, it will be helpful for offshore wind turbine testing.

---

2) This chapter was written by citing from the author's papers published in Energies (2019) and Journal of Wind Energy (2018) [97, 98].

This Chapter aims to identify the applicability of NTF_{NL} for power performance measurement of multiple wind turbines without a met mast, and to further estimate the uncertainties of the power curves and the AEPs.

The investigation was experimentally conducted at the Dongbok wind farm on Jeju Island, South Korea. A 4-beam nacelle LiDAR was mounted on the nacelle of a 2 MW wind turbine to measure wind conditions in front of the turbine rotor, and an 80 m high met mast was installed near another wind turbine to measure the free-stream wind speed.

First, the characteristics of the 4-beam nacelle LiDAR wind data were analyzed under the same conditions as the characteristics analysis of the 2-beam nacelle LiDAR wind data in Section 2.2 of Chapter III. NTF_{NL} was derived from the correlation between the wind data from a nacelle LiDAR and a nacelle anemometer on a wind turbine. For the same types of wind turbines as the test wind turbine, $PCs_{NTF,NL}$ were compared with PC_{Cup}, PC_{NL}, and the power curve from the wind speed corrected using NTF_{Cup} in IEC 61400-12-2 ($PC_{NTF,Cup}$). The combined standard uncertainties of the power curves (u_{PC}) were evaluated, and the uncertainties of each component involved in their construction were estimated in detail. Finally, the uncertainties of AEP (u_{AEP}) were evaluated assuming that the wind follows a Rayleigh wind speed distribution.

1. Test setup

1) Test site II

(1) Dongbok wind farm

The study on identifying the applicability of the NTF$_{NL}$ to test the power performance of multiple wind turbines was conducted at the Dongbok wind farm of Jeju Island, South Korea. The wind farm is situated on the north-eastern part of the island, as shown in Fig. IV-1. Fifteen 2 MW wind turbines have been operating and wind turbines no. 1 and 15 were tested for this work. The 4-beam nacelle LiDAR was installed on the nacelle of wind turbine no. 1, and a ground LiDAR was installed at 2.5 times the rotor diameter from the turbine. In addition, a met mast was positioned at 2.5 times the rotor diameter from wind turbine no. 15.

The 10-minute average wind conditions for one year from 1 January 2017 to 31 December 2017 were measured by the nacelle and ground LiDARs, the met mast, and the nacelle anemometers on the wind turbines, and these were analyzed in this work.
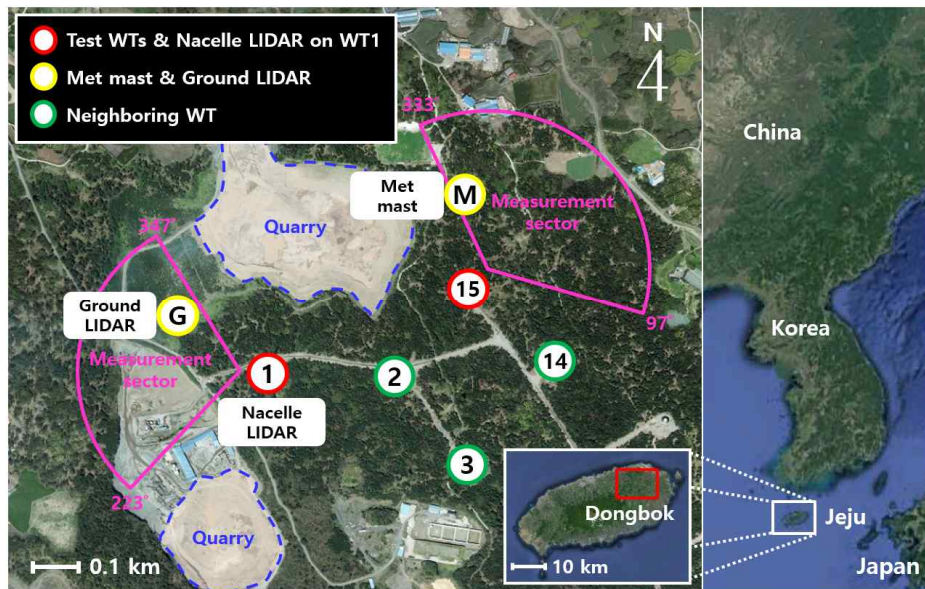
Fig. IV-1 Location of Jeju Island including the layout of the wind turbines and instruments at the Dongbok wind farm

(2) Measurement sector

There are two quarries to the south and north of wind turbine no. 1. To exclude the wind data disturbed by the wake effects due to blade rotation of neighboring wind turbines and the two quarries, the measurement sectors were calculated using Eqs. III-1 and III-2. As shown in Fig. IV-1, the determined measurement sector of wind turbine no. 1 was from 223° to 347° for NTF_{NL} derivation and application, and that of wind turbine no. 15 was from 333° to 97° for NTF_{NL} application to another wind turbine.

(3) Terrain evaluation

According to the procedure explained in Section 1.1.3 of Chapter III, the terrain evaluation was conducted as shown in Fig. IV-2. Table IV-1 lists the results. Although the topographical conditions were slightly complex as presented in Figs. IV-3 to IV-7, the values obtained for the maximum slope and terrain variation under each condition were met, which means that no site calibration was required.
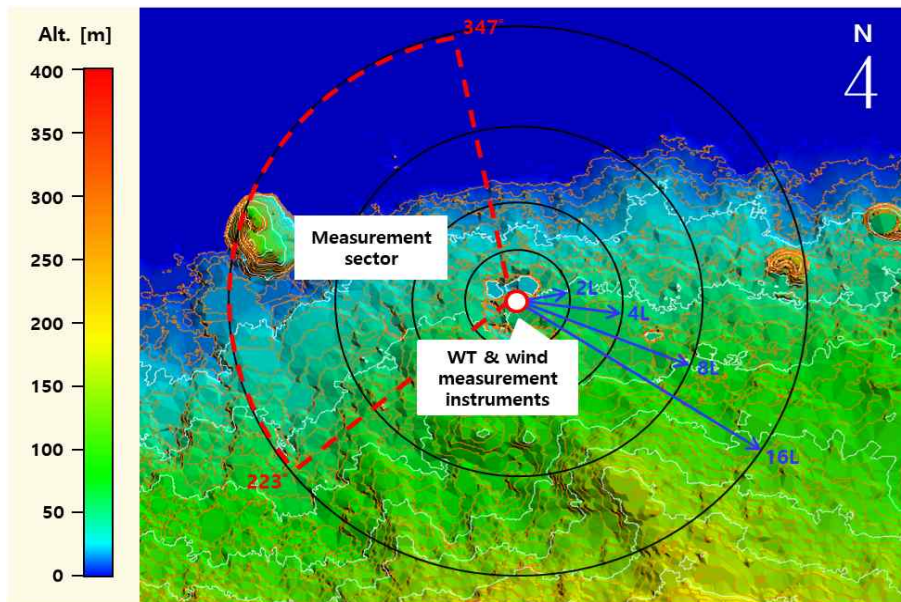
Fig. IV-2 Measurement sector and region for terrain evaluation of wind turbine no. 1 at the Dongbok wind farm

Table IV-1 Terrain evaluation results for the Dongbok wind farm

Distance	Sector	Maximum slope [%]	Maximum terrain variation [m]
<2L	360°	2.4 < 3	12.3 < 1/3(H-0.5D)
≥2L and <4L	Measurement sector	1.5 < 5	15.5 < 2/3(H-0.5D)
≥2L and <4L	Outside measurement sector	3.3 < 10	Not applicable
≥4L and <8L	Measurement sector	1.3 < 10	25.9 < (H-0.5D)
≥8L and <16L	Measurement sector	1.2 < 10	Not applicable

∗ H: 80 m, D: 87 m
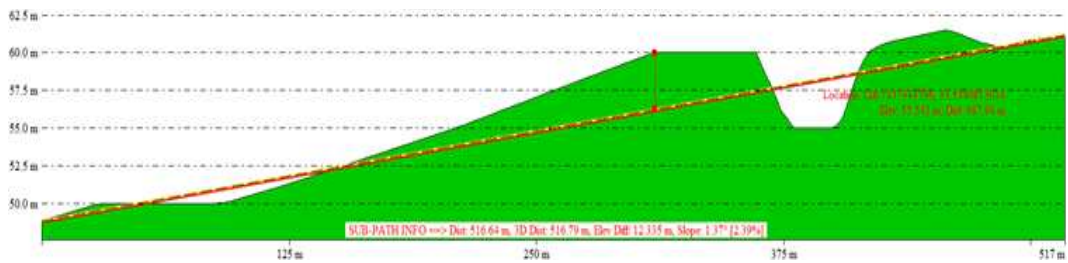
Fig. IV-3 Terrain evaluation within 2L of wind turbine no. 1 at the Dongbok wind farm
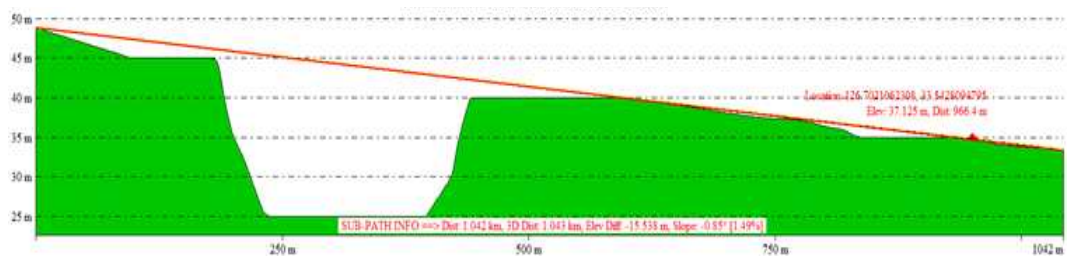
Fig. IV-4 Terrain evaluation of the measurement sector within 4L of wind turbine no. 1 at the Dongbok wind farm
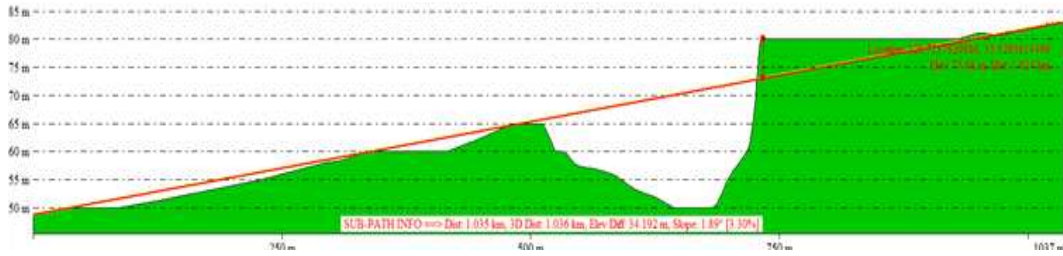
Fig. IV-5 Terrain evaluation of the outside measurement sector within 4L of wind turbine no. 1 at the Dongbok wind farm
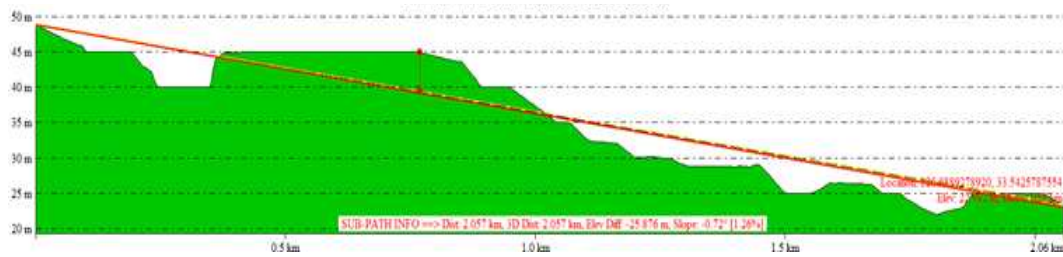
Fig. IV-6 Terrain evaluation of the measurement sector within 8L of wind turbine no. 1 at the Dongbok wind farm
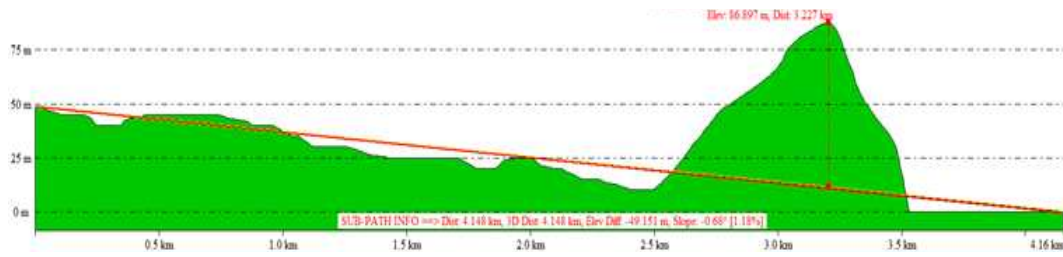
Fig. IV-7 Terrain evaluation of the measurement sector within 16L of wind turbine no. 1 at the Dongbok wind farm

2) Test wind turbine

(1) Wind turbine

Fig. IV-8 shows the view of test wind turbines no. 1 and 15 at the Dongbok wind farm, and Table IV-2 lists the specifications of two test wind turbines for this work. They are the same 2 MW wind turbines, HJWT 2000. Their hub height and rotor diameter are 80 m and 87 m, respectively.

Fig. IV-8 View of the test wind turbines at the Dongbok wind farm

Table IV-2 Specification of wind turbines no. 1 and 15 at the Dongbok wind farm

Items	Description
Model	HJWT 2000
Rated power	2000 kW
Hub height	80 m
Rotor diameter	87 m
Swept area	5944.68 m^2
Rated RPM	17.3 rpm
Blade control	Pitch control
Cut-in / rated / cut-out wind speed	3.5 / 12.5 / 25 m/s

Table IV-3 presents the specifications of electric power measurement instruments installed in the wind turbine tower bases. The CT and the PT of class 0.5 were used in compliance with IEC 61400-12-2.

Table IV-3 Specifications of electric power measurement instruments in wind turbines no. 1 and 15 at the Dongbok wind farm

Items	Current transformer	Power transducer
Model	BC 1009	P 530
Measurement range	3000 A	100-690 V / 1-6 A
Resolution	Ratio = 3000 : 5	4-20 mA output
Accuracy	Class 0.5	Class 0.5

(2) Nacelle wind sensors

Table IV-4 lists specifications of nacelle wind sensors and the SCADA system. The nacelle anemometers and the nacelle wind vanes were installed on the top of the nacelle, and the wind data were collected by the SCADA system, whose model is Gateway, developed by Mita-teknik.

Table IV-4 Specifications of nacelle wind sensors and SCADA system on wind turbines no. 1 and 15 at the Dongbok wind farm

Items	Nacelle anemometer	Nacelle wind vane
Model	Mita-Teknik WS sensor 690360	Mita-Teknik WD sensor 0-20 mA
Measurement range	0.5 - 50 m/s	0 - 360°
Accuracy	0.2 m/s	± 0.5°
Data acquisition system	Gateway SCADA system	

To avoid the flow distortions caused by the rotor blades and the nacelle itself, the nacelle wind sensors should be positioned in accordance with the criteria provided in Annex A of IEC 61400-12-2. Fig. IV-9 shows the criteria for mounting the nacelle wind sensor and the actual image of the nacelle anemometers and the nacelle wind vanes with a nacelle LiDAR on the nacelle of wind turbine no. 1. The nacelle wind sensors should be mounted above the boundary layer, indicated by the 10° line from the cylindrical blade root to the profiled blade, and at least 1.5 times the blade root diameter behind the blade root center. Additionally, they should not be situated within 1 m of the downwind end of the nacelle. According to the criteria, the mounting status of the nacelle anemometers and wind vanes of the wind turbines tested was carefully checked, and it was confirmed that those sensors had been properly mounted.
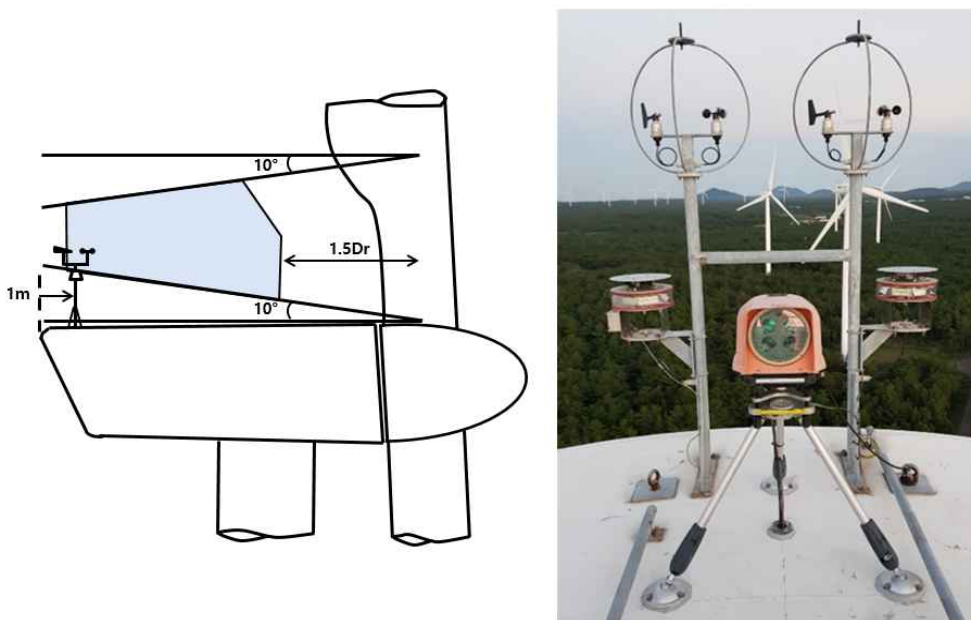
Fig. IV-9 Criteria and actual image for mounting wind sensors with a 4-beam nacelle LiDAR

3) Measurement instruments

(1) 4-beam nacelle LiDAR

For identifying the applicability of NTF_{NL} to test the power performance of multiple wind turbines, the 4-beam nacelle LiDAR, which is the Wind Iris 2nd edition developed by Avent, was used, as shown in Fig. IV-9. Table IV-5 presents the specification of the 4-beam nacelle LiDAR. It emits four laser beams as a stream of pulses with four lines of sight, separated by a horizontal angle of 30° and a vertical angle of 10°. It can measure wind conditions at up to 10 points between 80 m and 400 m horizontally from its optical head. The horizontal wind speed is calculated by taking account of wind shear from four beams. For this work, the nacelle LiDAR wind data at eight points from 80 m to 360 m with 40 m interval were used for characteristics analysis of 4-beam nacelle LiDAR measurements, and the nacelle LiDAR measurements at 2.5 times the rotor diameter from wind turbine no. 1 were analyzed to test the power performance of multiple wind turbines. The pre-tilt value of the nacelle LiDAR calculated using Eq. III-3 was - 1.35°.

Table IV-5 Specifications of the 4-beam nacelle LiDAR

Items	Description
Model	Wind Iris 2nd edition
Measurement range	80 to 400 m
Data sampling rate	1 to 2.5 Hz
No. of measurements	10
Laser source	Fiber pulsed laser 1.54 μm
Speed accuracy	0.1 m/s
Speed range	-10 to 40 m/s
Direction accuracy	± 0.5°

Using the dedicated software provided by the manufacturer, the wind data such as wind speed, wind direction, and CNR signals were monitored in real time during the measurement period,

This nacelle LiDAR was calibrated for the tilt inclinometer through a collaborative research project with KTL, according to the procedure in DTU Wind Energy E-0020 [74, 75]. The detailed calibration procedure and results are described with the uncertainty estimation in Section 5.1.2 of this Chapter.

(2) Ground LiDAR

The ground LiDAR used for this work was Windcube v2 the same model as the ground LiDAR described in Section 1.3.2 of Chapter III, as presented in Fig. IV-10. This ground LiDAR contains flow complexity recognition (FCR) module, which is an algorithm that associates the 10-minute average wind data with fluid mechanics equations in order to determine the wind speed and wind direction for a given terrain topography. It embeds a 3D wind field model for complex terrain [99-104].

Fig. IV-10 Ground LiDAR installed at the Dongbok wind farm

(3) Met mast

Table IV-6 lists the specifications of the sensors on the met mast that were installed north of wind turbine no. 15. An 80 m high lattice type met mast was installed to test the power performance of wind turbines in accordance with IEC 61400-12-1. The wind speed at the hub height was measured by a Thies first class cup anemometer. Moreover, air temperature, humidity, and atmospheric pressure were measured by a thermometer, hygrometer, and barometer, respectively. The meteorological data were used to derive the normalized wind speed from the specific air density at the test site.

Table IV-6 Specification of the met mast installed at the Dongbok wind farm

Items	Models	Accuracy	Height
Anemometer	Thies first class advanced	0.2 m/s	80 m
Wind vane	Thies first class advanced	± 0.5°	78.5 m
Temperature	Rotronic hygromer	0.3 K	78.5 m
Humidity	PT 100 class A	± 2 %	78.5 m
Pressure	P-GE 6/11	± 0.1 %	78.5 m

2. Characteristics analysis of the 4-beam nacelle LiDAR measurements

1) Validity check of the reference data

In this work, the ground LiDAR wind data were used as the reference data to verify the reliability of the nacelle LiDAR measurements. For that, it is necessary to firstly check the validity of the ground LiDAR wind data because only met mast wind data can be used as a reference according to IEC standards.

Fig. IV-11 presents the result of linear regression analysis between wind speeds measured by the ground LiDAR and the cup anemometer of a met mast. The ground LiDAR data filtering was then conducted according to the suggestion provided by Kim et al. [52]. Their correlation was very high: The slope and coefficient of determination were 0.954 and 0.940, respectively,
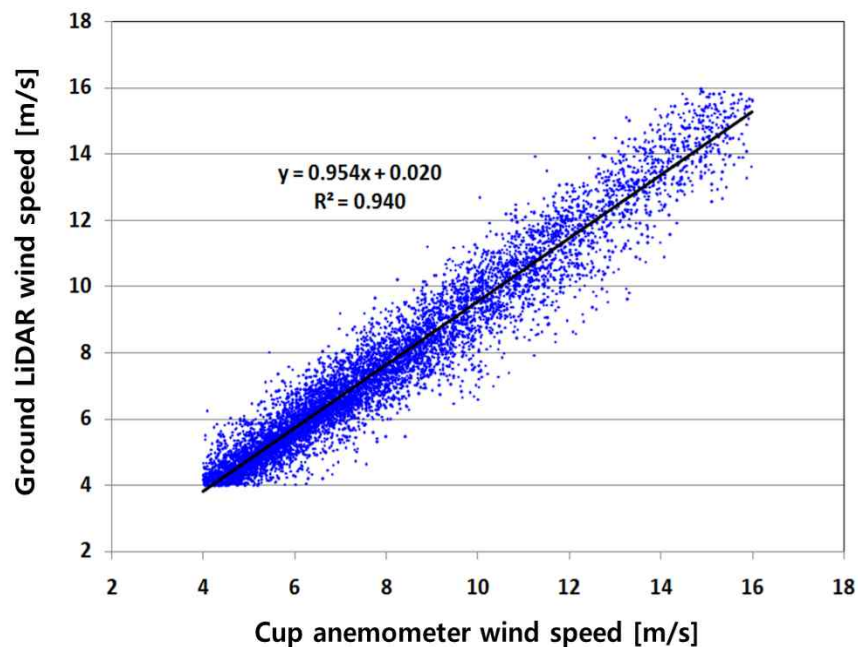
Fig. IV-11 Linear regression analysis between wind speeds measured by a ground LiDAR and a cup anemometer at the Dongbok wind farm

2) Characteristics analysis of 4-beam nacelle LiDAR measurements

To compare with the results of the characteristics analysis of 2-beam nacelle LiDAR measurements, the results of 4-beam nacelle LiDAR measurements were analyzed under the same conditions in Section 2 of Chapter III. The weather conditions, mechanical movement, and nacelle LiDAR availability were determined.

Fig. IV-12 presents the max, min, mean, and standard deviation of CNR signals measured by the 4-beam nacelle LiDAR for the measurement period. Although the mean value of the CNR signals was generally lower than those of the 2-beam nacelle LiDAR, which varied from ‑18 dB to ‑21 dB, it was confirmed that CNR signals were within a normal range, i.e., they were over ‑23 dB.
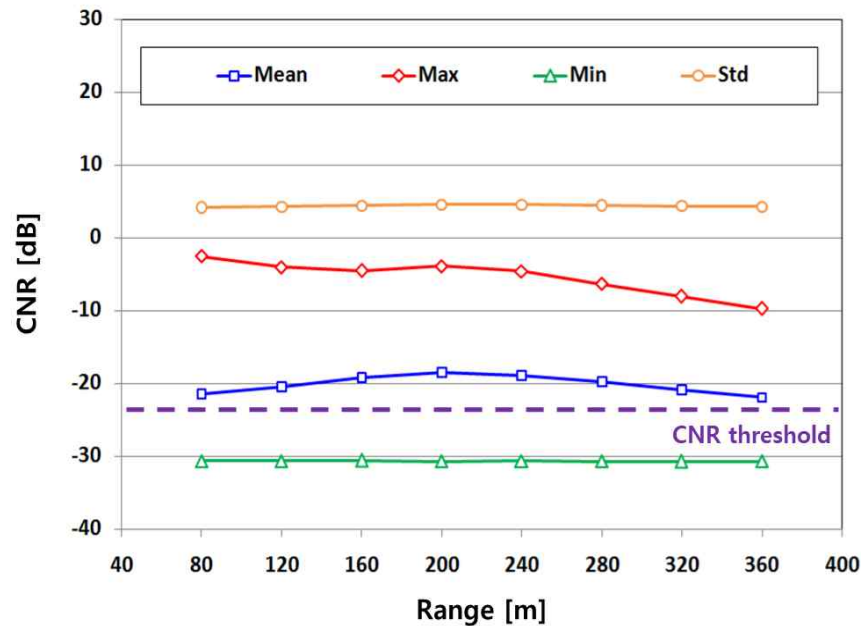
Fig. IV-12 Max, min, mean, and standard deviation of CNR signals of a 4-beam nacelle LiDAR

(1) CNR variation with weather conditions

Figs. IV-13 to IV-15 present CNR variations with weather conditions analyzed using air temperature, humidity and pressure data measured from the met mast. The CNRs were generally the highest at the distance between 160 m and 240 m, and their value reduces as distance increases beyond 240 m. For the temperature condition, the CNRs were the highest between 0 ℃ and 10 ℃ and the lowest between 21 ℃ and 30 ℃. This effect is opposite that of the CNR variation with temperature of the 2-beam nacelle LiDAR measurements. For the humidity condition, although the CNRs did not exhibit a trend, they were similar within ± 5 dB. For the pressure condition, they exhibited a sequential trend with pressure variation. However, the CNRs were in the normal range of more than ‐23 dB in all conditions. In conclusion, it was confirmed that the weather conditions have no effect on nacelle LiDAR measurement.

When comparing with the results of the characteristics analysis of the 2-beam nacelle LiDAR measurements, these results were considerably different. For a more accurate analysis, further studies are required, such as an analysis of CNR variation with aerosol distribution, wind speed variation, etc.
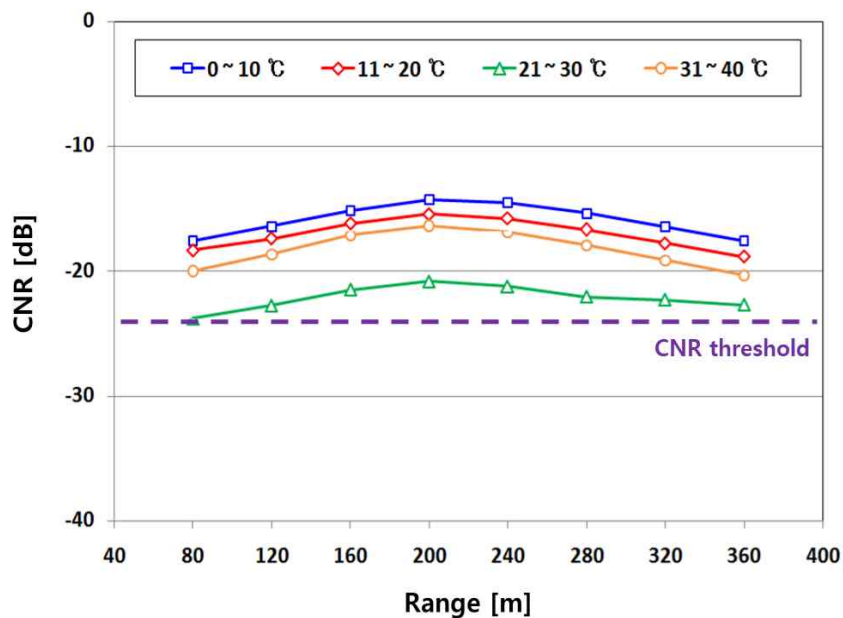
Fig. IV-13 Variation in the CNR of 4-beam nacelle LiDAR with temperature
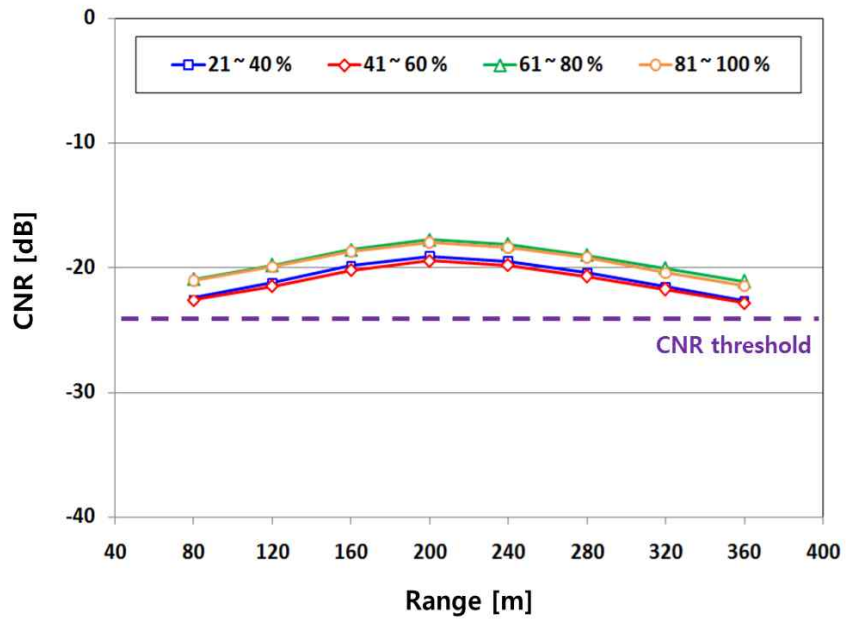
Fig. IV-14 Variation in the CNR of 4-beam nacelle LiDAR with humidity
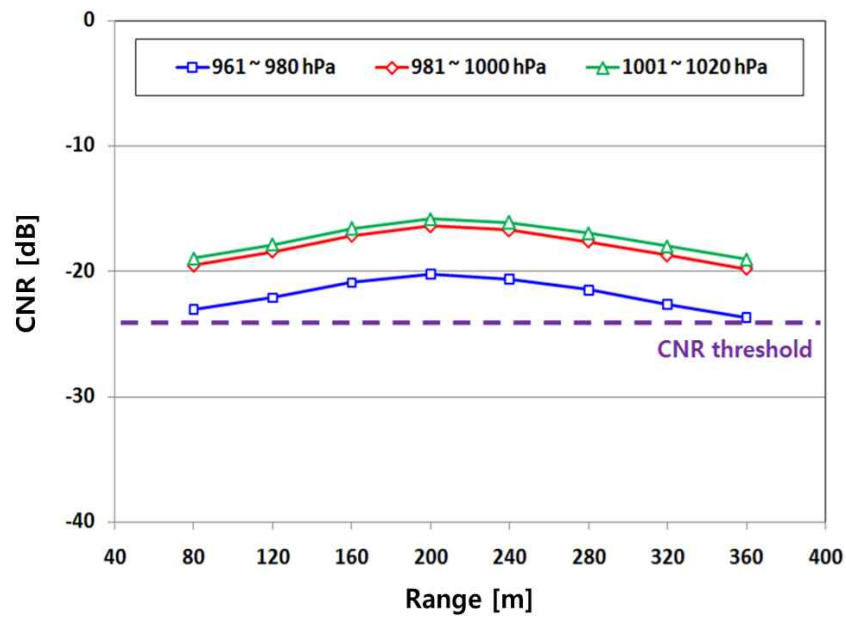
Fig. IV-15 Variation in the CNR of 4-beam nacelle LiDAR with pressure

Fig. IV-16 shows the CNR variation with the amount of precipitation. The CNR variation was investigated when daily precipitation was more than 10 mm for about five months of total measurement period. Although observation of CNR signals under the CNR threshold for the analysis period was low, it had nothing to do with precipitation. Although precipitation varied from 13.4 mm to 39.8 mm, it was confirmed that the CNR signals were normal, which means that the precipitation did not affect the nacelle LIDAR measurement.
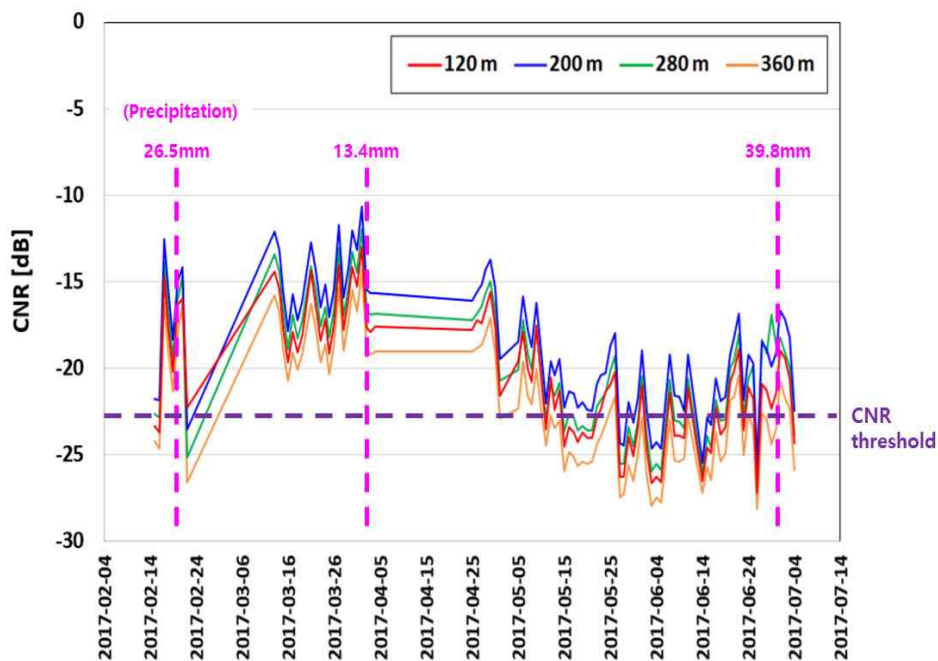
Fig. IV-16 Variation in the CNR of 4-beam nacelle LiDAR with amount of precipitation

(2) CNR variation with mechanical movement

Fig. IV-17 shows the CNR variation with rotor RPM. Although about 8.9 % of the CNR signals were under the threshold ‑23 dB, they were not a true reflection of the data because the data availability was less than 80 %, and they should be removed during data filtering. Thus, it was confirmed that rotation of the rotor blades did not affect normal measurement of a the nacelle LiDAR.

Fig. IV-18 presents the standard deviation of the CNR with rotor RPM. In this case, the trend of the standard deviation of the CNR with rotor RPM variation could not be confirmed owing to omission of rotor RPM data with values less than 10 rpm, which may be caused by the wind turbine control strategy for high efficiency.

Fig. IV-19 displays the 4-beam nacelle LiDAR measurement error with tilt angle variation. The tilt angle was changed in the range between ‑1.4 ° and ‑0.6 ° from the initial tilt value of ‑1.35 °; then, the 4-beam nacelle LiDAR measurement error was close to 0. Thus, it was confirmed once again that the tilt variation had no effect on the measurement accuracy of the nacelle LiDAR.
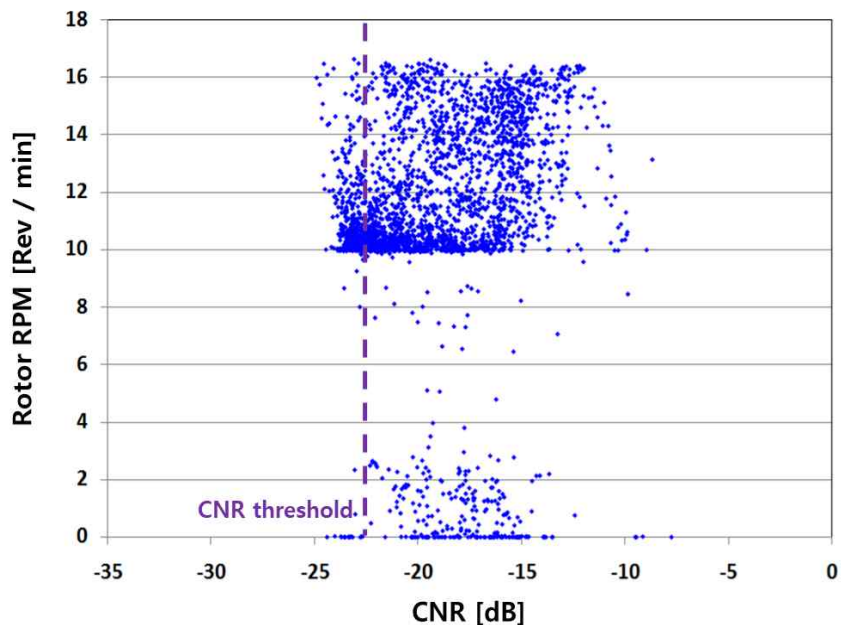
Fig. IV-17 Variation in the CNR of 4-beam nacelle LiDAR with rotation of rotor blades
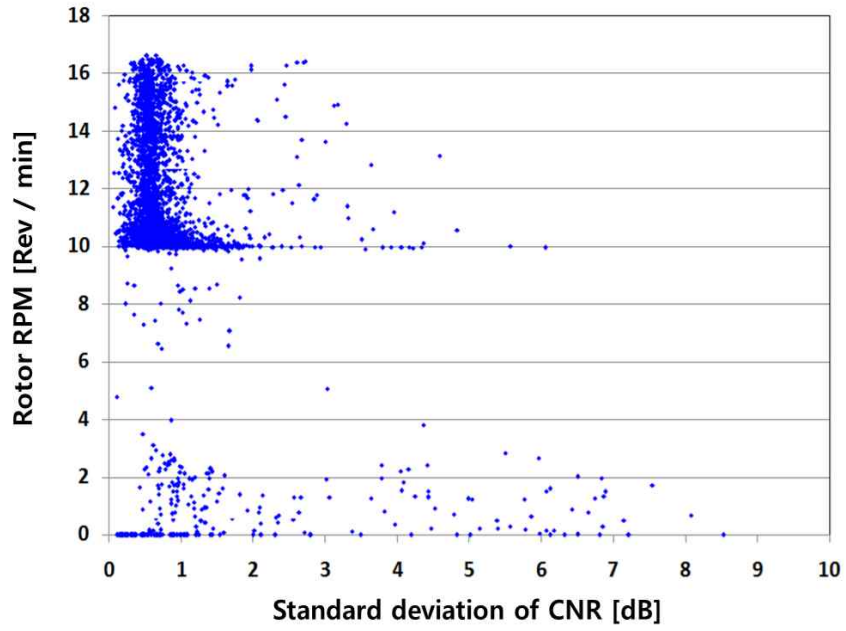
Fig. IV-18 Standard deviation of the CNR of 4-beam nacelle LiDAR with rotation of rotor blades
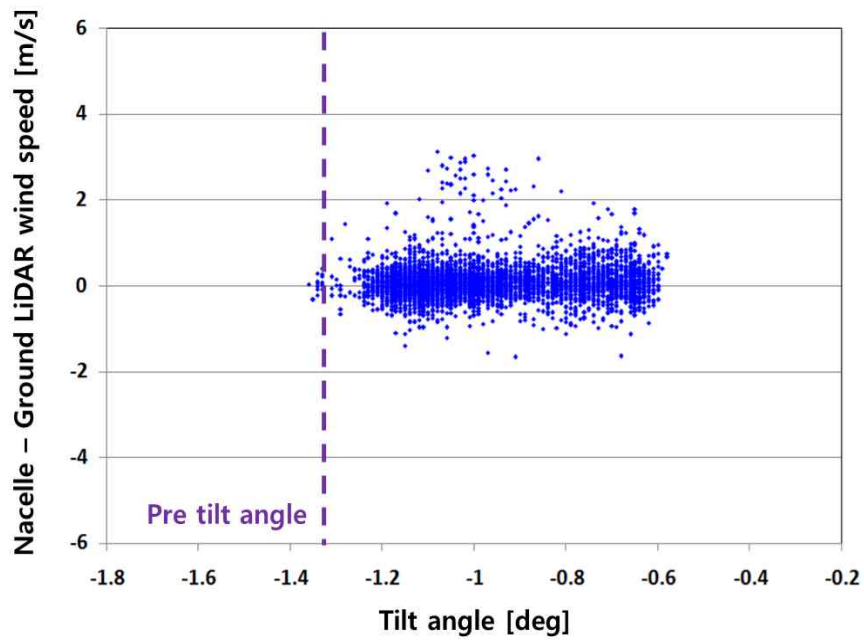
Fig. IV-19 4-beam nacelle LiDAR measurement error with tilt angle variation

(3) Data accuracy with data availability

Fig. IV-20 displays the 4-beam nacelle LiDAR measurement error with data availability. Here, the nacelle LiDAR measurement error is the difference between wind speeds measured from the nacelle and ground LiDARs. The measurement error was close to 0 when the data availability was more than 80 %. Most of the data points were included when the data availability was more than 80 %.
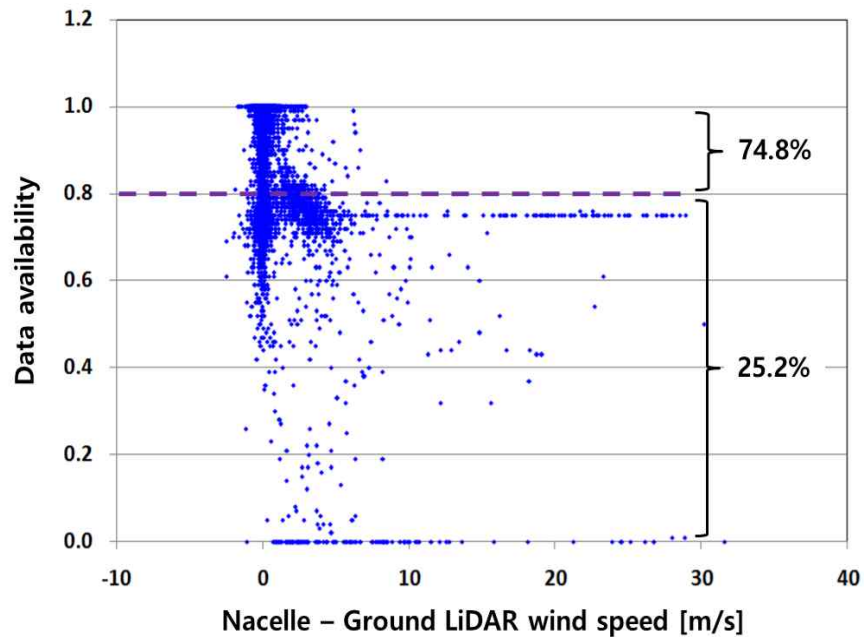
Fig. IV-20 4-beam nacelle LiDAR measurement error with data availability

3. Data rejection and reliability verification

According to the standard for LiDAR data filtering in Section 3 of Chapter III, the nacelle LiDAR measurements and the concurrent data of the other sources were discarded.

Fig. IV-21 shows the result of linear regression analysis between selected wind speeds from the nacelle and ground LiDARs after data filtering. The slope and coefficient of determination were 1.010 and 0.984, respectively. Thus, it was confirmed that the data were reliable and properly filtered.

Fig. IV-22 shows the scatter plot and the mean value with bin interval of 1 m/s of the nacelle and ground LiDAR wind speeds. The nacelle LiDAR measurement errors were close to 0 in all regions, and the mean value varied in the range from 0.05 m/s to 0.08 m/s with a median of 0.07 m/s. In addition, the standard deviations of the nacelle LiDAR measurement error varied from 0.20 to 0.34 m/s with a median of 0.33 m/s.
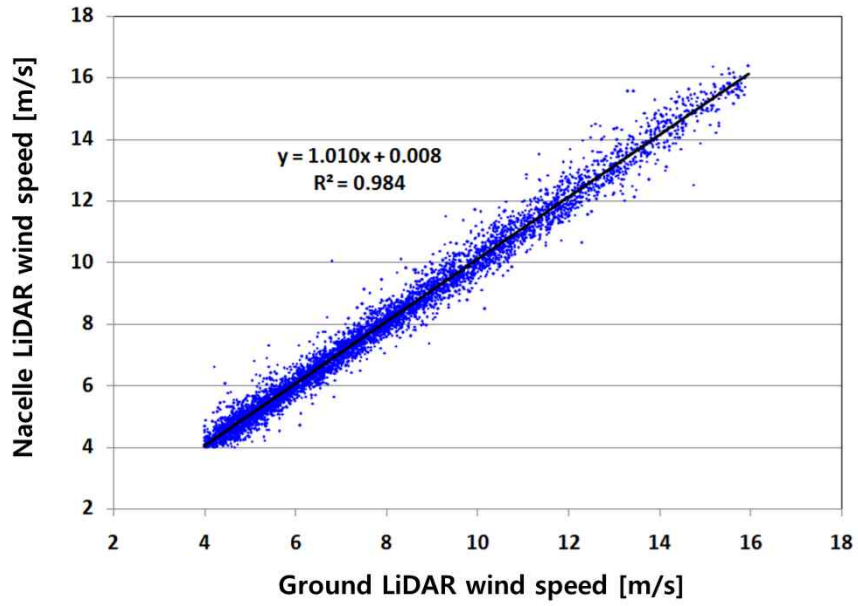
Fig. IV-21 Linear regression analysis between wind speeds measured by 4-beam nacelle and ground LiDARs
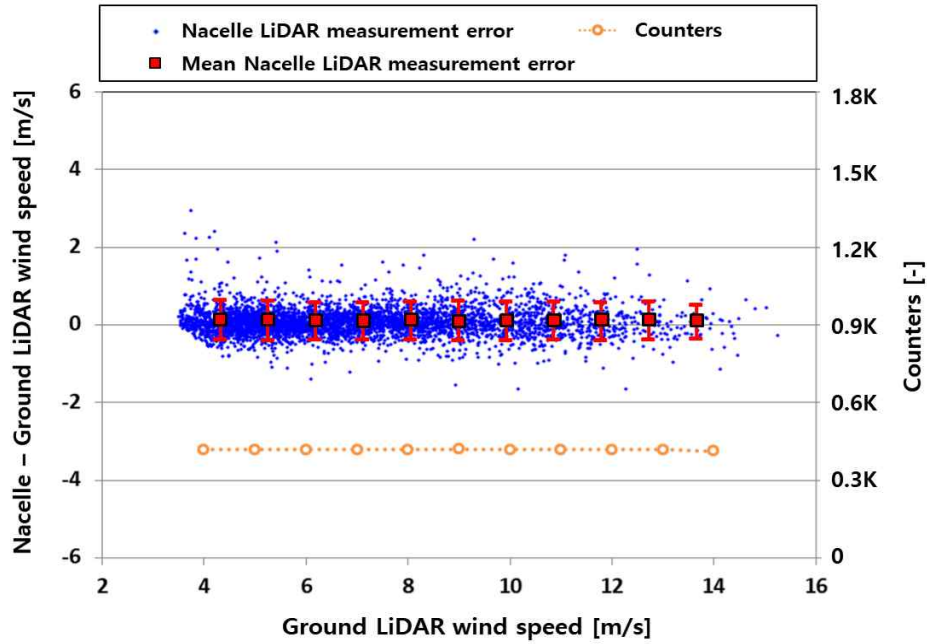
Fig. IV-22 4-beam nacelle LiDAR measurement error and number of data points

4. Wind turbine power performance measurement by applying the NTF from the nacelle LiDAR measurements

1) Derivation of NTF_{NL}

The NTF can be defined as the correlation of free-stream wind speed (V_{free}) and nacelle wind speed ($V_{nacelle}$). Using the table method given in IEC 61400-12-2, the $V_{nacelle}$ can be corrected to V_{free}.

The selected wind data after data filtering were binned in 0.5 m/s intervals; then, linear interpolation was conducted between the bins using the following equation to obtain V_{free}:

$$V_{free} = \frac{V_{free,i+1} - V_{free,i}}{V_{nacelle,i+1} - V_{nacelle,i}} \times (V_{nacelle} - V_{nacelle,i}) + V_{free,i} \qquad (IV-1)$$

where $V_{free,i}$ and $V_{free,i+1}$ are the bin-averaged free-stream wind speeds in bins i and i+1, respectively. $V_{nacelle,i}$ and $V_{nacelle,i+1}$ are the bin-averaged wind speeds measured by the nacelle anemometer in bins i and i+1, respectively. $V_{nacelle}$ is the wind speed measured by the nacelle anemometer.

NTF_{NL} and NTF_{Cup} were computed using the nacelle wind speeds of the test wind turbines with free-stream wind speeds measured by the nacelle LiDAR and the cup anemometer of the met mast, respectively.

Figs. IV-23, IV-24 and Tables IV-7, IV-8 present the NTFs derived from the nacelle LiDAR measurements and cup anemometer wind speeds using the table method, respectively. The relationships had a slope close to one, which means that the correlation between the free-stream and nacelle anemometer wind speeds was extremely high; consequently, NTF_{NL} and NTF_{Cup} were considered to have been derived properly.
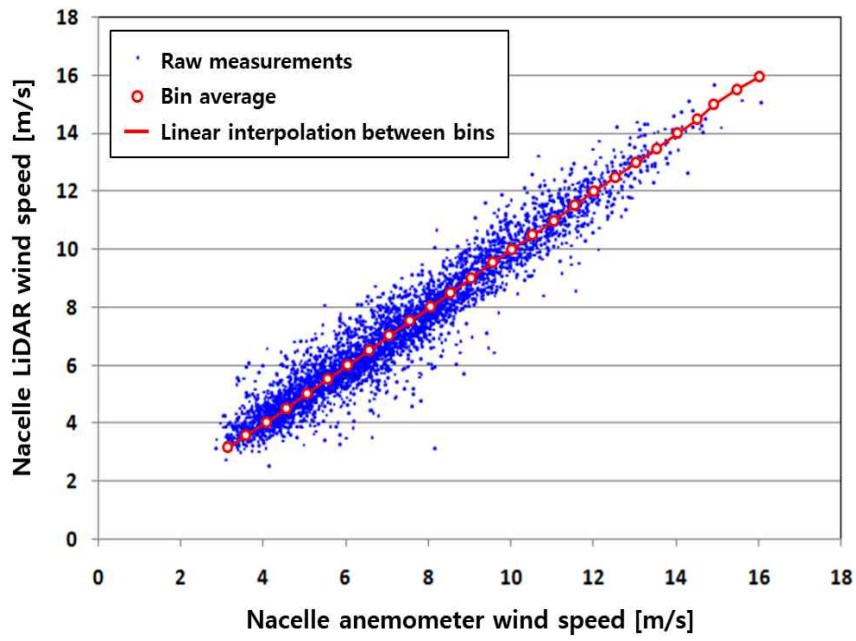
Fig. IV-23 NTF derived from the nacelle LiDAR measurements
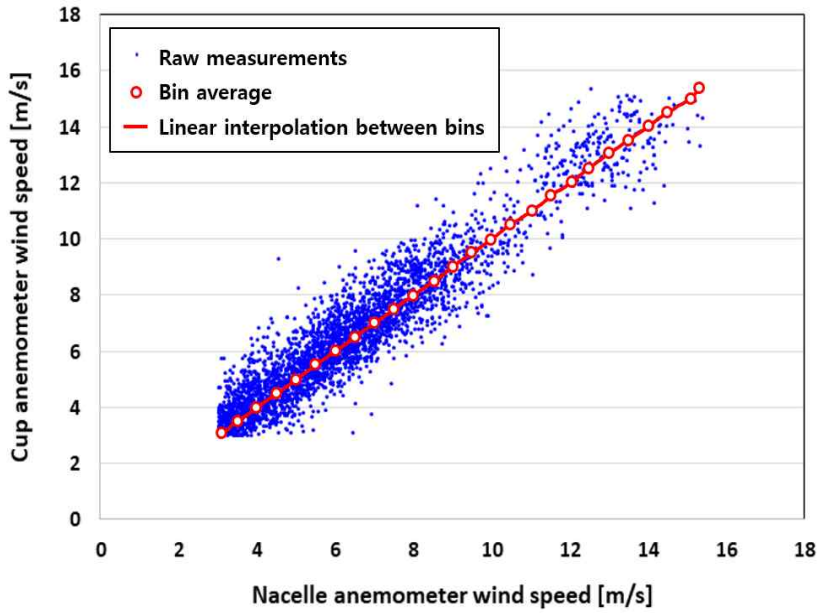
Fig. IV-24 NTF derived from the cup anemometer wind speed

Table IV-7 Transfer function from $V_{nacelle}$ to V_{free} by NTF_{NL}

$V_{nacelle}$	V_{free}	$V_{nacelle}$	V_{free}	$V_{nacelle}$	V_{free}
3.1	3.2	7.5	7.5	11.9	11.9
3.2	3.3	7.6	7.6	12.0	12.0
3.3	3.4	7.7	7.7	12.1	12.1
3.4	3.4	7.8	7.8	12.2	12.2
3.5	3.5	7.9	7.9	12.3	12.3
3.6	3.6	8.0	8.0	12.4	12.4
3.7	3.7	8.1	8.1	12.5	12.5
3.8	3.8	8.2	8.2	12.6	12.6
3.9	3.9	8.3	8.3	12.7	12.7
4.0	4.0	8.4	8.4	12.8	12.8
4.1	4.0	8.5	8.5	12.9	12.9
4.2	4.2	8.6	8.6	13.0	13.0
4.3	4.3	8.7	8.7	13.1	13.1
4.4	4.4	8.8	8.8	13.2	13.2
4.5	4.5	8.9	8.9	13.3	13.3
4.6	4.5	9.0	9.0	13.4	13.4
4.7	4.7	9.1	9.1	13.5	13.5
4.8	4.8	9.2	9.2	13.6	13.6
4.9	4.9	9.3	9.3	13.7	13.7
5.0	5.1	9.4	9.4	13.8	13.8
5.1	5.1	9.5	9.5	13.9	13.9
5.2	5.2	9.6	9.6	14.0	14.0
5.3	5.3	9.7	9.7	14.1	14.1
5.4	5.4	9.8	9.8	14.2	14.2
5.5	5.5	9.9	9.9	14.3	14.3
5.6	5.6	10.0	10.0	14.4	14.4
5.7	5.7	10.1	10.1	14.5	14.5
5.8	5.8	10.2	10.2	14.6	14.6
5.9	5.9	10.3	10.3	14.7	14.8
6.0	6.0	10.4	10.4	14.8	14.9
6.1	6.0	10.5	10.5	14.9	15.0
6.2	6.2	10.6	10.6	15.0	15.1
6.3	6.3	10.7	10.7	15.1	15.2
6.4	6.4	10.8	10.8	15.2	15.3
6.5	6.5	10.9	10.9	15.3	15.4
6.6	6.5	11.0	11.0	15.4	15.5
6.7	6.7	11.1	11.1	15.5	15.6
6.8	6.8	11.2	11.2	15.6	15.7
6.9	6.9	11.3	11.3	15.7	15.7
7.0	7.0	11.4	11.4	15.8	15.8
7.1	7.1	11.5	11.6	15.9	15.9
7.2	7.2	11.6	11.6	16.0	16.0
7.3	7.3	11.7	11.7	16.1	16.2
7.4	7.4	11.8	11.8	16.2	16.3

Table IV-8 Transfer function from $V_{nacelle}$ to V_{free} by NTF_{Cup}

$V_{nacelle}$	V_{free}	$V_{nacelle}$	V_{free}	$V_{nacelle}$	V_{free}
3.1	3.1	7.5	7.5	11.9	11.9
3.2	3.2	7.6	7.6	12.0	12.0
3.3	3.3	7.7	7.7	12.1	12.1
3.4	3.4	7.8	7.8	12.2	12.2
3.5	3.5	7.9	7.9	12.3	12.3
3.6	3.6	8.0	8.0	12.4	12.4
3.7	3.7	8.1	8.1	12.5	12.5
3.8	3.8	8.2	8.2	12.6	12.6
3.9	3.9	8.3	8.3	12.7	12.7
4.0	4.0	8.4	8.4	12.8	12.8
4.1	4.1	8.5	8.5	12.9	12.9
4.2	4.2	8.6	8.5	13.0	13.1
4.3	4.3	8.7	8.7	13.1	13.1
4.4	4.4	8.8	8.8	13.2	13.2
4.5	4.5	8.9	8.9	13.3	13.3
4.6	4.6	9.0	9.0	13.4	13.4
4.7	4.7	9.1	9.1	13.5	13.5
4.8	4.8	9.2	9.2	13.6	13.6
4.9	4.9	9.3	9.3	13.7	13.7
5.0	5.0	9.4	9.4	13.8	13.8
5.1	5.1	9.5	9.5	13.9	13.9
5.2	5.2	9.6	9.6	14.0	14.0
5.3	5.3	9.7	9.7	14.0	14.0
5.4	5.4	9.8	9.8	14.2	14.2
5.5	5.5	9.9	9.9	14.3	14.3
5.6	5.6	10.0	10.0	14.4	14.4
5.7	5.7	10.1	10.1	14.5	14.5
5.8	5.8	10.2	10.2	14.6	14.6
5.9	5.9	10.3	10.3	14.7	14.7
6.0	6.0	10.4	10.4	14.8	14.7
6.1	6.1	10.5	10.5	14.9	14.8
6.2	6.2	10.6	10.6	15.0	14.9
6.3	6.3	10.7	10.7	15.1	15.0
6.4	6.4	10.8	10.8	15.2	15.1
6.5	6.6	10.9	10.9	15.3	15.3
6.6	6.6	11.0	10.9	15.4	15.4
6.7	6.7	11.1	11.0	15.5	15.5
6.8	6.8	11.2	11.2	15.6	15.6
6.9	6.9	11.3	11.3	15.7	15.7
7.0	7.0	11.4	11.4	15.8	15.8
7.1	7.0	11.5	11.5	15.9	15.9
7.2	7.2	11.6	11.6	16.0	16.0
7.3	7.3	11.7	11.7	16.1	16.2
7.4	7.4	11.8	11.8	16.2	16.3

2) Application of NTF$_{NL}$ to other wind turbines

(1) Requirements for the terrain class

The NTF can be applied to other wind turbines if they are the same type as the turbine tested; further, the requirements for the terrain class should be satisfied. Since local terrain may influence the NTF derivation and application, the terrain class has to be assessed. If the NTF is derived and applied on a wind farm, the local terrain classes are allowed to have a gap of ± 1. If it is applied to different sites, the local terrain classes have to be the same. If these conditions are not satisfied, the NTF has to be derived for flat terrain.

① Rix index

To compute the Rix index, a radius 20 times the hub height from the test wind turbine is divided into 10° direction sector, and the elevation points are determined every 30 m along a line that extends through the center of the direction sector. The absolute difference in altitude, Δz_i, is calculated using the following equation:

$$\Delta z_i = \left| (elevation_i - elevation_{i-1}) \right| \qquad (\text{IV-2})$$

where $elevation_i$ and $elevation_{i-1}$ are the elevations expressed in meters for adjacent elevation points. Table IV-9 presents the RIX terrain classification.

Table IV-9 RIX terrain classification

RIX [%]	RIX terrain class
Compliant to IEC 61400-12-1: 2005 Annex B (use L = 2.5 D)	0
RIX$_{0.04}$ < 16 and RIX$_{0.06}$ < 8 and RIX$_{0.08}$ < 4 but not class 0	1
RIX$_{0.04}$ < 32 and RIX$_{0.06}$ < 16 and RIX$_{0.08}$ < 8 but not class 1	2
RIX$_{0.04}$ < 48 and RIX$_{0.06}$ < 32 and RIX$_{0.08}$ < 16 but not class 2	3
RIX$_{0.04}$ ≥ 48 or RIX$_{0.06}$ ≥ 32 or RIX$_{0.08}$ ≥ 16	4

② Average slope

The average slope is derived as the slope of a radius that is five times the hub height from the test wind turbine for each 10° sector. Furthermore, the average slope for the measurement sector was calculated by averaging the slopes for all 10° sectors that are part of the measurement sector. Table IV-10 presents the slope terrain classification.

Table IV-10 Slope terrain classification

Absolute slope [%]	Slope terrain class
Compliant to IEC 61400-12-1: 2005 Annex B (use L = 2.5 D)	1
0° ≤ slope < 10°, but not class 1	2
10° ≤ slope < 15°	3
15° ≤ slope < 20°	4
20° ≤ slope	5

③ Final terrain class

The final terrain class is evaluated by adding terrain classes for the RIX index and the average slope for the measurement sector. The two test wind turbines for this work met the requirements. The final terrain classes for wind turbines no. 1 and 15 were both one, which gives a sum of 0 for the RIX index class and 1 for the slope class because no site calibration is required. Thus, the NTF derived from wind turbine no. 1 can be applied to wind turbine no. 15.

(2) Comparison of power curves

The nacelle anemometer wind speeds of wind turbines no. 1 and 15 were corrected to free-stream wind speeds by applying the derived NTFs. The corrected wind speeds were normalized at the reference air density to exclude the effect of wind variation on air density using Eq. III-11. The power curves were finally drawn using the bin method with an interval of 0.5 m/s, using Eqs. III-12 and III-13. Additionally, the power coefficients were calculated using Eq. III-14.

Figs. IV-25 and IV-26 show $PC_{NTF,NL}$, $PC_{NTF,Cup}$, PC_{Cup}, and PC_{NL} with the respective power coefficients for the test wind turbines. Each power curve met the range requirements of the wind data from a cut-in wind speed to over 1.5 times the wind speed at 80 % of the rated power of the wind turbine, and each bin had a minimum of three sampled data points.

In Fig. IV-25, the power curves and the power coefficients for wind turbine no. 1 were compared. $PC_{NTF,NL}$ and $C_{P,NTF,NL}$ were very similar to the references $PC_{NTF,Cup}$ and $C_{P,NTF,Cup}$, respectively. On the other hand, PC_{NL} and $C_{P,NL}$ were lower than the other values.

The power curves and the power coefficients for wind turbine no. 15 were compared in Fig. IV-26. $PC_{NTF,NL}$ was higher and $PC_{NTF,Cup}$ was lower than PC_{Cup}. $PC_{NTF,NL}$ was similar to that for wind turbine no. 1. A higher $C_{P,Cup}$ than the others was observed under low wind speeds, which was caused by very low wind speeds compared to the high power output in the early stage of the wind speeds. The ratio between the power curves and power coefficients for each wind turbine are listed in Tables IV-11 and IV-12.
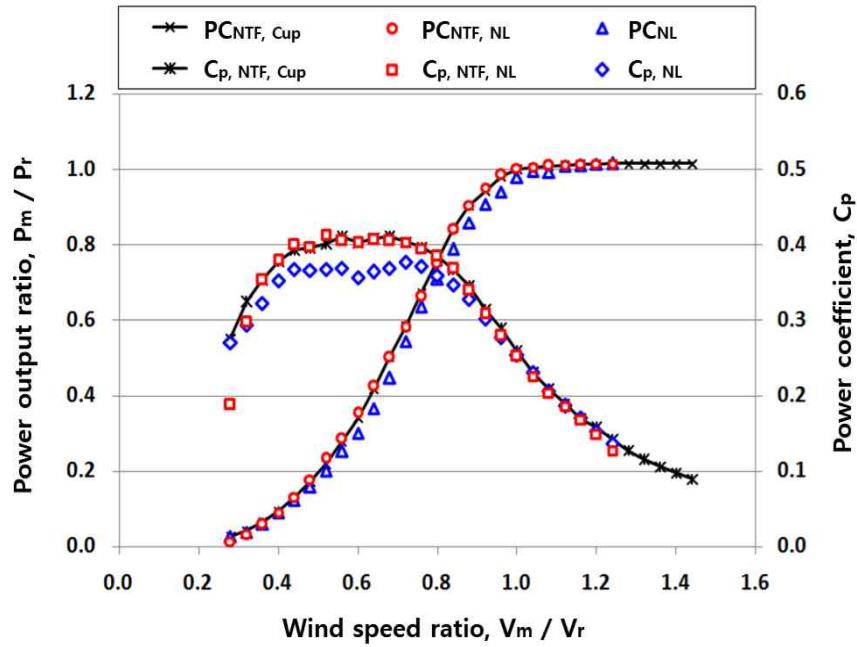
Fig. IV-25 Power curves and power coefficients for wind turbine no. 1 at the Dongbok wind farm
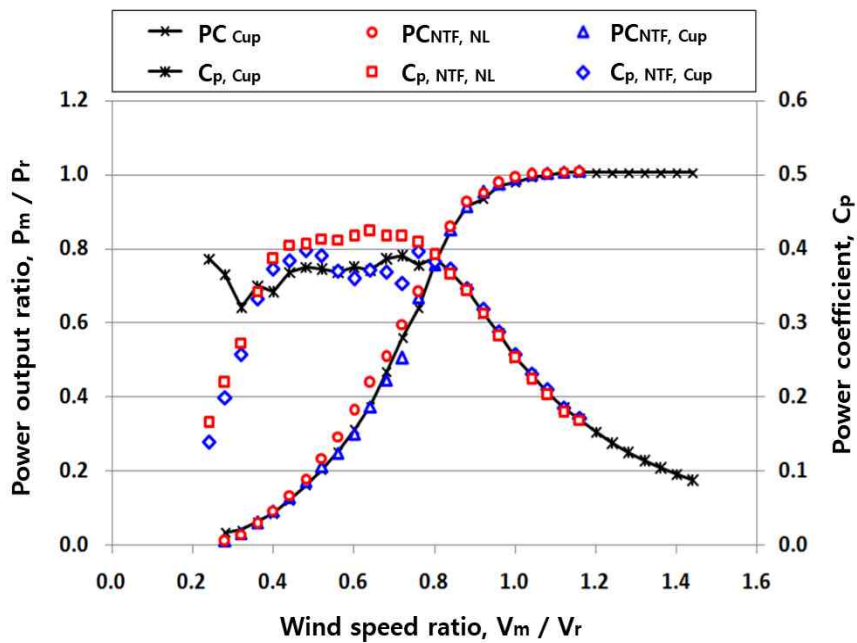
Fig. IV-26 Power curves and power coefficients for wind turbine no. 15 at the Dongbok wind farm

Table IV-11 Ratio between power curves and power coefficients for wind turbine no. 1 at the Dongbok wind farm

Bin no.	Wind speed [m/s]	Ratio between NTF_{NL} and NTF_{Cup}			Ratio between NTF_{NL} and NL		
		$V_{NTF,NL}$ /$V_{NTF,Cup}$	$P_{NTF,NL}$ /$P_{NTF,Cup}$	$C_{P,NTF,NL}$ /$C_{P,NTF,Cup}$	$V_{NTF,NL}$ /V_{NL}	$P_{NTF,NL}$ /P_{NL}	$C_{P,NTF,NL}$ /$C_{P,NL}$
7	3.5	0.91	0.51	0.90	0.91	0.52	0.70
8	4.0	0.94	0.76	0.58	0.94	0.85	1.01
9	4.5	0.97	0.91	0.84	0.97	1.00	1.09
10	5.0	0.98	0.96	0.94	0.98	1.01	1.08
11	5.5	1.00	1.00	0.96	0.99	1.07	1.09
12	6.0	1.01	1.04	1.01	1.01	1.13	1.09
13	6.5	1.01	1.07	0.99	1.01	1.17	1.12
14	7.0	1.01	1.03	1.00	1.01	1.13	1.10
15	7.5	1.01	1.04	1.01	1.01	1.18	1.13
16	8.0	1.01	1.02	0.99	1.01	1.16	1.12
17	8.5	1.00	1.00	0.99	1.01	1.12	1.10
18	9.0	1.00	0.99	1.00	1.00	1.07	1.07
19	9.5	1.00	0.99	1.01	0.99	1.04	1.06
20	10.0	1.00	0.99	1.03	1.00	1.06	1.07
21	10.5	1.00	1.00	1.05	1.00	1.07	1.06
22	11.0	1.01	1.00	1.06	1.01	1.05	1.03
23	11.5	1.01	1.01	1.08	1.01	1.05	1.02
24	12.0	1.01	1.00	1.06	1.01	1.05	1.01
25	12.5	1.01	1.00	1.08	1.01	1.03	0.99
26	13.0	1.01	1.00	1.09	1.01	1.01	0.98
27	13.5	1.01	1.00	1.08	1.01	1.02	0.99
28	14.0	1.01	1.00	1.08	1.00	1.00	1.00
29	14.5	1.00	1.00	1.10	1.01	1.00	0.98
30	15.0	1.02	1.00	1.06	1.01	1.00	0.98
31	15.5	1.04	1.00	1.05	1.02	1.00	0.93

Table IV-12 Ratio between power curves and power coefficients for wind turbine no. 15 at the Dongbok wind farm

Bin no.	Wind speed [m/s]	Ratio between NTF_{NL} and Cup			Ratio between NTF_{NL} and NTF_{Cup}		
		$V_{NTF,NL}/V_{Cup}$	$P_{NTF,NL}/P_{Cup}$	$C_{P,NTF,NL}/C_{P,Cup}$	$V_{NTF,NL}/V_{NTF,Cup}$	$P_{NTF,NL}/P_{NTF,Cup}$	$C_{P,NTF,NL}/C_{P,NTF,Cup}$
7	3.5	0.92	0.36	0.46	0.92	0.92	1.18
8	4.0	0.94	0.71	0.85	0.95	0.90	1.06
9	4.5	0.97	0.90	0.98	0.98	0.96	1.03
10	5.0	0.99	1.10	1.13	0.99	1.00	1.04
11	5.5	1.00	1.11	1.10	1.00	1.05	1.06
12	6.0	1.01	1.11	1.08	1.01	1.04	1.02
13	6.5	1.01	1.16	1.11	1.02	1.11	1.06
14	7.0	1.01	1.16	1.12	1.02	1.18	1.12
15	7.5	1.02	1.16	1.11	1.01	1.21	1.16
16	8.0	1.01	1.17	1.14	1.01	1.17	1.14
17	8.5	1.00	1.09	1.08	1.00	1.14	1.13
18	9.0	1.00	1.06	1.07	1.00	1.18	1.18
19	9.5	1.00	1.07	1.08	1.00	1.02	1.03
20	10.0	1.00	1.01	1.01	1.00	1.02	1.03
21	10.5	1.01	1.01	0.99	1.01	1.01	0.98
22	11.0	1.01	1.01	1.00	1.01	1.01	0.99
23	11.5	1.00	1.02	1.00	1.00	1.00	0.98
24	12.0	1.01	1.01	0.99	1.01	1.00	0.98
25	12.5	1.00	1.01	1.00	1.01	1.00	0.98
26	13.0	1.01	1.01	0.97	1.01	1.00	0.97
27	13.5	1.01	1.01	0.99	1.01	1.00	0.97
28	14.0	1.01	1.00	0.97	1.01	1.00	0.97
29	14.5	1.00	1.01	1.00	1.00	1.00	0.99
30	15.0	1.00	1.01	1.00	1.00	1.01	1.00
31	15.5	1.00	1.01	1.00	1.00	1.01	1.00

Table IV-13 lists the results of the two-parametric linear regression analysis between the power curves when $PC_{NTF,Cup}$ of wind turbine no. 1 and PC_{Cup} of wind turbine no. 15 were the references. The correlations of the $PCs_{NTF,NL}$ of the two wind turbines were very high, with slopes of 1.002 and 0.997, respectively, and coefficients of determination (R^2) of 0.999 and 0.997, respectively. Because $PCs_{NTF,NL}$ were very similar to the reference power curves, $PC_{NTF,Cup}$ and PC_{Cup}, which were derived from current IEC standards, the NTF from the nacelle LiDAR measurements could be applied to other wind turbines for power performance testing. The slopes and R^2 values of the other power curves had a high correlation.

Table IV-13 Two-parametric linear regression analysis between the power curves of the test wind turbines at the Dongbok wind farm

WTs	PCs	Slope	R^2
WT no. 1 (Reference: $PC_{NTF,Cup}$)	$PC_{NTF,NL}$	1.002	0.999
	PC_{NL}	0.992	0.997
WT no. 15 (Reference: PC_{Cup})	$PC_{NTF,NL}$	0.997	0.997
	$PC_{NTF,Cup}$	1.010	0.998

5. Uncertainty evaluation

1) Power curve uncertainty

(1) Components of uncertainty in power curve

The uncertainties of the power curves for wind turbine no. 15 were analyzed as a representative case. The uncertainties of $PC_{NTF,NL}$ and $PC_{NTF,Cup}$ were estimated by taking into account the following categories:

- Category A, uncertainty in electrical power ($S_{p,i}$);
- Category B, uncertainty in power output ($u_{p,i}$);
- Category B, uncertainty in wind speed ($u_{V,i}$);
- Category B, uncertainty in air density ($u_{AD,i}$);
- Category B, uncertainty in the utilized method ($u_{M,i}$).

Category A uncertainty in electrical power was calculated by statistical analysis based on the standard deviation of the power outputs in bin i divided by the square root of the number of sampled data in bin i. Category B uncertainties in the power output, air density, and utilized method were obtained by applying the uncertainty estimates provided in IEC 61400-12-2. Category B uncertainty in the utilized method is the uncertainty associated with air density correction, dynamic power measurement, seasonal variation, variation in the rotor inflow, and the effect of turbulence on averaging and binning. Category B uncertainty in wind speed is discussed in the next section. Table IV-14 lists the detailed information for estimates of uncertainty components.

Table IV-14 Estimates for uncertainty components from the power curve measurement

Source		Uncertainty component		Contribution factor without site calibration	
		Symbol	Estimate of magnitude	Symbol	Estimate of magnitude
Category A: Statistical	Variance in electrical power	$S_{P,i}$	$\sigma_{P,i}/\sqrt{N_i}$	N/A	N/A
Category B: Power output $c_{P,i}=1$	Current transformers	$u_{P1,i}$	0.35 %	I_{P1}	1
	Voltage transformers	$u_{P2,i}$	0.2 %	I_{P2}	1
	Power transducer	$u_{P3,i}$	0.5 %	I_{P3}	1
	Data acquisition system	$u_{dP,i}$	0.1 %	I_{dP}	1
Category B: Wind speed $c_{V,i}=\left\lvert\dfrac{P_i-P_{i-1}}{V_i-V_{i-1}}\right\rvert$	Anemometer calibration due to wind speed	$u_{V1,i}$	0.15 m/s	I_{V1}	1
	Anemometer calibration due to wind direction	$u_{V2,i}$	1.0 %	I_{V2}	1
	Operational characteristics	$u_{V3,i}$	Class 4 A k = 4	I_{V3}	0.7
	Mounting effects	$u_{V4,i}$	2.0 %	I_{V4}	0.7
	Flow distortion due to terrain	$u_{V5,i}$	1.0 %	I_{V5}	1
	NTF	$u_{V6,i}$	Table IV-15	I_{V6}	N/A
	Data acquisition system	$u_{dV,i}$	0.03 m/s	I_{dV}	1

Source	Uncertainty component		Contribution factor without site calibration	
	Symbol	Estimate of magnitude	Symbol	Estimate of magnitude
Category B: Air density $c_{T,i} = \left\| \dfrac{P_i}{288.15} \right\|$ $c_{B,i} = \left\| \dfrac{P_i}{1013} \right\|$				
Temperature sensor	$u_{T1,i}$	0.5 °C	I_{T1}	1
Radiation shielding	$u_{T2,i}$	2.0 °C	I_{T2}	1
Mounting effects	$u_{T3,i}$	0.33 °C	I_{T3}	1
Data acquisition	$u_{dT,i}$	0.04 °C	I_{dT}	1
Pressure sensor	$u_{B1,i}$	3.0 hPa	I_{B1}	1
Mounting effects	$u_{B2,i}$	1.89 hPa	I_{B2}	1
Data acquisition	$u_{dB,i}$	0.1 hPa	I_{dB}	1
Category B: Method $c_{M,i} = 1$				
Air density correction	$u_{M3,i}$	0.5 %	I_{M3}	1
Dynamic power measurement	$u_{M4,i}$	1 %	I_{M4}	1
Seasonal variation in power curve	$u_{M5,i}$	2 %	I_{M5}	1
Variation in rotor inflow	$u_{M6,i}$	2 %	I_{M6}	1
Effect of turbulence on averaging and binning	$u_{M7,i}$	1 %	I_{M7}	1

Table IV-15 Estimates for the uncertainty components from NTF measurement

Source		Uncertainty component		Contribution factor without site calibration	
		Symbol	Estimate of magnitude	Symbol	Estimate of magnitude
Category A: Statistical	Statistical uncertainty in captured dataset	$S_{NTF,i}$	$\sigma_{NTF,i}/\sqrt{N_i}$	N/A	N/A
Category B: Free stream wind speed	Anemometer calibration	$u_{FS1,i}$	0.1 m/s	I_{FS1}	1
	Operational characteristics	$u_{FS2,i}$	Class 1.9 A k = 1.9	I_{FS2}	1
	Mounting effects	$u_{FS3,i}$	1.0 %	I_{FS3}	1
	Flow distortion due to terrain	$u_{FS4,i}$	2.0 %	I_{FS4}	1
	Data acquisition system	$u_{FS5,i}$	0.03 m/s	I_{FS5}	1
Category B: Nacelle wind speed	Anemometer calibration uncertainty due to wind speed	$u_{N1,i}$	0.15 m/s	I_{N1}	1
	Anemometer calibration uncertainty due to wind direction	$u_{N2,i}$	1.0 %	I_{N2}	1
	Operational characteristics	$u_{N3,i}$	Class 4 A k = 4	I_{N3}	1
	Mounting effects	$u_{N4,i}$	2.0 %	I_{N4}	1
	Data acquisition system	$u_{dN,i}$	0.03 m/s	I_{dN}	1
Category B: Method	Seasonal variation	$u_{M2,i}$	2.0 %	I_{M2}	1

(2) Uncertainty in free-stream wind speed from nacelle LiDAR

Category B uncertainty in wind speed includes the uncertainty in the NTF, which contains the uncertainty in free-stream wind speed. Although the uncertainty component in free-stream wind speed from a met mast ($u_{FS,Cup}$) can be calculated in compliance with IEC 61400-12-2, the uncertainty in free-stream wind speed from the nacelle LiDAR ($u_{FS,NL}$) cannot be computed because of a lack of guidance in the current IEC standards. Thus, the following components were taken into account according to the following references:

- the statistical uncertainty of the nacelle LiDAR measurements ($u_{FS,NL1}$) [27];
- the uncertainty caused by flow distortion due to terrain ($u_{FS,NL2}$) [27];
- the uncertainty related to the measurement height ($u_{FS,NL3}$) [81];
- the uncertainty of the tilt inclinometers ($u_{FS,NL4}$) [81].

$u_{FS,NL1}$ was calculated from the standard deviation of the nacelle LiDAR measurements in bin i divided by the square root of the number of data points in bin i. $u_{FS,NL2}$ was estimated to be 2 % of the wind speed given in IEC 61400-12-2 because the distance between the test wind turbine and the measurement point was less than three times the rotor diameter, and no site calibration was undertaken.

① Uncertainty related to the measurement height ($u_{FS,NL3}$)

Because the nacelle LiDAR tilts owing to the motion of the wind turbine nacelle caused by wind variation, the tilt of the nacelle LiDAR should be set as −2.5 % of the hub height to measure wind conditions. In addition, the nacelle LiDAR measurements should be conducted within ± 2.5 % of the hub height. Fig. IV-27 illustrates the nacelle LiDAR measurement height relative to the hub height along with the wind speed ratio. The mean values of the

bin interval of 0.5 m/s are presented as well. The measurement height increased with an increase in the wind speed until the rated speed and then steadily decreased. This is because of blade pitching, which decreases the thrust force on the rotor after the rated wind speed. It was confirmed that the nacelle LiDAR measurement was conducted within ± 2.5 % of the hub height.
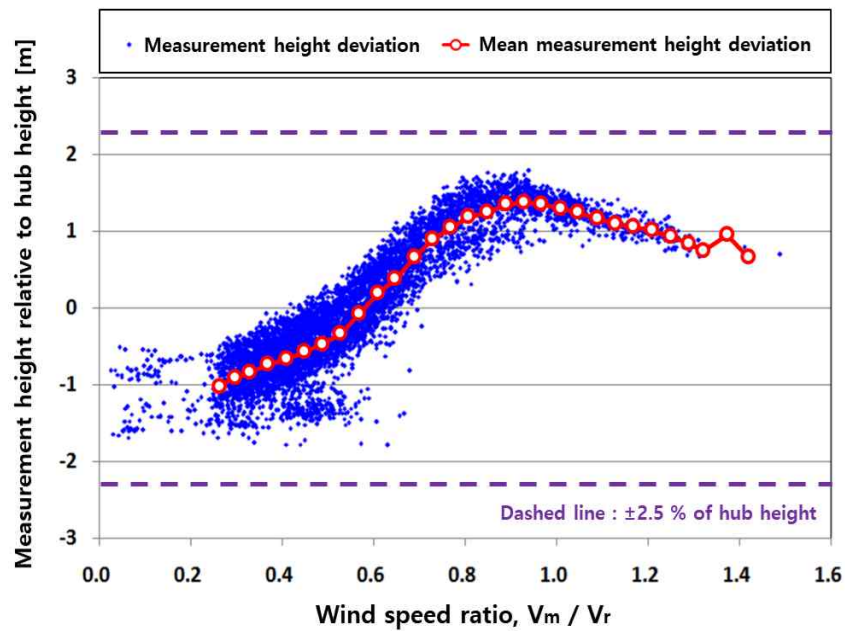
Fig. IV-27 Nacelle LiDAR measurement height relative to hub height

The uncertainty caused by variation in measurement height due to the tilting motion, u_{NLFS3}, can be calculated using Eqs. IV-3 and IV-4 [81]:

$$u_{NL,FS3} = \frac{1}{\sqrt{3}}\left(V_{NL,i} - V_{hub,i}\right) \tag{IV-3}$$

$$V_{hub,i} = V_{NL,i}\left(\frac{H}{z_{NL,i}}\right)^{0.5} \tag{IV-4}$$

제주대학교 중앙도서관
JEJU NATIONAL UNIVERSITY LIBRARY

where $V_{NL,i}$ is the average nacelle LiDAR wind speed in bin i, and $V_{hub,i}$ is the wind speed extrapolated to the hub height. $z_{NL,i}$ is the average nacelle LiDAR measurement height in bin i. In Eq. IV-4, the power law exponent was assumed to be 0.5.

Fig. IV-28 shows the relative uncertainty in the nacelle LiDAR wind speed due to the tilt motion, $u_{NL,FS3}$, with wind speed ratio. Uncertainties of approximately 0.12 % were distributed in the low wind speed regions and were very close to zero at 56 % of the rated wind speed. The uncertainty then rapidly increased until the rated wind speed, and it gradually decreased after the rated wind speed owing to blade pitching.
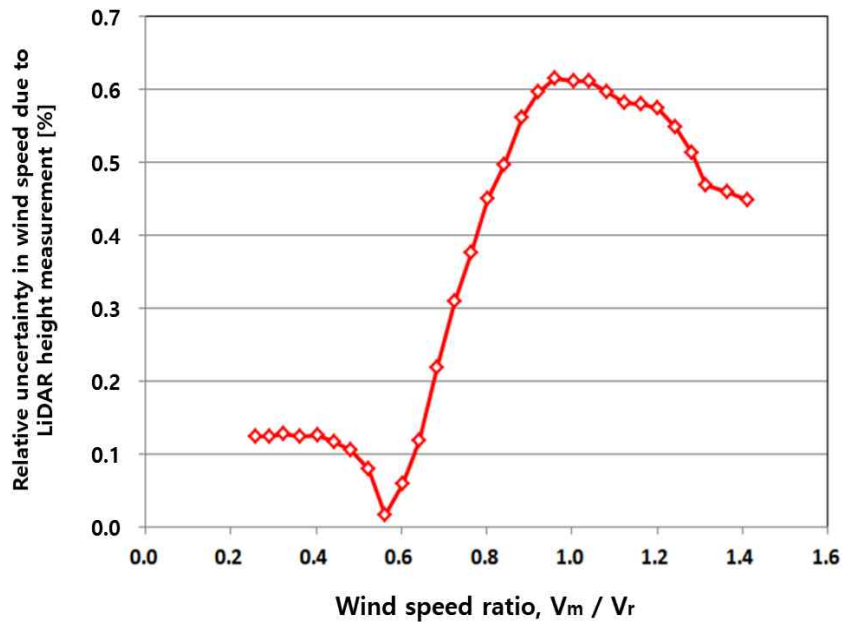
Fig. IV-28 Relative uncertainty in wind speed due to variation in the nacelle LiDAR measurement height

② Uncertainty of the tilt inclinometers ($u_{FS,NL4}$)

To evaluate $u_{FS,NL4}$, a calibration of the tilt inclinometer was conducted in accordance with the procedure in DTU Wind Energy E-0020 [74, 75]. The opening angle, α, was first calibrated by an iterative process of blocking and unblocking using a jig designed for beam detection at a distance of 29.85 m. The measured opening angle was confirmed to be 30.06°, and the maximum error of beam detection pointing, ΔH, was 21 mm. The tilt value was then measured using a theodolite Leica TM50. The uncertainty in the tilt, $u_β$, was estimated using the following equation [81]:

$$u_{\beta} = \sqrt{\left(2 \left(\frac{\Delta H}{2L\cos\dfrac{\alpha}{2}} \right)^2 + \Delta\beta_T^2 \right)} \qquad \text{(IV-5)}$$

where $\Delta\beta_T^2$ is the standard uncertainty of the theodolite associated with the tilt measurement, which was 0.03° according to the instrument calibration report. $u_β$ can be used to obtain the vertical length at a measurement distance of 2.5 times the rotor diameter, Δz_1, using Eq. IV-6 [81]:

$$\Delta z_1 = 2.5 \, D \, Tan \, (u_{\beta}) \qquad \text{(IV-6)}$$

Finally, $u_{FS,NL4}$ can be determined by the following equation assuming that wind shear follows a power-law profile with a shear exponent of 0.2 [81]:

$$u_{FS,NL4} = \left(\left(\frac{z_{hub} + \Delta z_1}{z_{hub}} \right)^{0.2} - 1 \right) V_{i,m} \qquad \text{(IV-7)}$$

③ Sensitivity factor for the wind speed

Additionally, the two sensitivity factors for category B uncertainty in wind speed for estimating power curve uncertainty, $c_{V,PC,i}$, and AEP uncertainty, $c_{V,AEP,i}$, were calculated using the following equations:

$$c_{V,PC,i} \approx \frac{1}{2}\left(\frac{(P_{i+1}-P_i)}{(V_{i+1}-V_i)}+\frac{(P_i-P_{i-1})}{(V_i-V_{i-1})}\right) \qquad \text{(IV-8)}$$

$$c_{V,AEP,i} \approx \frac{P_i-P_{i-1}}{V_i-V_{i-1}} \qquad \text{(IV-9)}$$

where P_{i+1}, P_i and P_{i-1} are bin-averaged power output in bins i+1, i and i-1, respectively. V_{i+1}, V_i, and V_{i-1} are bin-averaged wind speed in bins i+1, i, and i-1, respectively.

The sensitivity factors for category B uncertainties in the air density and method were also evaluated using other related equations presented in IEC 61400-12-2.

(3) Combined standard uncertainty

Finally, the combined standard uncertainties of the power curves, u_{PC}, were evaluated using the following equation:

$$u_{PC,i} = \sqrt{S_{P,i}^2+u_i^2} = \sqrt{S_{P,i}^2+u_{P,i}^2+c_{V,i}^2 u_{V,i}^2+c_{T,i}^2 u_{T,i}^2+c_{B,i}^2 u_{B,i}^2+u_{M,i}^2} \quad \text{(IV-10)}$$

where u_i is the combined category B uncertainty. $u_{T,i}$ and $u_{B,i}$ are the respective uncertainties in air temperature and pressure in bin i. $c_{T,i}$ and $c_{B,i}$ are the respective sensitivity factors of air temperature and pressure in bin i.

Fig. IV-29 and Table IV-16 present the combined standard uncertainties in $PC_{NTF,NL}$ ($u_{PC,NTF,NL}$) and $PC_{NTF,Cup}$ ($u_{PC,NTF,Cup}$) of wind turbine no. 15 and that in PC_{Cup} ($u_{PC,Cup}$), which was a reference complying with IEC 61400-12-1 1st edition. For all the uncertainties, higher uncertainties were generally found between wind speed ratios of 0.5 and 0.9, while lower uncertainties were estimated for the other wind speed ratios. The uncertainties of the power curves from NTFs were higher than that of PC_{Cup}. Because the uncertainty of $PC_{NTF,NL}$ was similar to that of $PC_{NTF,Cup}$ calculated in compliance with IEC 61400-12-2, the NTF derived from the nacelle LiDAR measurements could be utilized to estimate the power curves without a met mast.
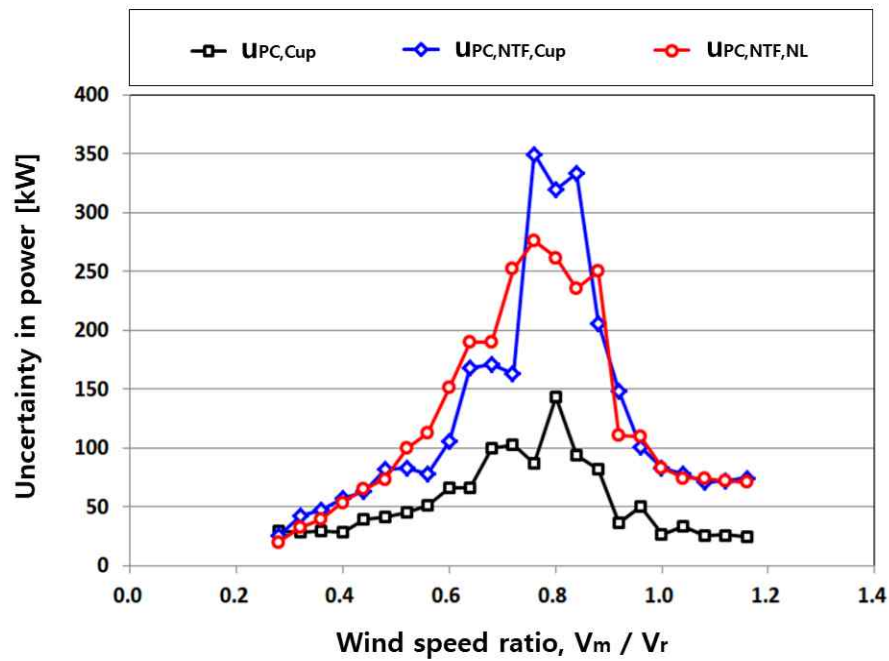
Fig. IV-29 Comparison of combined standard uncertainties for power curves of wind turbine no. 15 at the Dongbok wind farm

Table IV-16 Combined standard uncertainties for power curves of wind turbine no. 15 at the Dongbok wind farm

Bin no.	Wind speed [m/s]	$u_{PC,NTF,NL}$ [kW]	$u_{PC,NTF,Cup}$ [kW]	$u_{PC,NTF,NL}$ / $u_{PC,NTF,Cup}$	$u_{PC,Cup}$ [kW]	$u_{PC,NTF,NL}$ / $u_{PC,Cup}$
7	3.5	20.3	26.2	0.77	29.4	0.69
8	4.0	32.4	42.9	0.76	28.8	1.13
9	4.5	39.9	47.5	0.84	29.8	1.34
10	5.0	54.0	57.4	0.94	28.4	1.90
11	5.5	65.1	63.4	1.03	39.3	1.66
12	6.0	73.8	82.2	0.90	41.9	1.76
13	6.5	100.3	82.8	1.21	45.7	2.19
14	7.0	112.8	78.6	1.44	51.3	2.20
15	7.5	151.3	106.4	1.42	66.2	2.29
16	8.0	190.1	168.8	1.13	66.2	2.87
17	8.5	190.2	171.5	1.11	100.4	1.89
18	9.0	252.8	163.2	1.55	102.7	2.46
19	9.5	276.1	350.0	0.79	87.1	3.17
20	10.0	261.9	320.0	0.82	143.8	1.82
21	10.5	235.3	333.3	0.71	94.5	2.49
22	11.0	250.9	206.4	1.22	82.2	3.05
23	11.5	110.7	148.8	0.74	36.9	3.00
24	12.0	109.9	101.4	1.08	50.7	2.17
25	12.5	82.9	83.5	0.99	26.7	3.10
26	13.0	74.8	78.7	0.95	33.4	2.24
27	13.5	74.0	71.7	1.03	26.1	2.84
28	14.0	71.9	72.7	0.99	26.3	2.73
29	14.5	71.0	74.8	0.95	24.6	2.89

Fig. IV-30 presents the individual uncertainties of components in the category B uncertainties for $PC_{NTF,NL}$ of wind turbine no. 15. It was clear that the combined standard uncertainty of $PC_{NTF,NL}$ originated mainly from the wind speed. The high uncertainties of $PC_{NTF,NL}$ and $PC_{NTF,Cup}$ after the rated wind speed (Fig. IV-29) resulted from the uncertainty in the method, which was not taken into account when the uncertainty of PC_{Cup} was estimated. The power output, the temperature and the atmospheric pressure did not have a significant impact on u_{PC}.
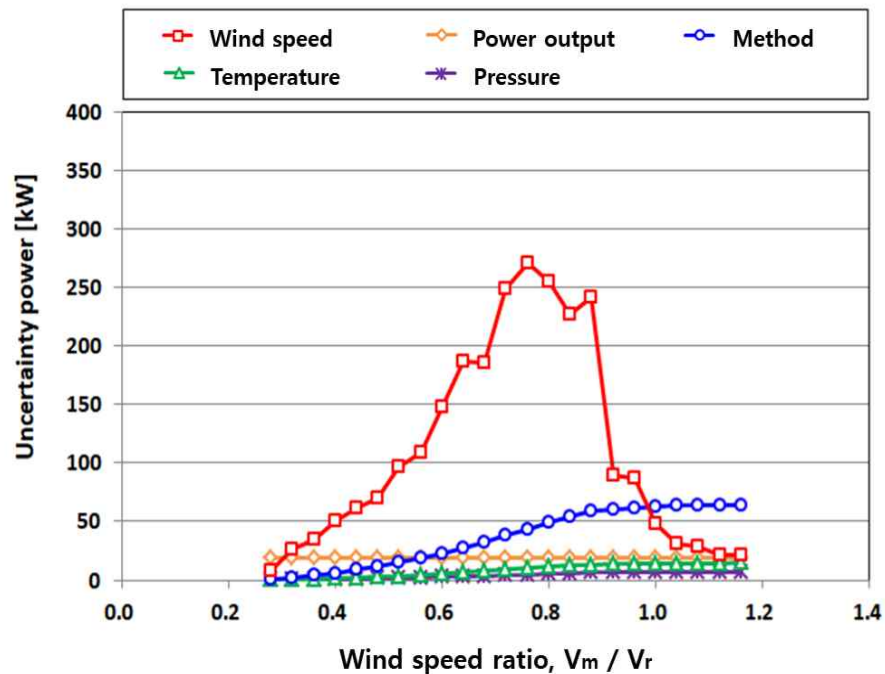
Fig. IV-30 Uncertainties of each component in category B uncertainty for $PC_{NTF,NL}$ of wind turbine no. 15 at the Dongbok wind farm

The individual uncertainties of each component of the wind speed in Fig. IV-30 are further presented in Fig. IV-31. The uncertainty of NTF derived from the nacelle LiDAR measurements was the highest among the uncertainty components. All other uncertainties related to the nacelle anemometer, such as operational characteristics and mounting effects, had comparatively low uncertainties of less than 100 kW. From Figs. IV-29 to IV-31, the combined standard uncertainty of $PC_{NTF,NL}$, was confirmed to result mostly from the NTF because the uncertainty for each bin of the NTF in Fig. IV-31 was slightly lower than the combined standard uncertainty for each bin in Fig. IV-29.
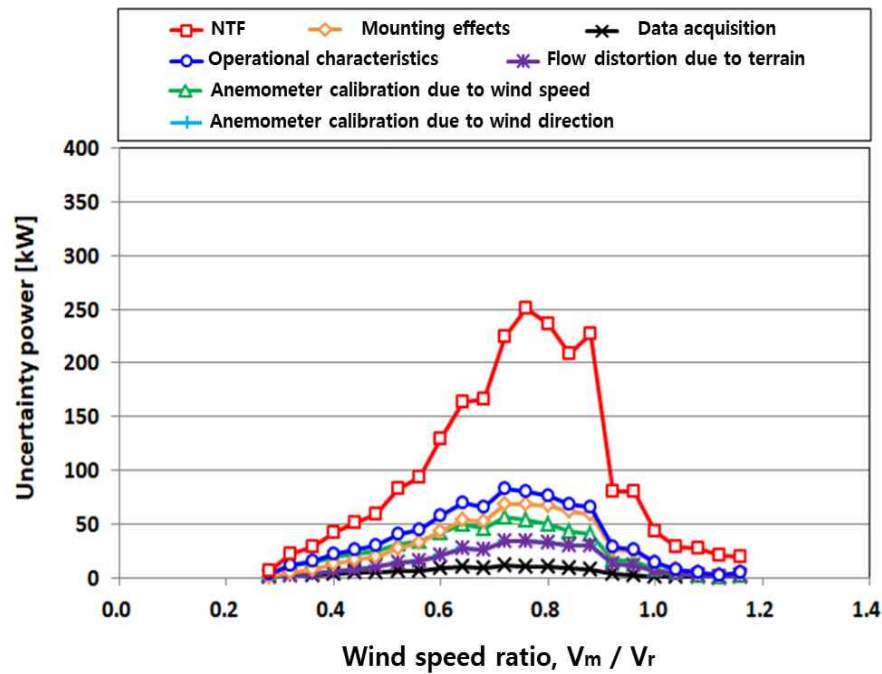
Fig. IV-31 Uncertainties of each component comprising the uncertainty in wind speed of wind turbine no. 15 at the Dongbok wind farm

2) AEP uncertainty

Using Eq. III-16, the AEPs were estimated from $PC_{NTF,NL}$ ($AEP_{NTF,NL}$), $PC_{NTF,Cup}$ ($AEP_{NTF,Cup}$), and PC_{Cup} (AEP_{Cup}) corresponding the Rayleigh wind speed distribution with annual mean wind speeds of 4 m/s to 11 m/s.

The uncertainties of the AEPs, u_{AEP}, were derived from the following equation:

$$u_{AEP} = N_h \sqrt{\sum_{i=1}^{N} f_i^2 \, S_i^2 + \left(\sum_{i=1}^{N} f_i \, u_i\right)^2} \qquad \text{(IV-11)}$$

where fi is the relative occurrence of wind speed between V_{i-1} and V_i in bin i. Fig. IV-32 shows the ratio and the uncertainties of $AEP_{NTFL,NL}$ ($u_{AEP,NTF,NL}$), $AEP_{NTF,Cup}$ ($u_{AEP,NTF,Cup}$), and AEP_{Cup} ($u_{AEP,Cup}$). A difference of 3.4 % to 7.0 % was found between $AEP_{NTF,NL}$ and AEP_{Cup} by means of IEC 61400-12-1. Additionally, $AEP_{NTF,NL}$ was from 3.5 % to 8.3 % higher than $AEP_{NTF,Cup}$ based on IEC 61400-12-2 for all annual mean wind speeds. $u_{AEP,NTF,NL}$ and $u_{AEP,NTF,Cup}$ were higher than $u_{AEP,Cup}$. On the other hand, $u_{AEP,NTF,NL}$ was almost the same as $u_{AEP,NTF,Cup}$ for all annual wind speeds.
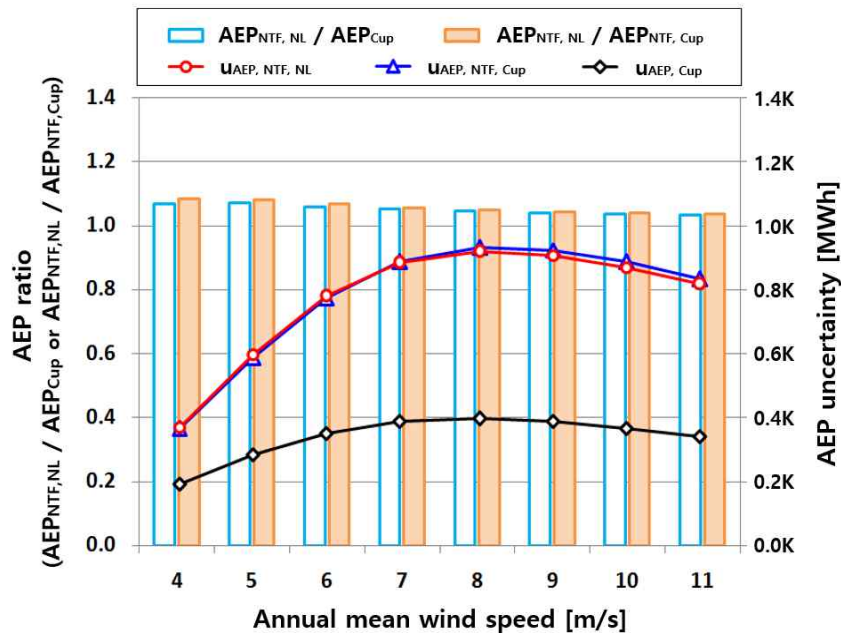
Fig. IV-32 Comparison of the AEP uncertainties of wind turbine no. 15 at the Dongbok wind farm

6. Discussion and conclusions

This study was conducted to identify the applicability of the NTF derived from nacelle LiDAR measurements to test the power performance of multiple wind turbines. $PC_{NTF,NL}$ was compared with PC_{Cup}, $PC_{NTF,Cup}$ and PC_{NL}. The uncertainties of the power curves and the AEPs were then discussed in detail. The results can be summarized as follows:

1) NTF_{NL} was estimated using the table method given in IEC 61400-12-2, and a strong relationship was identified between the nacelle LiDAR and the nacelle anemometer wind speeds, which had a slope close to one.

2) $PC_{NTF,NL}$ had a high correlation (based on the slope and R^2) with the reference power curves based on the IEC standards, which led to the conclusion that NTF_{NL} can be used for power performance testing of other wind turbines.

3) The combined standard uncertainty of $PC_{NTF,NL}$, was similar to that of $PC_{NTF,Cup}$ based on IEC 61400-12-2. Additionally, the combined standard uncertainty of the power curve derived from the NTF was derived from the uncertainty in the NTF.

4) Because $AEP_{NTF,NL}$ and $u_{AEP,NTF,NL}$ were very similar to $AEP_{NTF,Cup}$ and $u_{AEP,NTF,Cup}$ by means of the IEC 61400-12-2 in this study, there is potential for application of the NTF_{NL} to test the power performance of multiple wind turbines without a met mast.

V. Summary and conclusions

In this thesis, the applicability of the nacelle LiDAR was identified for wind turbine power performance measurement, and the use of the NTF by the nacelle LiDAR was proposed for power performance measurement of multiple wind turbines.

Through an analysis of the characteristics of nacelle LiDAR measurements, it was confirmed that the nacelle LiDAR measured comparatively accurate wind conditions under various weather and mechanical movement conditions. When the nacelle LiDAR wind data had an availability of 80 % or more, it was possible to derive reliable results from the data analysis.

Based on the results of an alaysis of the characteristics of nacelle LiDAR measurements, a standard for filtering nacelle LiDAR wind data was proposed. A strong relationship was identified between the selected nacelle LiDAR and reference wind speeds, with the slope and coefficient of determination having values close to one.

It was demonstrated that the nacelle LiDAR can be used for wind turbine power curve verification. The relative errors of PC_{NL} were approximately 3 % for PC_{Cup} and PC_{REWS} according to IEC 61400-12-1 1st and 2nd editions, and the ratio between the AEPs calculated from the power curves was close to one.

The NTF_{NL} proposed for power performance measurement for multiple wind turbines was verified. $PC_{NTF,NL}$ and $AEP_{NTF,NL}$ were in good agreement with $PC_{NTF,Cup}$ and $AEP_{NTF,NL}$ in accordance with IEC 61400-12-2. $u_{PC,NTF,NL}$ was almost the same as $u_{PC,NTF,Cup}$, and the difference between $u_{AEP,NTF,NL}$ and $u_{AEP,NTF,Cup}$ varied from 3.5 % to 8.3 %.

For power performance measurement of modern multi-megawatt wind turbines, the use of the nacelle LiDAR is cost efficient as it removes the need for installing tall and expensive met masts, especially offshore. The nacelle LiDAR is likely to replace a met mast to test the power performance of wind turbines.

Since the findings for the application of the nacelle LiDAR to wind turbine power performance measurement in this thesis were limited to this work, it is necessary to verify the applicability of the nacelle LiDAR through further experimental studies.

References

[1] Renewable capacity statistics 2018, International Renewable Energy Agency (IRENA), (2018).

[2] Global offshore wind market report 2018, Norwegian Energy Partners (NORWEP), (2018).

[3] Offshore wind in Europe : Key trends and statistics 2017, Wind Europe, (2018).

[4] E. Migoya, A. Crespo, J. Garcia and F. Moreno, Comparative study of the behavior of wind-turbines in a wind farm, Energy, 32 (10) (2007) 1871-85.

[5] A. Graves, K. Harman, M. Wilkinson and R. Walker, Understanding availability trend of operation wind farms, Proc. of the Windpower 2008 Conference, Houston, Texas (2008).

[6] K. H. Kim and S. G. Hyun. Power performance testing and uncertainty analysis for a 3MW wind turbine. J Korean Sol Energy Soc 2010;30(6).

[7] K. N. Ko and K. B. Kim, J. C. Huh. Variations of wind speed in time on Jeju Island, Korea. Energy 2010: 3381-7.

[8] L. Castro, A. Filgueira, M. A. Seijo, E. Munoz and L.Piegiari, Is it economically possible repowering wind farms, A general analysis in Spain, International Conference on Renewable Energies Power Quality (ICREPQ), 603 (2011).

[9] N. Conroy, J. P. Deane and Brian P. Ó Gallachóir, Wind turbine availability should it be time or energy based?-a case study in Ireland, Renewable Energy, 36 (11) (2011) 2967-71.

[10] K. Y. Oh, J. Y. Kim, J. K. Lee, M. S. Ryu and J. S. Lee, An assessment of wind energy potential at the demonstration offshore wind farm in Korea, Energy, 46 (2012) 555-63.

[11] H. C. Lim, Short-term observation of wind energy potentiality in the Wol-Ryong wind site, Journal of Mechanical Science and Technology, 26 (11) (2012) 3711-21.

[12] P. F. Bach, Capacity factor degradation for Danish wind turbines, Paul-Frederik Bach report, (2012).

[13] J. Harrison, Viability of the algonquin power Amherst Island wind energy generating system, Association to protect Amherst Island, (2012).

[14] G. Hughes, The performance of wind farms in the United Kingdom and Denmark, London: Renewable Energy Foun- dation, (2012).

[15] H. G. Kim, Analysis on wind turbine degradation of the Shinan wind power plant, Journal of the Korean Solar Energy Society, 33 (4) (2013) 46-50.

[16] R. Rodriguez, C. Rodriguez-Monroy, R. Rodriguez and F. Calvo, Analysis of renewable energy policies related to repowering the wind energy sector: the Spanish case, 11th Latin American and Caribbean Conference for Engineering and Technology 2013(LACCEI′2013), 104 (2013).

[17] Staffell and R. Green, How does wind farm performance decline with age?, Renewable Energy, 66 (2014) 775-86.

[18] J. Dai, D. Liu, L. Wen and X. Long. Research on power coefficient of wind turbines based on SCADA data. Renew Energy, (2016) 86: 206-15.

[19] S. H. Jeon, B. S. Kim and J. C. Huh. Comparison and verification of wake models in an onshore wind farm considering single wake condition of the 2 MW wind turbine. Energy, (2016) 93: 1769-77.

[20] E. T. Al-Shammari, S. Shamshirband, D. Petkovic, E. Zalnezhad, L. Yee, R. S. Taher. Comparative study of clustering methods for wake effect analysis in wind farm. Energy 2016; 95: 573-9.resource assessment. Energies, (2010) 3, 1087-141.

[22] C. B. Hasager, N. G. Nygaard, P. J. H. Volker, I. Karagali, S. J. Andersen, J. Badger. Wind farm wake: the 2016 horns rev photo case, (2017) 10, 317.

[23] S. L. Clainche, L. S. Lorente, J. M. Vega. Wind predictions upstream wind turbines from a LiDAR database, (2018) 11, 543.

[24] X. Shen, C. Zhou, G. Li, X. Fu, T. T. Lie. Overview of wind parameters sensing methods and framework of a novel MCSPV recombination sensing method for wind turbines. Energies, (2018) 11, 1747.

[25] A. Marjan, M. Shafiee. Evaluation of wind resources and the effect of market price components on wind farm income: a case study of Orland in Norway. Energies, (2018) 11, 2955.

[26] International Electrotechnical Commission (IEC), Wind turbine generator systems part 12-1: Power performance measurements of electricity producing wind turbines, First edition, IEC 61400-12-1, (2005).

[27] International Electrotechnical Commission. Wind turbine generator systems part 12-2: Power performance of electricity-producing wind turbines based on nacelle anemometry, First edition, IEC 61400-12-2, (2013).

[28] International Electrotechnical Commission. Wind turbine generator systems part 12-1: Power performance measurements of electricity producing wind turbines, Second edition, IEC 61400-12-1 (2017).

[29] A. J. Bowen and N. G. Mortensen. Wasp prediction errors due to site orography. Risø National. Lab. Tech. Rep. Risø-R.- (995(EN) (2004).

[30] D. A. Smith, M. Harris, A. S. Coffey, T. Mikkelsen, H. E. Jørgensen, J. Mann and R. Danielian. Wind lidar evaluation at the danish wind test site in Høvsøre. Wind Energy 9 (2006) 87-93.

[31] S. Emeis, M. Harris and R. M. Banta. Boundary-layer anemometry by optical remote sensing for wind energy applications. Meteorol. Zeitschrift 16(4) (2007) 337‐47.

[32] D. Kindler, A. Oldroyd, A. MacAskill and D. Finch. An eight month test campaign of the Qinetiq ZephIR system, Preliminary results. Meteorol. Zeitschrift 16 (2007) 479‐89.

[33] S. Bourgeois, Documentation and results of the SODAR and LiDAR measurements at the Maligrad site in Bosnia and Herzegovina, Meteotest (2008).

[34] F. Bingöl, J. Mann and D. Foussekis. Conically scanning LIDAR error in complex terrain. Meteorol. Zeitschrift. 18 (2) (2009) 189‐95.

[35] D. Foussekis, T. Georgakopoulos and I. Karga. Investigating Wind Flow Properties in Complex Terrain Using 3 LIDARS and a Meteorological Mast. Proceedings of the EWEA European Wind Energy Conference. Marseille, France (2009).

[36] A. Peña, C. Hasager, S. E. Gryning, M. Courtney, I. Antoniou and T. Mikkelsen. Offshore wind profiling using light detection and ranging measurements. Wind Energy 12 (2009) 105‐24.

[37] J. Gottschall and M. Courtney. Verification test for three WindCube WLS7 LiDAR at the Høvsøre test site. Risø DTU National Laboratory for Sustainable Energy, Risø‐ R.‐1732(EN) (2010).

[38] M. Harris, I. Locker, N. Power, N. Douglas, R. Girault, C. Abiven and O. Brady. Validated adjustment of remote sensing bias in complex terrain using CFD. European Wind Energy Conference. (2010).

[39] H. G. Kim and H. C. Ji, Uncertainty analysis on wind speed profile measurements of LiDAR by applying SODAR measurements as a virtual true value, J Korean Solar Energy Society, 30(4) (2010) 79‐85.

[40] H. G. Kim, C. W. Chyng, H. J. An and Y. M. Ji, Comparative validation of windcube LiDAR and remtech SODAR for wind resource assessment Remote sensing campaign at Pohang Accelerator Laboratory, J Korean Solar Energy Society, 31(2) (2011) 63‐71.

[41] B. Cañadillas, A. Westerhellweg and Neumann T, Testing the performance of a ground-based wind LiDAR system: One year intercomparison at the offshore platform FINO1, DEWI Magazine 38 (2011).

[42] S. Lang and E. McKeogh, LiDAR and SODAR measurements of wind speed and direction in upland terrain for wind energy purposes, Remote sensing, 3 (2011) 1871-901.

[43] M. C. Brower. Wind ResourceAssessment, A Practical Guide to Developing a Wind Project. Wiley & Sons, New Jersey (2012).

[44] P. Behrens, J. O'Sullivan, R. Archer and S. Bradley. Underestimation of monostatic sodar measurements in complex terrain. Bound.-Layer. Meteor. 143 (2012) 97 - 106.

[45] J. Sanz Rodrigo, F. Borbón Guillén, P. Gómez Arranz, M. S. Courtney, R. Wagner and E. Dupont. Multi-site testing and evaluation of remote sensing instruments for wind energy applications. Renew. Energy 53 (2013) 200-10.

[46] E. Jeannotte, C. Masson, D. Faghani, M. Boquet, B. Boucher and E. Osler. Estimation of LiDAR error over complex terrain covered with forest using numerical tools. Mech. Ind. 15 (2014) 169-74.

[47] R. M. Banta, Y. L. Pichugina, W. A. Brewer, J. K. Lundquist, N. D. Kelley, S. P. Sandberg, R. J. Alvarez, R. M. Hardesty and A. M. Weickmann. 3D volumetric analysis of wind turbine wake properties in the atmosphere using high-resolution Doppler lidar. J. Atmos. Ocean. Technol. 32 (5) (2015) 904-14.

[48] Z. R. Shu, Q. S. LI and P. W. Chan, Investigation of offshore wind energy potential in Hong Kong based on Weibull distribution function, Appl Energy, 156 (2015) 362-73.

[49] Z. R. Shu, Q. S. Li, Y. C. He and P. W. Chan, Observations of offshore wind characteristics by Doppler-LiDAR for wind energy applications, Appl Energy, 169 (2016) 150-63.

[50] S. Bradley, A. Strehz and S. Emeis. Remote sensing winds in complex terrain – a review. Meteorol. Zeitschrift. 24 (6) (2015) 547 - 55.

[51] S. Wharton, J. F. Newman, G. Qualley and W. O. Miller. Measuring turbine inflow with vertically-profiling LiDAR in complex terrain. J. Wind Eng. Ind. Aerodyn. 94(142) (2015) 217 - 31.

[52] D. Y. Kim, T. W. Kim, G. J. Oh, J. C. Huh and K. N. Ko, A comparison of ground-based LiDAR and met mast wind measurements for wind resource assessment over various terrain conditions, J Wind Eng Ind Aerodyn 158 (2016) 109-21.

[53] V. S. Indasi, M. Lynch, B. McGann, F. Yu, F. Jeanneret and J. Sutton. WAsP model performance verification using lidar data. Int. J. Energy Environ. Eng. 7 (2016) 105-13.

[54] S. Wan, L. Cheng and X. Sheng, Numerical analysis of the spatial distribution of equivalent wind speeds in large-scale wind turbines, J Mech Sci Technol, 31(2) (2017) 965-74.

[55] http://www.iec.ch/dyn/www/f?p=103:38:2235361504226::::FSP_ORG_ID.FSP _APEX_PAGE,FSP_PROJECT_ID:1282,23,100113

[56] A. Albers, H. Klug and D. Westermann, Power performance verification, In: 1999 European wind energy conference, Nice, France (1999) p. 657-60.

[57] B. Smith, H. Link, G. Randall and T. McCoy, Applicability of nacelle anemometer measurements for use in turbine power performance tests, National renewable energy laboratory, (2002).

[58] A. Curvers and P. A. Van der Werff, OWEZ wind farm efficiency, ECN, (2008).

[59] T. Üstüntas and A. Sahin, Wind turbine power curve estimation based on cluster center fuzzy logic modeling, Journal of Wind Engineering and Industrial Aerodynamics, 96(5) (2008) 611‒20.

[60] S. Barber, N. Chokani and R. S. Abhari, Assessment of wind turbine performance in Alpine environments. Wind engineering, 35(3) (2011) 313‒28.

[61] F. Trivellato, L. Battisti and G. Miori, The ideal power curve of small wind turbines from field data. Journal of Wind Engineering and Industrial Aerodynamics, 107‒108 (2012) 263‒73.

[62] S. Gill, B. Stephen and S. Galloway, Wind turbine condition assessment through power curve copula modeling, IEEE Trans Sustainable Energy, 3(1) (2012) 94‒101.

[63] N. Murugan, Umamaheswari, S. I. Vimal and P. Sivashanmugam, Experimental investigation on power output in aged wind turbines, Advances in Mechanical Engineering, (2012).

[64] B. D. Altan and M. Atilgan, A study on increasing the performance of Savonius wind rotors, Journal of Mechanical Science and Technology, 26(5) (2012) 1493‒9.

[65] A. Allik and J. Uiga, Deviations between wind speed data measured with nacelle‒mounted anemometers on small wind turbines and anemometers mounted on measuring masts, Agron Res 12(2) (2014) 433‒44.

[66] H. Suzuki, J. Suzuki, Y. Fujita and A. Muto, Evaluation of wind turbine power curve with nacelle anemometer, Jpn Wind Energy Assoc, (2013) 228‒31.

[67] W. Hernandez, J. L. Lopez‒Presa and J. L. Maldonado‒Correa, Power performance verification of a wind farm using the Friedman's test, Sensors, 16(6) (2016) 816.

[68] H. S. Oh and B. S. Kim, Comparison and verification of the deviation between guaranteed and measured wind turbine power performance in complex terrain, Energy, 85 (2015) 23-9.

[69] F. Ormel, I. L. Ducosson, M. D. Marre, R. E. Keck and C. K. Nielsen, Advanced nacelle anemometry and SCADA-data, analysis techniques and limitations, Lyon: Europe wind energy association (EWEA); (2012).

[70] H. W. Kim, K. N. Ko and J. C. Huh, Wind turbine power performance testing using nacelle transfer function, J Korean Solar Energy Society, 33(4) (2013) 51-8.

[71] D. H. Shin, H. W. Kim and K. N. Ko, Analysis of wind turbine degradation via the nacelle transfer function, J Mech Sci Technol, 29(9) (2015) 1-8.

[72] D. H. Shin, Master thesis: An Analysis of wind turbine degradation using the nacelle wind speed, (2015).

[73] D. H. Shin and K. N. Ko, Comparative analysis of degradation rates for inland and seaside wind turbines in compliance with the International Electrotechnical Commission standard, Energy, 118 (2017) 1180-6.

[74] M. Courtney, Calibrating nacelle LiDARs. DTU Wind Energy (2013).

[75] A. Borraccino, M. Courtney and R. Wagner, Generic methodology for calibrating profiling nacelle LiDARs, DTU Wind Energy report (2015).

[76] S. Davoust, A. Jehu, M. Bouillet, M. Bardon and B. Vercherin, Assessment and optimization of LiDAR measurement availability for wind turbine control, National renewable energy laboratory (NREL) (2014).

[77] R. Wagner, T. F. Pedersen, M. Courtney, J. Gottschall, I. Antoniou, R. Møller, S. M. Pedersen, T. Velociter, M. Bardon and A. S. Mouritzen, Power performance measured using a nacelle LiDAR, EWEA Annual Event (2011).

[78] R. Wagner, R. L. Rivera, I. Antoniou, S. Davoust, T. F. Pedersen, M. Courtney and B. Diznabi, Procedure for wind turbine power performance measurement with a two-beam nacelle LiDAR, DTU Wind Energy report (2013).

[79] R. Wagner and D. Samuel, Nacelle LiDAR for power curve measurement Avedøre campaign, DTU Wind Energy report (2013).

[80] R. Wagner, A. Sathe, A. Mioullet and M. Courtney, Turbulence measurement with a two-beam nacelle LiDAR, EWEA Annual Event (2013).

[81] R. Wagner, M. S. Courtney, T. F. Pedersen and S. Davoust, Uncertainty of power curve measurement with a two-beam nacelle-mounted LiDAR, Wind energy 19 (2016) 1269-87.

[82] P. A. Fleming, A. K. Scholbrock, A. Jehu, S. Davoust, E. Osler, A. D. Wright and A. Clifton, Field-test results using a nacelle-mounted LiDAR for improving wind turbine power capture by reducing yaw misalignment, In Journal of Physics: Conference Series, 524(1) (2014), p.012002 IOP Publishing.

[83] D. Schlipf, P. Fleming, F. Haizmann, A. Scholbrock, M. Hofsäß, A. Wright and P. W. Cheng, Field testing of feedforward collective pitch control on the CART2 using a nacelle-based LiDAR scanner, In Journal of Physics: Conference Series, 555(1) (2014), p.012090. IOP Publishing.

[84] A. Borraccino, Ph. D. thesis, Remotely measuring the wind using turbine-mounted LiDARs: Application to power performance testing, (2017).

[85] http://slapcoffee.com/2019/02/13/global-nacelle-mounted-lidar-system-for-wind market-demand-2019-leosphere-sgurrenergy-windar-photonics-zephir-lida/

[86] https://www.windpowermonthly.com/article/1440378/zephir-lidar-completes -dnv-gl-verification

[87] https://www.ews-consulting.com/en/news/items/research-project-wind-in-forests-how-much-wind-blows-over-our-forests.html

[88] http://www.partosystem.com/Files/1/Products/RemoteSensing/EN_PS_Ammonit _ZephIRLidar.pdf

[89] http://www.offshorewindindustry.com/news/wind-measurement-campaign-m3e a-wind-lidar

[90] https://2hoffshore.com/services/minimum-facilities-platforms/exploration-early -production/

[91] http://halo-photonics.com/Galion_LiDAR_system.htm

[92] D. H. Shin, K. N. Ko., M. S. Kang, D. H. Ryu, M. J. Kang and H. S. Kim, Comparison of wind turbine power curves using cup anemometer and pulsed Doppler light detection and ranging systems, Journal of mechanical science and technology (JMST), 33(4) (2019) 1663-71.

[93] D. H. Shin, K. N. Ko and M. S. Kang, Characteristics analysis and reliability verification of nacelle LiDAR measurements, Journal of the Korean energy society, 37(5) (2017) 1-11.

[94] Wind Iris user manual with software 1.5.1, Avent LiDAR technology.

[95] Windcube V2 LiDAR Remote Sensor User Manual version 06. Leoshphere, France.

[96] M. C. Brower, Wind resource assessment: A practical guide to developing a wind project, Wiley, (2012).

[97] D. H. Shin and K. N. Ko, Application of the nacelle transfer function by a nacelle-mounted light detection and ranging system to wind turbine power performance measurement, Energies, 12(6) (2019) 1087-106.

[98] D. H. Shin, K. N. Ko, M. S. Kang, D. H. Ryu, M. J. Kang and H. J. Kim, Accuracy assessment of four-beam nacelle LiDAR measurements in complex terrain, Journal of wind energy, 9(2) (2018) 20-7.

[99] Technical report, Windcube v2 + FCR validation on complex site and application for resource assessment analysis, Barlovento, 2012.

[100] Test report 546-01B, Operation of the windcube v2 LiDAR at CRES test station, Centre for renewable energy sources and saving (CRES), 2011.

[101] L. Wagner and C. Schmitt, Measuring wind profiles in complex terrain using doppler wind LiDAR systems with FCR and CFD implementations, 2013.

[102] Windcube FCR measurements; Princples, performance and recommendations for use of the flow complexity recognition (FCR) algorithm for the windcube ground-based LiDAR, Leoshphere, France.

[103] Technical note, GL GH position statement on the windcube remote sensing device, GL Garrad Hassan, 2012.

[104] Windcube v2 LiDAR Remote Sensor User guide FCR option. Leoshphere, France.

Appendices

1. Appendix A. International papers

2. Appendix B. Domestic papers

3. Appendix C. Conference papers

4. Appendix D. R&D projects (only government task)

5. Appendix E. International standardization action

6. Appendix F. Photographs

Appendix A. International papers

1) D. H. Shin and K. N. Ko, Application of the nacelle transfer function by a nacelle-mounted light detection and ranging system to wind turbine power performance measurement, Energies, 12(6) (2019) 1087-106.

2) D. H. Shin, K. N. Ko, M. S. Kang, D. H. Ryu, M. J. Kang and H. S. Kim, Comparison of wind turbine power curves using cup anemometer and pulsed Doppler light detection and ranging systems, Journal of mechanical science and technology (JMST), 33(4) (2019) 1663-71.

3) D. H. Shin and K. N. Ko, Comparative analysis of degradation rates for inland and seaside wind turbines in compliance with the International Electrotechnical Commission standard, Energy, 118 (2017) 1180-6.

4) D. H. Shin, H. W. Kim and K. N. Ko, Analysis of wind turbine degradation via the nacelle transfer function, Journal of mechanical science and technology (JMST), 29(9) (2016) 4003-10.

Appendix B. Domestic papers

1) D. H. Ryu, M. S. Lee, C. W. Lim, K. N. Ko, D. H. Shin, B. S. Kang and D. W. Kim, Nacelle-mounted LiDAR beam line of sight (LOS) wind speed calibration procedure using meteorological mast, Journal of wind energy, 9(4) (2018) 24-31.

2) D. H. Shin, K. N. Ko, M. S. Kang, D. H. Ryu, M. J. Kang and H. J. Kim, Accuracy assessment of four-beam nacelle LiDAR measurements in complex terrain, Journal of wind energy, 9(2) (2018) 20-7.

3) D. H. Shin, K. N. Ko and M. S. Kang, Characteristics analysis and reliability verification of nacelle LiDAR measurements, Journal of the Korean energy society, 37(5) (2017) 1-11.

4) B. C. Ju, D. H. Shin and K. N. Ko, Accuracy assessment of annual energy production estimated for Seongsan wind farm, Journal of the Korean solar energy society, 36(2) (2016) 9-17.

Appendix C. Conference papers

1) D. H. Shin, K. N. Ko, I. H. Kim, D. H. Ryu, M. J. Kang and H. J. Kim, Characteristics analysis and reliability validation of 4 beam nacelle LiDAR measurements, Korea wind energy association, 2017.
   ** Excellent paper award

2) D. H. Shin and K. N. Ko, Characteristics of wind turbine power performance with wake effect and turbulence intensity within a wind farm, Korea wind energy association, 2016.

Appendix D. R&D projects (only government task)

1) Technology development for power performance measurement of wind turbines and wind farms using the nacelle LiDAR, May 2016 – December 2018

   ** Role : Project manager of managing department

2) Development of yaw optimizer for wind turbine efficiency improvement using LiDAR and machine learning, November 2015 – October 2016

3) Development of optimization design onshore and offshore wind farms in Jeju Island, June 2013 – April 2015

4) Development of wind energy efficient management system and establishment of a standardization system, May 2012 – April 2015

Appendix E. International standardization action

\<Joined IEA Wind Task 32 as the representative of South Korea\>

\<IEA Wind Task 32 workshop in Munich, Germany on September 2016\>

\<IEA Wind Task 32 general meeting in Calgary, Canada on October 2018\>

Appendix F. Photographs

<View seen at the nacelle of Dongbok wind turbine no. 1 (photograph by D. H. Shin)>
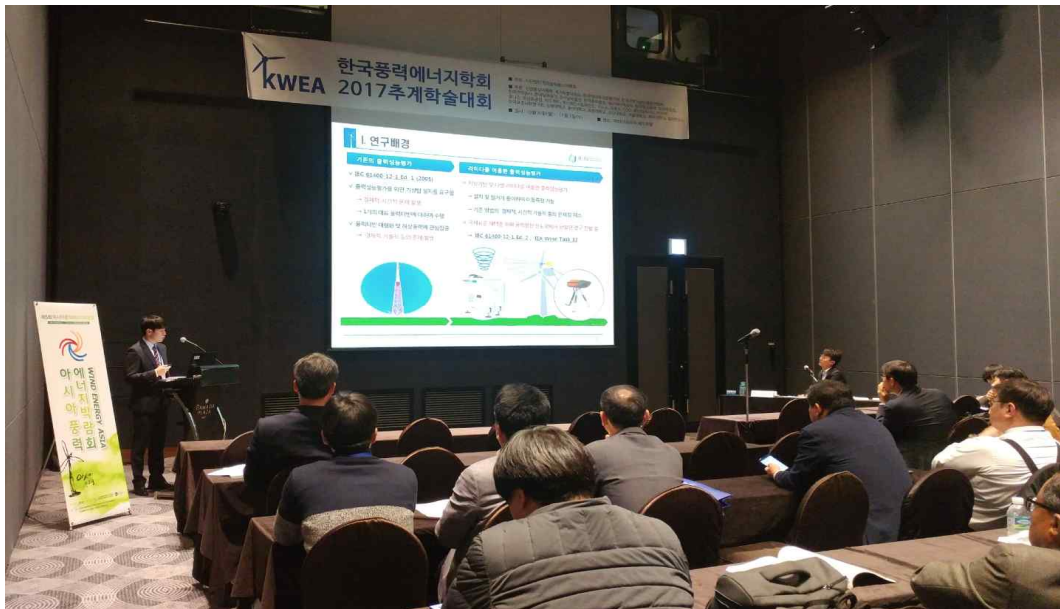

<4-beam nacelle LiDAR installed on Dongbok wind turbine no. 1 (photograph by D. H. Shin)>

<Ground LiDAR installed in Haengwon wind farm (photograph by D. H. Shin)>

<Ground LiDAR installed in Dongbok wind farm (photograph by D. H. Shin)>

<Presentation in Korea wind energy association conference on October 2017>

<Members of the wind farm design laboratory>

Acknowledgement

I would like to sincerely thank everyone who contributed
to my Ph. D. degree.

I would like to express my sincere gratitude to my supervisor
Prof. Kyungnam Ko.

I would also like to thank my colleagues
in the wind farm design laboratory

and the institutions that worked together for about three years:
Korea Testing Laboratory, Jeju Energy Corporation,
Korea Register, Vision Plus, and Doarm Engineering.

Lastly, I would like to extend my thanks to my beloved family.

감사의 글

졸업하는 날이 올까 싶었던 박사과정 입학이 엊그제 같은데 어느새 4년이란 시간이 흘러 졸업을 하게 되었습니다. 졸업을 앞두고 지난 박사과정 동안 정말 열심히 했는지 돌아보게 되고, 과연 박사로써 앞으로 나아갈 준비가 되었는지 걱정도 됩니다.

박사과정 중 약 3년 정도의 시간을 나셀 라이다 연구과제의 프로젝트 매니저로 지내며, 연구 과제를 수행함에 있어 대부분의 것이 새롭고 쉽지 않은 도전이었지만 하나하나 해결해나가며 저를 더 성숙하고 발전할 수 있게 한 값진 경험이었던 것 같습니다.

박사과정 입학부터 졸업까지 모든 것이 저 혼자 할 수 없는 일이었고, 많은 분들의 도움이 있었기에 가능했다고 생각이 듭니다. 이 면을 빌려 감사의 마음을 전합니다.

아무것도 아니었던 저를 박사로 만들어주신 지도교수 고경남 교수님, 더 열심히 하지 못하여 죄송하고 끝까지 저를 믿어주셔서 감사합니다. 저희 대학원 풍력공학부를 이끌어주시는 허종철 교수님, 김범석 교수님 항상 감사합니다. 앞으로 더 열심히 하는 모습으로 보답하도록 하겠습니다.

그리고 저의 박사학위논문 심사를 위해 바쁜 시간 내주신 정지현 교수님, 강용덕 교수님께 감사의 말씀을 전합니다. 심사 결정에 누가 되지 않는 앞으로도 열심히 하는 박사가 되도록 하겠습니다.

많이 알려주고 싶었지만 부족해서 많이 알려주지 못해 미안한 자랑스러운 우리 풍력단지설계 연구실 후배들에게 감사의 마음을 전합니다. 저희 학생들의 연구를 위해 아낌없는 지원과 조언을 해주신 양경부 박사님, 그리고 신재생에너지 엔지니어링 연구실, 유체역학 연구실 선후배님들께 감사의 말씀을 전합니다.

나셀 라이다 프로젝트를 수행하며 함께 고생한 한국산업기술시험원, 제주에너지공사, 한국선급, 비전플러스, 도암엔지니어링 참여기관 분들께 감사의 말씀을 전합니다.

이 외에도 도움을 주시고 응원해주신 많은 분들께 한 분 한 분 고마움을 다 전하지 못하여 죄송하고 감사합니다.

마지막으로 아들의 어떠한 선택도 믿고 지원해주신 우리 가족 아버지, 어머니, 동생 희진이에게 감사의 마음을 바칩니다.